UCLA
UCLA Electronic Theses and Dissertations

Title
Effect of Chemical Kinetic Mechanisms on Turbulent Combustion

Permalink
https://escholarship.org/uc/item/1gc653j8

Author
Badillo-Rios, Salvador

Publication Date
2020

Peer reviewed|Thesis/dissertation

UNIVERSITY OF CALIFORNIA

Los Angeles

Effect of Chemical Kinetic Mechanisms

on Turbulent Combustion

A dissertation submitted in partial satisfaction

of the requirements for the degree

Doctor of Philosophy in Aerospace Engineering

by

Salvador Badillo-Rios

2020

ABSTRACT OF THE DISSERTATION

Effect of Chemical Kinetic Mechanisms

on Turbulent Combustion

by

Salvador Badillo-Rios

Doctor of Philosophy in Aerospace Engineering

University of California, Los Angeles, 2020

Professor Ann Renee Karagozian, Chair

Understanding the effects of alternative chemical kinetic mechanisms in turbulent reactive flows is critical to the ability to accurately simulate combustion processes, especially in practical systems. Exploring such effects is not a trivial endeavor because turbulent reactive simulations can be costly, especially when Direct Numerical Simulations (DNS) are employed and/or for large parameter studies. In addition, detailed chemical kinetic mechanisms are often too large and impractical for incorporation in multi-dimensional transient flow field simulations. The large number of species and reactions, as well as the wide range of time scales, in the detailed chemical kinetics account for the computational cost in large-scale combustion simulations. Currently, reduced mechanisms are developed under specific laminar flow conditions in which selected global properties of a flame (e.g., ignition delay time, laminar flame speed, adiabatic flame temperature) are matched to those of the original detailed mechanism. However, this imposes restrictions on the operating range and applicability of these reduced mechanisms. For example, in addition to the presence of turbulence, it cannot be guaranteed that these specific conditions will be met everywhere in the flowfield for non-premixed combustion. If turbulence is shown to affect the results from reduced models, then use of the model would become flow and regime specific. It may even be necessary to simulate each flow configuration with detailed chemical kinetic mechanisms before reduced models can be developed for that flow configuration. A better understanding of the sensitivities of turbulent reactive flow results is clearly needed to address these issues.

The Chemical Explosive Mode Analysis (CEMA) appears to be an efficient computational diagnostic tool that may give insight into the the important species and reactions in a given flowfield, and to help to explain differences that various kinetic mechanisms may produce in a reactive flowfield. Thus, CEMA may have the potential to help in the development of reduced mechanisms.

The objective of this dissertation is to gain insights into the influence of alternative chemical kinetics mechanisms on the results of turbulent combustion simulations and, specifically, the effects of these mechanisms under conditions representative of rocket injector applications. Methane-oxygen combustion simulations of a shear coaxial injection configuration are performed using several chemical kinetic mechanisms ranging from detailed, to skeletal, to reduced mechanisms. Multi-dimensional simulations of rocket injector flowfields are used to establish the underlying issues and motivate the studies. 0D and 1D simulations in concert with the the Chemical Explosive Mode Analysis (CEMA) procedure are then employed to develop insight into the important species and reactions involved to explain differences between the different kinetic mechanisms. Injector results reveal that it is important to establish grid convergence before making comparisons of reaction mechanisms. They also show that the skeletal FFCM1-21 chemical mechanism has time-step and spatial grid sensitivity compared to the detailed GRI-Mech 3.0 mechanism. Given that FFCM1-21 is a skeletal mechanism, the absence of certain species may be responsible for the sensitivity.

The CEMA module is first validated with published hydrogen-air 1D premixed flame results. The CEMA method is then applied to a 0D homogeneous combustion problem to obtain insights about the important species and reactions in methane-oxygen combustion for various chemistry models relevant to the rocket injector problem described earlier. A gaseous methane-oxygen mixture is studied as well as mixtures with the addition of H and/or O radicals to simulate the effects of turbulent mixing of burnt gases with reactants. For these cases, a new detailed mechanism (FFCM-1) and a reduced version (FFCMY-12) are used to study the underlying sensitivities. It is found that there is poor prediction of the ignition delay by the reduced mechanism FFCMY-12 in the presence of radicals as compared with the full FFCM-1 mechanism. Trends seen in 0D results help to identify the important

species and reactions necessary for a reduced mechanism to replicate important phenomena such as ignition. Because of this, there is confidence that 0D simulations with the CEMA implementation could also help in pinpointing the pertinent species and reactions and in identifying and determining what to examine in a large and more complex turbulent dataset.

The dissertation of Salvador Badillo-Rios is approved.

Xiaolin Zhong

Raymond Mitchell Spearrin

Jeffrey D. Eldredge

Venkateswaran Sankaran

Ann Renee Karagozian, Committee Chair

University of California, Los Angeles

2020

TABLE OF CONTENTS

LIST OF FIGURES

NOMENCLATURE

E_i	Inviscid flux vector
P	Pressure
H	Source term vector
m	Mass
V	Volume
Q	Solution vector
R	Universal gas constant
T	Temperature
$F_{v,i}$	Viscous flux vector
Y_ℓ	Species mass fraction
Y_ℓ	Species mole fraction
Δt	Time-step size
Δx	Mesh size
γ	Ratio of specific heat coefficients, c_p/c_v
ρ	Density
c_p	Specific heat coefficient at constant pressure
c_v	Specific heat coefficient at constant volume
u_i	Velocity component
h^0	Stagnation enthalpy
G^0	Gibbs free energy
$V_{i,\ell}$	Diffusion velocity
$\tau_{i,j}$	Viscous tensor
q_i	Heat flux in direction i
δ_{ij}	Kronecker symbol
$\dot{\omega}_\ell$	Source term for species ℓ
W_ℓ	Molecular weight of species ℓ
μ	Dynamic viscosity

ν_t Turbulent viscosity

k Turbulent kinetic energy

ω Turbulent dissipation

L_T Turbulent length scale

E_a Activation energy

K_{eq} Equilibrium constant

K_f Forward rate of reaction k

K_b Reverse rate of reaction k

ν Stoichiometric coefficient

λ_{exp} Largest eigenvalue of chemical Jacobian

$\mathbf{b_e}$ Left eigenvector for CEM

$\mathbf{b_e}$ Right eigenvector for CEM

$\mathbf{S}$ Matrix of stoichiometric coefficients

$\mathbf{w}$ Net reaction rate vector

D_ω Chemical Jacobian used

LES Large-Eddy Simulations

DNS Direct Numerical Simulations

$RANS$ Reynolds-Averaged Navier-Stokes

DES Detached Eddy Simulations

$CEMA$ Chemical Explosive Mode Analysis

CSP Computational Singular Perturbation

EI Explosion Index

PI Participation Index

Re Reynolds Number

Pr Prandtl Number

Sc Schmidt Number

ACKNOWLEDGMENTS

Reflecting on my doctoral journey at UCLA, I realize I would be remiss if I did not acknowledge some of the great people in my life who have supported, mentored, and encouraged me, not only academically, but also in my personal life throughout the years. I would not have gotten this far in my journey without them. Here, I want to provide a small token of my deepest gratitude to some of these individuals.

I would first like to thank my family who has always supported me in pursuing my dreams. As the oldest of my siblings and a first generation college student, I, as well as my family, found going to graduate school to be a foreign concept. Despite the fact they did not fully understand my career choice or what I studied, I am very appreciative of their open-mindedness and support. To my mom, you bravely sacrificed everything to come to this country and worked hard to give my siblings and I a life and opportunities you never had. You are my inspiration. From'you, I learned what it is to be determined, hard working, and kind. I hope I have made you proud. To my younger brother Eddie, thank you for being good to me and being there when I've needed you. To my youngest brother Danny, your unconditional love has been a safe haven for me. You have been a blessing in my life and you have taught me to be more more kind and patient. I dedicate this accomplishment to you and celebrate this milestone as if it was one of your own. To my dad, thank you for wishing me success in school. To my close friends who are like family (Eleazar, Alex, Brenda, and others not explicitly listed), you have seen the journey in my career from the very beginning and have always been there when I needed you the most. Thank you for looking out for me, giving me advice, and allowing me to be my authentic self around you.

I have also been fortunate to have several mentors throughout the course of my academic career. Many thanks to my teachers in elementary school, Mrs. McGuigan and Mrs. Nishida, who encouraged me as a young boy to dream big. To Mrs. Bettencourt and Brother Javier Gonzalez, you guys gave me the gift of playing musical instruments, which to this day has helped me unwind during the most stressful times. Thank you to KiKa Friend (California Alliance for Minority Participation) for championing for diversity in the STEM fields and

higher education, for first introducing me to students that look like me at all levels in their academic career, and for giving me opportunities and showing me the realm of possibilities at my disposal. Also to Leo, I am grateful for the cheerful smile you always put on (even when you were not always feeling it) and thank you for always lending an ear to hear me vent. I am very appreciative of Mrs. Kim Pawell for her support throughout the years. To Professor Guillaume Blanquart (Caltech) and Dr. Robert Barlow (Sandia National Labs, Combustion Research Facility), a huge thank you for taking a chance on me, welcoming me into your labs with open arms, and offering me advice in my career exploration.

I am especially grateful for my advisors, Professor Karagozian and Venke Sankaran. To Professor Karagozian, I thank you for always believing in me, being patient with me, and pushing me to be better. To Venke, thank you for your continuous support and invaluable guidance in my dissertation progress, personal growth, and career development. I also could not have done this without Matthew Harvazinski, who worked closely with me, encouraged me, and provided thoughtful discussions and guidance. What I have learned from the three of you will benefit me for the rest of my life.

I would also like to extend my gratitude to the Edwards Air Force Research Lab (AFRL) team, who have all enriched my life in some way. Special thanks to Zoltan Jozefik and Ayaboe Edoh for their fruitful discussions, guidance, and entertaining conversation. Also a special thank you to UCLA staff (Abel, Evgenia, Collin, Amanda) who are the workhorses behind the scenes.

VITA

2017   M.S. (Aerospace Engineering), UCLA, Los Angeles.

2015   B.S. (Aerospace Engineering) and B.S. (Mechanical Engineering), UC
                Irvine, Irvine.

2015   Cota-Robles Fellowship (UCLA)

2016-2019   National Defense Science and Engineering Graduate (NDSEG) Fellowship

PUBLICATIONS AND PRESENTATIONS

S Badillo-Rios, ME Harvazinski, V Sankaran, and AR Karagozian, *Timescale Analysis Procedure Applied to Premixed and Non-Premixed Turbulent Combustion*, APS (2019): P05-005.

S Badillo-Rios and AR Karagozian, *Effect of Alternative Kinetic Mechanisms on Turbulent Combustion in a Shear Coaxial Injector*, Bulletin of the American Physical Society 63 (2018).

S Badillo-Rios and AR Karagozian, *Modeling and Simulation of Swirl Stabilized Turbulent Non-Premixed Flames*, APS (2017): KP1-110.

CHAPTER 1

Introduction

1.1 Importance of Turbulent Combustion

Turbulent combustion is the main process in aero-propulsion systems, which involves the conversion of chemical energy to thermal energy. Among the multiple processes in turbulent combustion, fluid dynamics and chemical reactions play the largest roles [3]. Thus, combustion is a challenging subject to study due to the complex chemical kinetics and transport processes that are involved. For example, the pyrolysis and oxidization processes in realistic fuels can involve hundreds of species and thousands of chemical reactions, which can present challenges in both diagnosing the flame and in performing numerical computations [4]. Furthermore, the mixing between fuel and oxidizer can take place in premixed, non-premixed, or partially-premixed configurations. The type of configuration chosen can impact the roles of chemistry and transport, often requiring the design of different combustors for each type. In addition, complex local flame features and dynamics can arise due to the presence of varying turbulence often found in realistic combustors. Many experimental studies of premixed [5–11] and non-premixed [12–15] turbulent flames have been performed, yielding significant progress in the field. Typically, these studies involve measuring instantaneous and time-averaged scalar or vector fields of velocity, temperature, and some chemical species concentrations in order to obtain insight about the flow and flame processes involved.

There has also been a significant increase in the computational power and the ability to implement massively parallel architectures over the past decades, which has allowed computational fluid dynamics (CFD) to aid in understanding turbulence and combustion. Several approaches, such as Direct Numerical Simulations (DNS), Large-Eddy Simulations (LES), or

Reynolds-averaged Navier-Stokes (RANS) simulations can be used for the simulation of turbulent reacting flows. These will be discussed in further detail in Chapter 2. One challenge is that most closure models used in RANS and LES are specifically developed to be applicable for either premixed or non-premixed flames. Thus, their applicability is limited to only a set of flame features [16]. However, turbulent combustion usually involves a wide range of flame features, such as ignition, extinction, and flame front propagation. To adequately capture or predict these flame features, detailed chemistry and advanced turbulent combustion models are typically required, which can be computationally expensive.

The structure of turbulence is known to be affected by chemistry (i.e., thermal energy release). Recently, this has been studied by looking at a flame's enstrophy budget, the structure of vorticity, and backscatter [17, 18]. The effects of turbulence on chemistry, however, have received less attention and are not well understood. Studies show that under turbulent conditions, reactant pre-heating patterns could control chemical reaction pathways, which may lead to key reaction pathways that differ widely to those under laminar flame conditions [3]. Thus, investigating the effects of turbulence on chemical pathways is important. However, a broader aspect of this research is to also study the influence of chemical kinetics on turbulent flames.

There are three main mechanisms that could alter the relative contributions of the various reactions in turbulent flames compared to laminar flames. First, turbulent flames involve a significant amount of stretching. Stretch changes the local temperatures and the relative concentrations of species [19]. Second, there are different characteristic time scales associated with the different reactions. Unsteady differential diffusion effects may impact their instantaneous rates, and thus their relative role in the overall oxidation pathway [20]. And third, eddies that pierce the flame reaction zone change the flame structure by introducing a richer mix of thermochemical states, thereby potentially affecting the chemical pathways.

Despite these observations, Dasgupta et al. [20] showed that a lean premixed hydrogen-air flame oxidizes through a dominant kinetic pathway that essentially remains constant between laminar unstretched, laminar stretched, and high Karlovitz number flames. However, the study does not take into consideration complex fuels and limits the value of the largest

Karlovitz number to 36. Note that typical aerospace propulsion system configurations, such as the supersonic cavity flame holder and the shear coaxial injector, generally have much higher Karlovitz numbers (greater than 100).

Wang et al. [21] similarly studied hydrogen-air flames but looked at pressures ranging from 1 to 5 atm. The study demonstrated that compared to laminar flames, in turbulent flames, pressure changes the chemical pathways and heat release patterns. As pressure is increased in turbulent flames, the heat release from the key pressure-dependent reaction pathways decreases. In laminar flames, the heat release increases with increasing pressure. Zambon et al. [22] looked at a non-premixed ethylene-air counterflow flame at 10 atm under laminar and turbulent conditions and investigated the extinction bulk strain rate. A detailed, a reduced, and a skeletal chemical mechanism were used in the study. The latter two mechanisms were derived from the detailed mechanism. Extinction strain rates using the three mechanisms were in good agreement under laminar conditions, while large differences were observed under turbulent conditions. The detailed mechanism was further investigated by performing a chemical kinetic element flux analysis, which also highlighted the differences between chemical kinetic pathways that are triggered under laminar and turbulent flow conditions. Xu et al. studied the 3D structure of strongly turbulent premixed n-dodecane/air flames with high Karlovitz numbers using DNS, HyChem mechanisms, and the Chemical Explosive Mode Analysis (CEMA) [23]. They found that the local mode spatial distribution significantly differed to comparable flames under laminar conditions. For high Ka flames, the extinction mode was found to be equally important (if not more) as the heat release and fuel consumption rate auto-ignition modes whereas for laminar and low Ka flames, the auto-ignition mode was found to be more dominant in heat release compared to the extinction mode.

1.2 Detailed and Reduced Chemical Mechanisms in Combustion Simulations

A detailed reaction kinetic model is comprised of elementary chemical reactions and their associated rate coefficients, which come with a certain level of uncertainty. Detailed chemical kinetic mechanisms are often too large for incorporation in multi-dimensional transient flow field simulations. The large number of species and reactions, as well as the wide range of time scales, in the detailed chemical kinetics account for the computational cost in large-scale combustion simulations [24]. Figure 1.1 shows that over the years, more complex detailed mechanisms with K species and R reactions have been able to be developed. The number of reactions in these detailed mechanisms have increased in a fairly linear fashion with respect to the number of species, such that $R \approx 5K$. In order to represent the combustion of some of the larger fuels, a significant number of species and reactions are necessary. Examples of some detailed mechanisms include the well known methane-air GRI-3.0 mechanism developed by Smith et al. [25,26] which consists of 325 reactions and 53 species, the 268-step and 57-species UCSD mechanism tailored for many combustion processes from C0 to C4 [27], the HyChem mechanism developed for real multicomponent liquid fuels [28, 29], and the Foundational Fuel Chemistry Model (FFCM-1) mechanism for predicting H2, H2/CO, CH2O and CH4 combustion and developed by Hai Wang [30, 31].

Recognizing that $R \approx 5K$ [4] for most detailed chemical kinetic models, it can be observed in Figure 1.2 that, in the limit of large K, i.e., for large kinetic models, relative to the cost of the chemical rate, which is $\mathcal{O}(R) = \mathcal{O}(K)$, the computational cost for evaluating diffusion scales as $\mathcal{O}(K^2)$ while the cost for evaluating Jacobian factorization scales as $\mathcal{O}(K^3)$. As a consequence, smaller chemical mechanisms are found to be more practical in turbulent combustion simulations. Thus, detailed mechanisms are typically reduced to reaction sets that are small enough to be used in turbulent combustion simulations. There are two different reduction approaches. One involves skeletal reduction, which involves removing the non-important reactions and only leaving the pertinent reactions and species to yield a smaller skeletal mechanism. This skeletal mechanism can be reduced further through

a global reduction, in which the impact of the timescales on the reaction system is taken into account to yield a reduced mechanism. In this dissertation, a variety of chemical mechanisms for methane-oxygen combustion are investigated, ranging from detailed to skeletal to reduced. The detailed mechanisms investigated are the standard GRI-3.0 mechanism developed by Smith et al. [25, 26] and the Foundational Fuel Chemistry Model (FFCM-1) developed at Stanford University by Hai Wang [30, 31]. The skeletal mechanism in this study is the FFCM1-21 mechanism which was derived from the detailed FFCM-1 mechanism and developed by Tianfeng Lu. Lastly, the reduced mechanism used in this study is FFCMY-12, which was derived from the detailed FFCM-1 mechanism and is applicable to higher pressures (10 atm or higher). The computational cost associated with these mechanisms can be seen in Figure 1.2. It can be seen that the cost for the factorization of the Jacobian for the detailed FFCM-1 mechanism is about an order of magnitude larger than for the reduced FFCMY-12 mechanism.

The size of a reduced mechanism depends on the combustion properties of interest and the range of temperatures, pressures, and fuel and oxidizer composition. The reduced mechanism can be developed to try and predict single-combustion properties such as flame propagation or ignition at limited conditions or all combustion properties over a wider range of conditions. The latter mechanism would be larger and more versatile. However, flame ignition, propagation, and extinction are controlled by different chemical and physical parameters, some of which are not understood. Thus, it is more challenging to incorporate all these flame properties as targets, and if they are, their applicability becomes questionable. Currently, these reduced mechanisms are developed under specific laminar flow conditions in which selected global properties of a flame (e.g., ignition delay time, laminar flame speed, adiabatic flame temperature) are matched to those of the original detailed mechanism. However, this imposes restrictions on the operating range and applicability of these reduced mechanisms. For example, rocket combustors typically involve combustion with premixed, non-premixed, and partially premixed regions, as well as local extinctions and reignition and turbulence. Under turbulent conditions, there is a richer mix of thermochemical states present. In the exhaust gas recirculation (EGR) condition, there is recirculation of radicals from the burnt
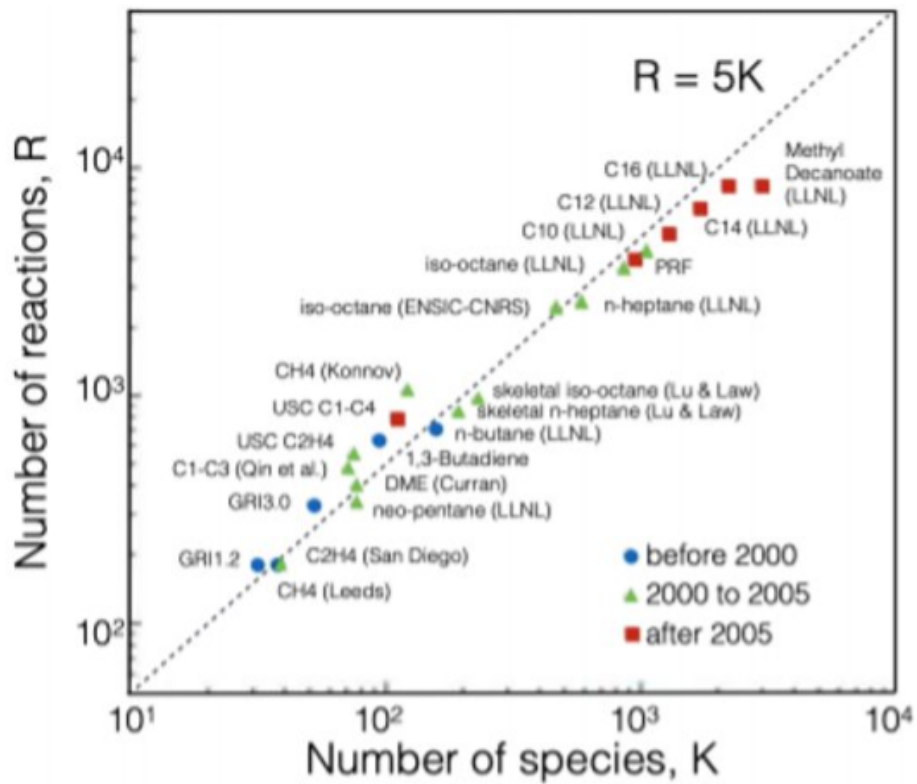
Figure 1.1: Size of selected detailed and skeletal mechanisms for hydrocarbon fuels, together with the approximate years when the mechanisms were compiled [1]
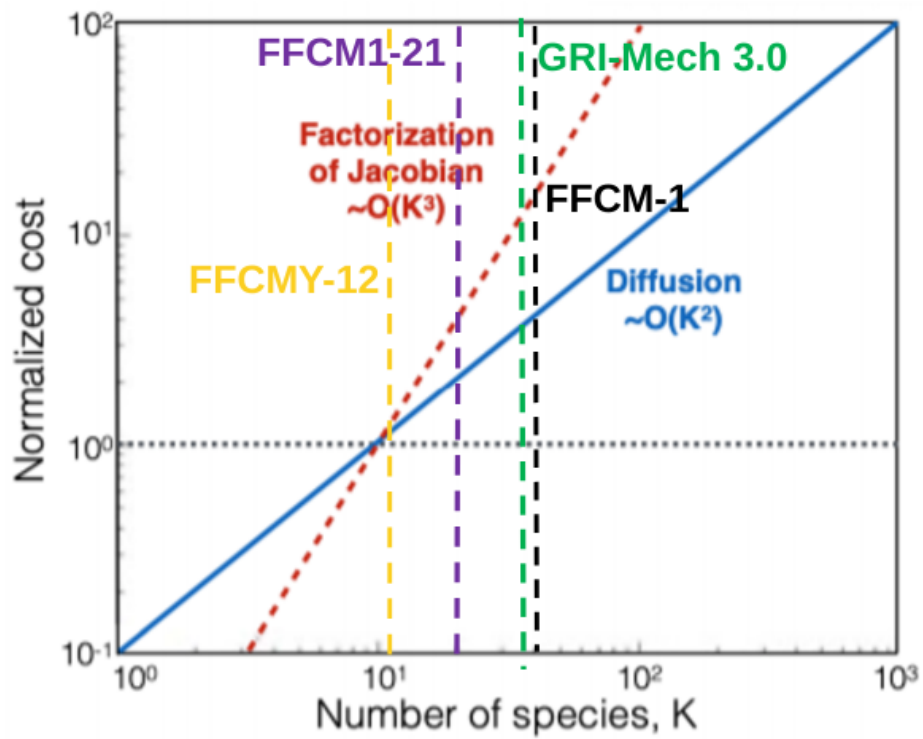
Figure 1.2: Cost for evaluating diffusion and factorization of Jacobian relative to that of chemical rate [1]

mixture into the unburnt mixture. Thus, it cannot be guaranteed that these specific laminar conditions under which reduced mechanisms are validated will be met everywhere in such a complex flowfield If turbulence is also shown to affect reduced models, then use of the model would become flow and regime specific. It may even be necessary to simulate each flow configuration with detailed chemical kinetic mechanisms before reduced models can be developed for that flow configuration. A better understanding of the sensitivities of turbulent reactive flow results is clearly needed to address these issues.

1.3   Mechanism Reduction Procedures

Several methods have been developed to help deal with large detailed chemical kinetics in flame simulations, such as skeletal reduction [1, 32–46], dynamic adaptive chemistry [47, 48], and dimension reduction [49, 50]. Skeletal reduction involves eliminating species and reactions that are not relevant or important. Thus, reasonable accuracy is maintained while significantly reducing the detailed chemical kinetic model. Many numerical methods exist to aid in skeletal reduction, including sensitivity analysis [45, 46], principal component analysis (PCA) [12, 51, 52], detailed reduction [34], the directed relation graph (DRG) method [53] and more [54]. Another approach, the dynamic adaptive chemistry (DAC) method [47], has been successfully applied in internal combustion (IC) engine [48] and other turbulent flame [55] simulations to reduce the overall computational cost.

The analysis of chemical kinetics can also involve decoupling the fast and slow timescales. Dimension reduction involves the use of a low-dimensional manifold in the composition space, which arises from species with short timescales. The canonical quasi-steady-state approximation (QSSA) [56] and partial-equilibrium approximation (PEA) [57] are two dimension reduction methods. These two approaches are often confused with one another, especially in complex chemical kinetic systems. Thus, a more systematic approach based on computational singular perturbation (CSP) has been developed. CSP decouples the slow and fast chemical modes using an iterative refinement procedure [58]. Intrinsic low-dimensional manifold (ILDM) is another way to decouple the fast processes [59]. In this approach, fast

8

processes tend towards the 'attractors' and the slow ones move within the manifolds [60]. ILDM involves an eigen-analysis and simply ignores the time dependence of the Jacobian. It also assumes that the reaction rates vanish in a transient period if they are in the direction of the fast modes. One main challenge with CSP and ILDM is that the eigen-decomposition in both is computationally expensive for the mechanism reduction and may negatively affect the computational efficiency of the simulations, especially for mechanisms involving a large number of species.

1.4 Computational Diagnostics of Complex Turbulent Flames

Several researchers have tried to analyze kinetics and investigate combustion regimes using experimental data and/or computational tools [29]. For example, researchers recently developed a combustion regime identification based on convolutional neural networks (CNNs) using the recently proposed gradient-free regime identification (GFRI) approach [61] based on the Chemical Explosive Mode Analysis (CEMA) to try and identify different combustion regimes in turbulent CH4/air jet flames [62]. Efficient computational diagnostic tools that can clearly identify different burning regimes in turbulent flames, such as the distinction between autoignition and propagation driven reaction zones, as well as compare varying kinetic mechanisms, could help bridge the gap between the governing physics and predictive turbulent combustion modeling as well as aid in the development of more accurate reduced mechanisms.

Many of the current computational diagnostic approaches rely on temperature or arbitrary species concentrations as a criteria to identify different combustion regimes. Unfortunately, chemical species and reactions that are sensitive to flame configurations, inlet and boundary conditions, the type of fuels, etc. control and determine the success of these computational diagnostic tools. Thus, these tool often lack rigor and are not universally applicable to all flame configurations, thereby requiring manual calibrations for each case.

Automated computational diagnostic tools, such as the sensitivity analysis [63], have also been developed. Global sensitivity analysis identifies important parameters or processes

using a trial and error brute-force method. In contrast, local sensitivity analysis focuses on the local sensitivity matrix. The main challenge with sensitivity analysis is that it only works on small to moderate kinetic models. This is because of the high computational cost associated with the large number of parameters, the high-dimensionality of the chemical kinetics, and the repetitive calculations of the full solution.

A more systematic computational diagnostic tool is the CSP approach. It was initially developed for solving stiff ODEs [58] and Valorani et al. [64], Najm et al. [65], and Prager et al. [66] extended it to analyze the flow and flame interactions in complex laminar flame configurations. Three types of CSP modes were identified, decoupled, and investigated, thereby revealing useful physical insights into system timescales and stiffness: fast (or exhausted) modes and slow (active/dormant) modes. Gupta et al. [67] and Pal et al. [68] used CSP to develop a criterion for the slow dynamics to identify auto-ignition regimes in Homogenous Charge Compression Ignition (HCCI) combustion with weak turbulence. A bifurcation analysis focusing on the bifurcation points on the S-curves in steady state perfectly-stirred reactors (PSRs) was also developed to identify the processes controlling ignition and extinction [69]. The bifurcation analysis, which is based on the eigen-analysis of the full Jacobian, considers both chemical and mixing source terms. Thus, it can help identify some important processes, such as reactions or mixing, which control the ignition or extinction dynamics.

Chemical Explosive Mode Analysis (CEMA) is a more recent kinetic analysis proposed by Lu et al. [2]. Through an eigenvalue analysis of the Jacobian matrix of the chemical source terms, the timescales related to chemical explosive modes (CEM) are found. The contribution of each species or elementary reaction to CEM can be determined as outlined in [2, 70, 71]. These serve as diagnostic techniques to investigate complex flame dynamics, such as auto-ignition in turbulent lifted jet flames [55, 71–74] and other advanced combustion systems [75, 76].

1.5 Turbulent Combustion Applications to Rocket Engines

A rocket injector helps mix and feed the propellants into the combustor. The propellants provide the energy and the working substance for the rocket engine. The selection of propellants affects overall engine system performance as well as the design criteria for each engine component. Many different non-premixed injector configurations are possible. One type of configuration is the single element shear coaxial rocket injector. The rocket combustion chamber converts propellants into gas at high temperature and pressure through combustion, which releases the chemical energy of the propellant. The internal energy in the gas then increases. The rocket nozzle efficiently converts the enthalpy of the combustion gases into kinetic energy, resulting in a high gas exhaust velocity.

Rocket combustors typically involve several complex and highly-coupled physical phenomena. The strong coupling creates significant challenges in the development of modern rocket engines. The current design cycle of rocket combustors involves expensive trial-and-error. Thus, it is important to make use of and obtain dependable numerical tools that can aid in the design process. To do this, it is necessary to better understand the strong coupling between the fluid dynamics, chemical kinetics, heat transfer and acoustics.

1.5.1 Rocket Injector Studies

Many studies have focused on investigating combustion instabilities. Gers et al. [77] used two-dimensional RANS to simulate a shear coaxial injector. Combustion instabilities were induced when a numerical loudspeaker provided external forcing at selected frequencies. Qualitative results showed trends in the symmetry of the velocity that were similar to the experimental results. Candel et al. [78] studied the reacting case of a high-pressure shear coaxial injector jet flame. Other cryogenic fuels, such as CH4, have also been investigated [79, 80].

Numerous researchers at AFRL/RQR experimentally studied coaxial jet flows operating in the transcritical regime, in the presence of combustion instabilites, etc [81–84]. For example, some have investigated the effects of an externally-imposed transverse acoustic field in

a flush shear coaxial jet at/near critical pressures by varying the outer to inner jet velocity ratio and outer to inner jet momentum flux ratio [85–89]. Talley also observed the dynamic response of the flame and flame holding region of a coaxial liquid oxygen gaseous hydrogen injector to open loop acoustic forcing. More generally, he explored how the presence of chemical reactions alters the behavior of coaxial shear flows in the presence of acoustic waves [90]. Harvazinski et al. [91–94] used CFD to investigate the instability mechanism present in a laboratory rocket combustor and studied the impacts of chemical mechanisms on CH4-O2 shear coaxial injectors and instabilities. He evaluated the effects of chemical kinetics mechanisms on combustion instability modeling in a methane-fueled single element rocket chamber using a single step global mechanism and a detailed mechanism in 2D and 3D simulations. In 2D, significant differences between the two predictions were identified, including the amplitude of the unsteady pressure oscillations, and more importantly, the underlying mechanisms responsible for driving the combustion instabilities. In contrast to 2D results, 3D results demonstrated negligible differences between the two predictions. This may indicate that mixing is the dominant process controlling the combustion, however, this may not be the case for other combustion phenomena, and thus, further analysis involving kinetics may be required. Miller et al. studied a single element rocket combustion injector to investigate the combustion dynamics. Results suggest that the observed instabilities are a result of the combined effects of chamber mode shape and a driving combustion mechanism that limits the frequency range over which instability occurs [95]. Yu et al. experimentally studied spontaneous longitudinal high frequency combustion instabilities in a high pressure model rocket combustor [96, 97].

Pioneering work in supercritical mixing and combustion has been performed by Oefelein and Yang [98]. Work by Lacaze and Oefelein [99] have shown that the flamelet approach can be used for the modeling of cryogenic rocket combustors. A GH2/GO2 single element injector with an optically accessible combustion chamber was studied by Foust et al. [100] using experiments and numerical simulations. They neglected effects of turbulence on reaction chemistry, and thus relied on a simplified model, a laminar finite-rate chemistry model. Foust el al. obtained fair qualitative agreement with measured species mole fractions. They

12

also achieved good quantitative agreement with the measured velocity field. However, as the distance downstream from the injector face increased, the agreement deteriorated. Oefelein [101] performed several simulations using LES and DNS approaches for fully coupled compressible governing equations to further study the effect of non-idealized thermodynamics. Results showed the near jet region to be diffusion dominated with intense property gradients approaching contact discontinuity. Note that the influences of sgs turbulence and chemical interactions are accounted for, yielding the well-known closure problem for turbulent reacting gases.

There are a few takeaways from these studies. First, the relevant phenomena to be modeled and captured in aerospace propulsion flows are flame-holding, blow-out, acoustics interactions, and ignition. It is also important to know how turbulence-chemistry interactions can impact these phenomena. Secondly, there have been few systematic studies of the influence of chemical kinetics on these major phenomena [94]. Thus, there is a need for further studies in this area.

1.5.2   Advantages of Methane Fuel in Rocket Engines

In this dissertation, the combustion of methane-oxygen is investigated. There are a few reasons for this. The first is because using methane as the fuel in a rocket has several advantages. Methane natural gas is one of the most abundant chemicals on the planet. In addition, methane fuel is easier and cheaper to refine and produce than other fuels, such as RP-1. Methane is also a cleaner burner fuel than RP-1. RP-1 generates a lot of carbon when burning, thus possibly affecting engine components. If the rocket engine is intended to be reusable, this can affect a rocket engine's ability for re-use. Rocket fuel performance is measured by the specific impulse, which indicates the amount of momentum that can be produced for every unit of fuel. Methane-oxygen combustion usually offers higher performance than karosene/LOX combustion at the same pressure. Rocket engines using methane can achieve even higher performance because they can be designed to run at much higher and more efficient pressures. With a higher specific impulse, the amount of

methane required for lift off as well as the fuel tank size decreases. In addition, lighter fuel pumps on the rocket are used, saving costs overall. For these reasons, among others, the next generation of rockets may be powered by methane. Lastly, although there have been some studies involving methane-oxygen combustion, not many have been at representative rocket engine conditions. In addition, significant works still lies ahead for understanding kinetics models for methane-oxygen combustion under these conditions.

1.6 Objectives and Overview

Chemical kinetics challenges include the large size of the mechanisms (and associated computational cost) for use in aero-propulsion systems, convergence issues due to stiffness, and strong dependencies of some intermediates on the mechanism. In addition, because chemical mechanisms are typically developed under specific laminar conditions, they are not universally applicable, such as everywhere in the flowfield for non-premixed combustion and especially under certain turbulent conditions. Furthermore, conventional computational diagnostic tools have their limitations and can be computationally expensive.

The studies highlighted above suggest that further investigations are warranted to understand if, and under what conditions, chemical kinetic pathways are altered by the interaction of turbulence with the flame. More work is needed to help delineate the applicability of reduced mechanisms. CEMA appears to be an efficient computational diagnostic tool that may give insight into the the important species and reactions in a given flowfield, and to help to explain differences that various kinetic mechanisms may produce in a reactive flowfield. Thus, CEMA may have the potential to help in the development of reduced mechanisms.

The objective of this dissertation is to gain insights into the influence of alternative chemical kinetics mechanisms on the results of turbulent combustion simulations and, specifically, the effects of these mechanisms under conditions representative of rocket injector applications. The CEMA method is then applied to simpler 0D and 1D cases that are relevant to the more complex 2D combustion problem. The remainder of the dissertation is organized as follows. Chapter 2 goes over the computational framework, including the equations of mo-

tion, equation of state, thermodynamic and transport properties, turbulence and combustion models, and numerics. Chapter 3 investigates the global effects of turbulence and reaction mechanisms at different spatial and temporal resolutions using a realistic configuration, a 2D shear coaxial injector and explores further motivation for the need of a computational diagnostic tool like CEMA. Chapter 4 goes over the CEMA framework in more detail and validates the CEMA module for a one-dimensional premixed flame configuration. Chapter 5 applies the CEMA framework to 0D homogeneous combustion to verify that the conclusions from 0D reflect what is already known about laminar combustion and to learn more about what to expect in a related but more complex turbulent data set, such as 2D or 3D CFD data sets.

CHAPTER 2

Computational Framework

In this chapter, the computational framework for reacting flows is outlined. Several 0D simulations as well as all 1D and 2D simulations in this dissertation were carried out using the in-house computational framework named General Equation Mesh Solver, or GEMS for short [102]. GEMS uses an implicit finite volume scheme with second order time and space accuracy to solve equations for momentum, continuity, and energy, along with turbulence and species transport equations.

With the inclusion of combustion processes, the Navier-Stokes equations and energy conservation become considerably more complex. Heat release from combustion results in an increase in temperature. Thermodynamic data is more complex in a reacting gas because of the changes in temperature and composition. In addition, an increase in temperature accelerates combustion chemistry. Moreover, a larger number of species are usually part of the mixture when many chemcial reactions are involved. These species react chemically, and the the associated reaction rates require modelling. The transport coefficients of the mixture of gases, such as heat diffusivity, species diffusivity, and viscosity, also require attention. These important differences are shown in detail below.

2.1   Conservation Equations

The governing equations in vector form for a system with N species and in three-dimensions are,

$$\frac{\partial \mathbf{Q}}{\partial t} + \frac{\partial \mathcal{F}_i}{\partial x_i} - \frac{\partial \mathcal{F}_{v,i}}{\partial x_i} = \mathbf{H} \tag{2.1}$$

where $\mathbf{Q}$ represents the vector of conserved variables,

$$\mathbf{Q} = \begin{pmatrix} \rho & \rho u & \rho v & \rho w & \rho e & \rho Y_\ell \end{pmatrix}^\top, \tag{2.2}$$

The first entry of each vector in Equation 2.1 corresponds to conservation of mass, or continuity. The second, third, and fourth entries correspond to the momentum equations. For the momentum equations, the two terms on the left hand side represent the local rate of change and convection of momentum, respectively. The third term is the pressure gradient and the fourth term is the molecular transport due to viscosity. The fifth entry of each vector in Equation 2.1 corresponds to the energy equation, and the final entry corresponds to the species conservation equations. Some of the computations using the $k - \omega$ DES model which involves additional transport equation. These are presented in a later section.

Note, ρ is the mixture density and u, v, and w are the x, y, and z component fluid flow velocities, respectively. To represent ρe, the total energy, e first can be written in terms of h^0 (stagnation enthalpy) and p (pressure),

$$e = h^0 - \frac{p}{\rho}. \tag{2.3}$$

Thus, the energy ρe, found in $\mathbf{Q}$, can be obtained by substitution. Y_ℓ is the ℓ species mass fraction, where if mass conservation is included, as shown above, then ℓ varies from 1 to $N - 1$.

Referring back to Equation 2.1, the inviscid and viscous fluxes are $\mathcal{F}$ and $\mathcal{F}_v$, respectively. Decomposing the invscid flux into components along each coordinate axis, i:

$$\mathcal{F}_i = \begin{pmatrix} \rho u_i \\ \rho u u_i + \delta_{1i} p \\ \rho v u_i + \delta_{2i} p \\ \rho w u_i + \delta_{3i} p \\ \rho u_i h^0 \\ \rho u_i Y_\ell \end{pmatrix} \tag{2.4}$$

17

Similarly, decomposing the viscous flux into components along each coordinate axis, i:

$$\mathcal{F}_{v,i} = \begin{pmatrix} 0 \\ \tau_{xi} \\ \tau_{yi} \\ \tau_{zi} \\ u_j \tau_{ji} - q_i \\ -\rho V_{i,\ell} Y_\ell \end{pmatrix} \tag{2.5}$$

$V_{i,\ell}$ is the diffusion velocity, the velocity of species ℓ in the ith direction. The diffusion can be approximated using the Hirshfelder and Curtiss first order approximation [103],

$$Y_\ell \vec{V}_\ell \approx -\mathcal{D}_{\ell M} \nabla Y_\ell \tag{2.6}$$

where the equivalent diffusion coefficient of species ℓ into the rest of the mixture is

$$\mathcal{D}_{\ell M} = \frac{1 - X_\ell}{\sum_{i \neq \ell}^{N} \frac{X_i}{\mathcal{D}_{i\ell}}} \tag{2.7}$$

The heat flux in the ith direction, q_i, is,

$$q_i = -K \frac{\partial T}{\partial x_i} + \rho \sum_{\ell=1}^{n} V_{i,\ell} Y_\ell h_\ell + \mathcal{Q}. \tag{2.8}$$

Using the dynamic (molecular) viscosity and the velocity components, the viscous tensor, τ_{ij}, is defined as,

$$\tau_{ij} = \mu \left(\frac{\partial u_i}{\partial x_j} + \frac{\partial u_j}{\partial x_i} - \frac{2}{3} \frac{\partial u_m}{\partial x_m} \delta_{ij} \right). \tag{2.9}$$

where δ_{ij} is the Kronecker symbol. Note, $\delta_{ij} = 1$ if $i = j$, and $\delta_{ij} = 0$ otherwise.

The remaining term in Equation 2.1 is the source term, $\mathbf{H}$, which describes the production (positive) or destruction (negative) for each species ℓ,

$$\mathbf{H} = \begin{pmatrix} 0 & 0 & 0 & 0 & 0 & \dot{\omega}_\ell \end{pmatrix}^\top. \tag{2.10}$$

For two-dimensional axisymmetric simulations, the momentum equation in the radial direction is present. This results in a source term which includes additional terms and is represented as,

$$\mathbf{H} = \begin{pmatrix} 0 & 0 & p + \mu \left(2\frac{v}{y} - \frac{2}{3} \nabla \cdot \mathbf{u} \right) & 0 & \dot{\omega}_\ell \end{pmatrix}^\top. \tag{2.11}$$

18

2.2 Equation of State

The ideal gas equation of state used can be written as,

$$\rho = \frac{pW_\ell}{RT} \tag{2.12}$$

where R is the universal gas constant and W_ℓ is the molecular weight of species ℓ.

Using the species mass fraction, the molecular weight of the mixture can be calculated,

$$W^{-1} = \sum_{\ell=1}^{N} \frac{Y_\ell}{W_\ell} \tag{2.13}$$

The mixture density is,

$$\rho = \left(\sum_{\ell=1}^{N} \frac{Y_\ell}{\rho_\ell} \right)^{-1} \tag{2.14}$$

Tabulated data is used to determine the thermodynamic and transport properties of the mixture. Note that the mixture property formulas are written in terms of the mole fraction X_ℓ. The following equation can be used to convert between mass and mole fractions,

$$X_\ell = Y_\ell \left(\frac{W}{W_\ell} \right) \tag{2.15}$$

2.2.1 Thermodynamic Properties

McBride et al. tabulated thermodynamic properties for a wide range of species and temperatures [104]. Specefic heats, enthalpy, and entropy are calculated using polynomials that are composed from coefficients that are tabulated,

$$\frac{h_\ell}{RT} = -\frac{a_1}{T^2} + \frac{a_2}{T} \ln T + a_3 + \frac{a_4}{2} T + \frac{a_5}{3} T^2 + \frac{a_6}{4} T^3 + \frac{a_7}{5} T^4 + \frac{a_8}{T} \tag{2.16}$$

$$\frac{s_\ell}{R} = -\frac{a_1}{2T^2} - \frac{a_2}{T} + a_3 \ln T + a_4 T + \frac{a_5}{2} T^2 + \frac{a_6}{3} T^3 + \frac{a_7}{4} T^4 + a_9 \tag{2.17}$$

The mixture enthalpy and entropy are

$$h = \sum_{i=1}^{N} h_i Y_i \tag{2.18}$$

The total enthalpy can also be calculated

$$h^0 = h + \frac{1}{2} \mathbf{u} \cdot \mathbf{u} \tag{2.19}$$

19

2.2.2 Transport Properties

McBride et al. tabulates transport properties such as viscosity μ and thermal conductivity K data, which is needed to solve the equations of motion [105] Similar to enthalpy, they can be computed using the following equations,

$$\left.\begin{array}{c} \ln\mu \\ \ln K \end{array}\right\} = A\ln T + \frac{B}{T} + \frac{C}{T^2} + D \tag{2.20}$$

(the constants are found in the tabulated data). Using Wilke's law for gas mixtures, the mixture viscosity is calculated [106]

$$\mu = \sum_{\ell=1}^{N} \frac{X_\ell \mu_\ell}{\phi_\ell} \tag{2.21}$$

where the parameter, ϕ_ℓ is,

$$\phi_\ell = \frac{1}{2\sqrt{2}} \sum_{n=1}^{N} X_n \left[1 + \left(\frac{\mu_\ell}{\mu_n}\right)^{1/2} \left(\frac{W_n}{W_\ell}\right)^{1/4} \right]^2 \left(1 + \frac{W_\ell}{W_n} \right)^{-1/2} \tag{2.22}$$

Mathur et al. outlines the mixing rule for thermal conductivity [107],

$$K = \frac{1}{2} \left[\sum_{\ell=1}^{N} X_\ell K_\ell + \left(\sum_{\ell=1}^{N} X_\ell K_\ell^{-1} \right)^{-1} \right] \tag{2.23}$$

2.3 Turbulence Modeling

Because turbulence is inherently three-dimensional (3D), unsteady, and involves a wide range of scales, numerically computing it and resolving all the scales become a challenge. In CFD, there are three main types of simulations that are usually carried out: Direct Numerical Simulations (DNS), Large Eddy Simulations (LES) and Reynolds Averaged Navier-Stokes (RANS). DNS involves numerically solving the full Navier-Stokes equations directly and DNS requires sufficiently small temporal and spatial resolutions in order to capture all the turbulent scales (smallest to largest eddies) that are present in a given flow. This can be computationally expensive and is not feasible for large multi-physics and multi-scale simulations applicable to high Reynolds number flows and complex geometries, which is typical of

many engineering problems. For these cases, using a turbulence model is a necessary choice. LES and RANS are two popular turbulence modeling approaches, both of which are less expensive than DNS.

In LES, large scale motions (large eddies) of a turbulent flow are resolved and small scale (sub-grid scale (SGS)) motions are modeled. This results in a significant decrease in computational cost compared to DNS. In RANS simulations, averaged quantities are solved and all instantaneous turbulence is modelled by a turbulence model. Thus, RANS averaged mean quantities involve averages over regions in physical space that are of the order of the integral scale. This, along with the fact that the grid can be coarser than with DNS and LES, makes the RANS approach less computationally expensive than the DNS and LES approaches. The smaller computing requirement has made RANS the preferred approach for industrial CFD applications. Although this seems great, RANS simulations tend to be inaccurate for highly unsteady flowfields, given that knowledge of the transients is necessary in order to accurately predict flow behaviour. In addition, the turbulence model requires fine-tuning several parameters for each specific problem [108]. Note that compared to RANS, LES are more accurate since LES resolve the large eddies. These large eddies contain a large portion of the turbulent energy and also induce most of the momentum transfer and turbulent mixing. In contrast, all of the large eddies are modelled in the RANS approach. Furthermore, the small scales that are modelled in LES are usually more isotropic and homogeneous than the large scales. This makes it easier to model the SGS motions in LES compared to modelling all turbulent scales using the RANS approach. Also, in LES, filtering is done over regions smaller than the integral length scale. This results in different mean values and smaller variances than with RANS. Therefore, although LES do not resolve all turbulent scales like DNS do and they have a larger computational cost compared to RANS, LES are currently the most adequate approach for simulating realistic turbulent flows.

In order to address the LES issues associated with computational cost and wall functions in near-wall regions, a hybrid LES-RANS approach called Detached Eddy Simulations (DES) can be used. In DES, the RANS approach is used in regions where insufficient resolution in time and/or space prevent the large turbulent scales to be captured (near-wall boundary

layer region) and the LES approach is used in the rest of the flowfield, where grid and time resolution is able to capture the large turbulent eddies. The core flame is typically found within the LES region. Note, the 2D GEMS computations in this work use the DES approach. In the DES approach to modeling turbulence, Reynolds averaging is applied to the governing equations such that flow variables are decomposed into mean and perturbation in time components. This is used in particular for density and pressure using the following form

$$\alpha(\vec{x}, t) = \langle \alpha(\vec{x}, t) \rangle + \alpha'(\vec{x}, t) \tag{2.24}$$

where the mean value is defined as,

$$\langle \alpha(\vec{x}, t) \rangle = \frac{1}{\Delta t} \int_{t}^{t+\Delta t} \alpha(\vec{x}, t') dt' \tag{2.25}$$

For flows with large density changes such as in combustion, it is convenient to use a density-weighted average, otherwise known as the Favre average. For example, in the momentum equations, along with the temperature and species conservation equations, the convective terms are typically dominant for high Reynolds number flows. Since these terms contain products of dependent variables with density, Favre averaging is the preferred method to use. Favre averaging is typically used to split velocity, enthalpy and temperature into a turbulent fluctuations, $\alpha''(\vec{x}, t)$, and the mean flow, $\widetilde{\alpha(\vec{x}, t)}$, such that,

$$\alpha(\vec{x}, t) = \widetilde{\alpha(\vec{x}, t)} + \alpha''(\vec{x}, t) \tag{2.26}$$

By definition, Favre averaging is defined by requiring that the mean of density weighted fluctuation approaches zero. In other words,

$$\left\langle \rho(\vec{x}, t) \widetilde{\alpha(\vec{x}, t)} \right\rangle = 0 \tag{2.27}$$

Thus, the mean component may be derived by multiplying Equation 2.28 by ρ and then averaging,

$$\widetilde{\alpha(\vec{x}, t)} = \frac{\langle \rho(\vec{x}, t) \alpha(\vec{x}, t) \rangle}{\langle \rho(\vec{x}, t) \rangle}. \tag{2.28}$$

Once Favre averaging is applied, the vector of conserved variables now becomes,

$$\langle Q \rangle = \left(\langle \rho \rangle \quad \langle \rho \rangle \, \widetilde{u} \quad \langle \rho \rangle \, \widetilde{v} \quad \langle \rho \rangle \, \widetilde{w} \quad \langle \rho \rangle \, \widetilde{h}^0 - \langle p \rangle \quad \langle \rho \rangle \, \widetilde{Y}_\ell \right). \tag{2.29}$$

Some of the computations using the $k - \omega$ DES model which involves additional transport equation, which are presented in a later section. The Favre-averaged inviscid flux vectors are now defined in terms of the Farve-averaged variables,

$$
E = \begin{pmatrix} \langle \rho \rangle \, \widetilde{u} \\ \langle \rho \rangle \, \widetilde{u}^2 + \langle p \rangle \\ \langle \rho \rangle \, \widetilde{uv} \\ \langle \rho \rangle \, \widetilde{uw} \\ \langle \rho \rangle \, \widetilde{uh}^0 \\ \langle \rho \rangle \, \widetilde{uY}_\ell \end{pmatrix}
\quad
F = \begin{pmatrix} \langle \rho \rangle \, \widetilde{v} \\ \langle \rho \rangle \, \widetilde{uv} \\ \langle \rho \rangle \, \widetilde{v}^2 + \langle p \rangle \\ \langle \rho \rangle \, \widetilde{vw} \\ \langle \rho \rangle \, \widetilde{vh}^0 \\ \langle \rho \rangle \, \widetilde{vY}_\ell \end{pmatrix}
\quad
G = \begin{pmatrix} \langle \rho \rangle \, \widetilde{w} \\ \langle \rho \rangle \, \widetilde{uw} \\ \langle \rho \rangle \, \widetilde{vw} \\ \langle \rho \rangle \, \widetilde{w}^2 + \langle p \rangle \\ \langle \rho \rangle \, \widetilde{wh}^0 \\ \langle \rho \rangle \, \widetilde{wY}_\ell \end{pmatrix}. \tag{2.30}
$$

The viscous flux vectors are shown below and now include several additional terms. These

new terms require modelling,

$$
E_{v,x} = \begin{pmatrix}
0 \\
\widetilde{\tau_{xx}} - \langle\rho\rangle\,\widetilde{u''^2} \\
\widetilde{\tau_{yx}} - \langle\rho\rangle\,\widetilde{u''v''} \\
\widetilde{\tau_{zx}} - \langle\rho\rangle\,\widetilde{u''w''} \\
\widetilde{u}\widetilde{\tau_{xx}} + \widetilde{v}\widetilde{\tau_{yx}} + \widetilde{w}\widetilde{\tau_{zx}} - \widetilde{q}_x - \langle\rho\rangle\left(\widetilde{u}\widetilde{u''^2} + \widetilde{v}\widetilde{u''v''} + \widetilde{w}\widetilde{v''w''} + \widetilde{u''e''}\right) \\
- \langle\rho\rangle\left(\widetilde{V_{x,\ell}}\widetilde{Y}_\ell + \widetilde{u''Y_\ell''}\right)
\end{pmatrix}
$$

$$
F_{v,y} = \begin{pmatrix}
0 \\
\widetilde{\tau_{xy}} - \langle\rho\rangle\,\widetilde{v''u''} \\
\widetilde{\tau_{yy}} - \langle\rho\rangle\,\widetilde{v''^2} \\
\widetilde{\tau_{zy}} - \langle\rho\rangle\,\widetilde{v''w''} \\
\widetilde{u}\widetilde{\tau_{xy}} + \widetilde{v}\widetilde{\tau_{yy}} + \widetilde{w}\widetilde{\tau_{zy}} - \widetilde{q}_y - \langle\rho\rangle\left(\widetilde{u}\widetilde{v''u''} + \widetilde{v}\widetilde{v''^2} + \widetilde{w}\widetilde{v''w''} + \widetilde{v''e''}\right) \\
- \langle\rho\rangle\left(\widetilde{V_{y,\ell}}\widetilde{Y}_\ell + \widetilde{v''Y_\ell''}\right)
\end{pmatrix}
\tag{2.31}
$$

$$
G_{v,z} = \begin{pmatrix}
0 \\
\widetilde{\tau_{xz}} - \langle\rho\rangle\,\widetilde{w''u''} \\
\widetilde{\tau_{yz}} - - \langle\rho\rangle\,\widetilde{w''v''} \\
\widetilde{\tau_{zz}} - \langle\rho\rangle\,\widetilde{w''^2} \\
\widetilde{u}\widetilde{\tau_{xz}} + \widetilde{v}\widetilde{\tau_{yz}} + \widetilde{w}\widetilde{\tau_{zz}} - \widetilde{q}_z - \langle\rho\rangle\left(\widetilde{u}\widetilde{u''w''} + \widetilde{v}\widetilde{v''w''} + \widetilde{w}\widetilde{w''^2} + \widetilde{w''e''}\right) \\
- \langle\rho\rangle\left(\widetilde{V_{z,\ell}}\widetilde{Y}_\ell + \widetilde{w''Y_\ell''}\right)
\end{pmatrix}
$$

Note, the mean heat flux is written as as,

$$
\widetilde{q}_i = -K\frac{\partial\widetilde{T}}{\partial x_i} + \langle\rho\rangle\sum_{\ell=1}^{N}\langle V_{\ell,i}\rangle\,\widetilde{Y}_\ell\,\langle h_\ell\rangle.
\tag{2.32}
$$

The Boussinesq eddy viscosity approximation can be used to model the Reynolds stress, $\widetilde{u_i''u_j''}$ in the DES. Modelling it involves using a turbulent viscosity, ν_t, such that,

$$
\mathcal{R}_{ij} = -\widetilde{u_i''u_j''} = \nu_t\left(\frac{\partial\widetilde{u}_i}{\partial x_j} + \frac{\partial\widetilde{u}_j}{\partial x_i} - \frac{2}{3}\frac{\partial\widetilde{u}_\ell}{\partial x_\ell}\delta_{ij}\right) - \frac{2}{3}k\delta_{ij}
\tag{2.33}
$$

where k is the turbulent kinetic energy, which is half of the trace of the Reynolds stress,

$$
k = \frac{1}{2}\text{tr}\left(\mathcal{R}_{ij}\right) = \frac{1}{2}\sum_{i=1}^{3}\widetilde{u_i''^2}.
\tag{2.34}
$$

24

Note, a gradient-diffusion model can be used to model the fluctuation terms that contain species mass fractions and energy.

Using the turbulent viscosity and a turbulent Prandtl number, the energy equation term is closed,

$$\widetilde{u_i'' e''} = -\frac{\nu_t}{\Pr_t} \frac{\partial \widetilde{h}}{\partial x_i}. \tag{2.35}$$

Similarly, the species transport equation is closed using a turbulent Schmidt number and the turbulent viscosity,

$$\widetilde{u_i'' Y_\ell''} = -\frac{\nu_t}{\mathrm{Sc}_{t,\ell}} \frac{\partial \widetilde{Y}_\ell}{\partial x_i}. \tag{2.36}$$

Note, the turbulent Prandlt and Schmidt numbers are assigned as constants.

2.4 Turbulence Equations

The new terms that were introduced as a result of applying Reynolds decomposition were closed using the turbulent kinetic energy and eddy viscosity, which typically need to be either specified or modelled. One popular approach to model these quantities is the Wilcox two-equation k-ω model [109], a system of two conservation equations for the turbulent kinetic energy, k and the turbulent dissipation, ω. The eddy viscosity can be written in terms of the turbulent kinetic energy and dissipation,

$$\nu_t = \frac{k}{\widetilde{\omega}} \tag{2.37}$$

where $\widetilde{\omega}$ is the shear stress limited dissipation,

$$\widetilde{\omega} = \max \left(\omega, \frac{7}{8} \sqrt{\frac{2 S_{ij} S_{ij}}{\beta^\star}} \right). \tag{2.38}$$

The two conservation equations to be solved for the turbulent kinetic energy and dissipation are, respectively,

$$\frac{\partial (\langle \rho \rangle k)}{\partial t} + \nabla \cdot (\langle \rho \rangle \widetilde{u} k) = \langle \rho \rangle \tau_{ij} \frac{\partial \widetilde{u}_i}{\partial x_j} - \beta^\star k \omega + \frac{\partial}{\partial x_j} \left(\left(\mu + \sigma^\star \frac{\langle \rho \rangle k}{\omega} \right) \frac{\partial k}{\partial x_j} \right) \tag{2.39}$$

25

Table 2.1: k-ω turbulence model parameters

Parameter	Value
γ	$13/25$
β	$\beta_0 f_\beta$
β_0	0.0708
$\beta^\star$	$9/100$
σ	$1/2$
$\sigma^\star$	$3/5$
σ_d	0 for $\frac{\partial k}{\partial x_j}\frac{\partial \omega}{\partial x_j} \leq 0$, otherwise $1/8$
χ_ω	$\left\lvert \Omega_{ij}\Omega_{kj}\widehat{S_{ki}}/(\beta^\star\omega)^3 \right\rvert$
$\widehat{S_{ki}}$	$S_{ki} - \frac{1}{2}\frac{\partial u_\ell}{\partial x_\ell}\delta_{ki}$
f_β	$(1+85\chi_\omega)/(1+100\chi_\omega)$

and,

$$\frac{\partial(\langle\rho\rangle\,\omega)}{\partial t} + \nabla \cdot (\langle\rho\rangle\,\widetilde{u}\omega) = \gamma\frac{\langle\rho\rangle\,\omega}{k}\tau_{ij}\frac{\partial\widetilde{u}_i}{\partial x_j} - \langle\rho\rangle\,\beta\omega^2$$
$$+ \langle\rho\rangle\,\frac{\sigma_d}{\omega}\frac{\partial k}{\partial x_j}\frac{\partial\omega}{\partial x_j} + \frac{\partial}{\partial x_j}\left(\left(\mu + \sigma\frac{\langle\rho\rangle\,k}{\omega}\right)\frac{\partial\omega}{\partial x_j}\right). \quad (2.40)$$

In these equations, the first term on the left hand side is the local rate of change and the second term is convection. The values for modeling parameters in these turbulence model equations are given in Table 2.1. Note, the turbulent length scale used with the k-ω model is,

$$L_\mathrm{T} = \frac{k^{1/2}}{\beta^\star\omega}. \quad (2.41)$$

The second term on the right hand side of the equation for turbulent kinetic energy, Equation 2.39 can be rewritten in terms of the turbulent length,

$$\beta^\star k\omega = \frac{k^{3/2}}{L_\mathrm{T}}. \quad (2.42)$$

26

In DES, the turbulent length scale is compared with the grid size in order to determine the value of the length in the turbulent kinetic energy equation. In the LES region, the grid size is used as the turbulent length scale while in the RANS region, the length scale is calculated using Equation 2.41.

Mathematically,the length is defined as,

$$L_T^\star = \min\left(L_T, C_{DES}\Delta\right) \tag{2.43}$$

where Δ is taken as the maximum grid dimension for the cell and C_{DES} uses a recommended value of 0.78.

2.5   Chemical Kinetics

In reaction flow simulations, the chemical mechanism is one of the data inputs that is needed. Kinetics data properties can have a significant effect on the computation results.

Writing the set of conservation equations as,

$$\frac{\partial Q}{\partial t} + \frac{\partial E_i}{\partial x_i} - \frac{\partial F_{vi}}{\partial x_i} = H \tag{2.44}$$

the vector Q is the list of conserved variables, E_i and F_{vi} are the inviscid and viscous flux vectors, respectively. Vector H involves the remaining source terms, such as the chemical source terms from the elementary reactions. Modeling of the mean chemical source term is often considered one of the biggest challenges in turbulent combustion. Each chemical reaction is written as [110],

$$\nu'_{j,k}\chi_j \xrightleftharpoons[K_b]{K_f} \nu_{j,k}''\chi_j \tag{2.45}$$

where χ are the species in the reaction (reactants and products), K_f and K_b are the forward and reverse rates of a reaction k, respectively, while ν are stoichiometric coefficients of jth species in the reaction.

Chemical mechanisms can either involve elementary or global reactions. Global reactions represent the net effect of multiple reaction processes. Elementary reactions are typically reversible and usually are a larger set than the global reaction mechanism. Although they

differ, the Arrhenius form for the reaction rates is used in both types,

$$K_f = AT^b e^{\frac{-E_a}{RT}} \tag{2.46}$$

where A, b are constants, T is temperature, E_a is the activation energy and R is the universal gas constant.

Reaction rates for global reactions represent the fuel consumption rate. Detailed chemical mechanisms usually involve sets of elementary reactions. The reaction rates in these elementary reactions are non-linear functions of temperature, concentration, and pressure..

The forward rate is determined first, and then the reverse reaction rate is obtained using the equilibrium constant K_{eq}. The equilibrium constant can be written in terms of species concentrations as,

$$
\begin{aligned}
K_{eq} &= \frac{\prod_{j=1}^{N_{spc}} [\chi_j]^{\nu_j''}}{\prod_{j=1}^{N_{spc}} [\chi_j]^{\nu_j'}} \left(\frac{R_u T_{ref}}{P_{ref}} \right)^{\sum \nu'' - \sum \nu'} \\
&= \frac{K_f}{K_b} \left(\frac{R_u T_{ref}}{P_{ref}} \right)^{\sum \nu'' - \sum \nu'}
\end{aligned}
\tag{2.47}
$$

where R_u is the universal gas constant (molar units) and $[\chi_i]$ are species concentrations $(Kmol/m^3)$. The equilibrium constant is,

$$K_{eq} = e^{-\frac{\Delta G^0}{R_u T}} \tag{2.48}$$

where G^0 is the Gibbs free energy of formation of a species at some chosen reference condition,

$$G^0 = \left(h^0 - T s^0 \right)_{ref} \tag{2.49}$$

Note, h^0 and s^0 are enthalpy and entropy of formation of each species. Thus, for the kth reaction,

$$\Delta G_k^0 = \sum_{j=1}^{N} \left(\nu_{j,k}'' G_j^0 - \nu_{j,k}' G_j^0 \right). \tag{2.50}$$

The backward reaction rate K_b is found using equations 2.48 and 2.47. Note that all the elementary reactions have to considered to calculate the overall species source terms, $\dot{\omega}$. The species source terms can be written as [110],

$$q_{\text{progf}-\text{k}} = k_f \prod_i [\chi]_i^{\nu_{ik}'} \tag{2.51a}$$

28

Table 2.2: All kinetic mechanisms used in this study

	GRI-Mech 3.0	FFCM-1	FFCM1-21	FFCMY-12	WD-9	Dryer
Type	Detailed	Detailed	Skeletal	Reduced	Reduced	Reduced
Combustion Type	CH4-O2	CH4-O2	CH4-O2	CH4-O2	CH4-O2	H2-Air
No. Species	36	38	22	13	9	13
No. Steps	218	291	107	38	7	35

$$q_{\text{progb}-\text{k}} = k_b \prod_i [\chi]_i^{\nu_{ik}''} \tag{2.51b}$$

where q_{prog} is the progress of reaction k. The net reaction rate, $[NRR]$, can be found using the forward and reverse rates,

$$[NRR] = q_{\text{progf}} - q_{\text{progb}} \tag{2.52}$$

Lastly, the species production (or destruction) vector is calculated,

$$\dot{\Omega} = [\dot{\omega}_1, \dot{\omega}_2 \ldots \dot{\omega}_j]^T = [\nu'' - \nu']^T [NRR] [MW_j]^T \tag{2.53}$$

MW_j is added to maintain consistency in units.

Table 2.2 shows all the chemical mechanisms used in this dissertation. All are for methane-oxygen combustion except the Dryer mechanism, which is used for hydrogen-air combustion [111]. Also, they span from detailed to skeletal to reduced mechanisms. The GRI-Mech 3.0 mechanism is a standard detailed kinetic model for hydrocarbon and methane combustion. Reactions involving nitrogen were removed to reduce computational cost [25,26]. The Foundational Fuel Chemistry Model (FFCM-1) is a detailed kinetic model developed at Stanford by Hai Wang [30,31]. FFCM-1 was optimized for H2, H2/CO, CH2O and CH4 combustion and incorporated combustion data such as laminar flame speeds, shock tube ignition delay times, shock tube species profiles, and flow reactor species profiles. In addition, other kinetic uncertainties were further analyzed using extinction and ignition residence time predictions in perfectly-stirred reactor conditions. FFCM-1 uses more up-to-date kinetic data and more well-defined predictive uncertainties than GRI-Mech 3.0 and has been investigated

under relevant engine conditions [112]. FFCM1-21 is a skeletal kinetic model derived by Tianfeng Lu from the detailed FFCM-1 mechanism. FFCMY-12 is a reduced kinetic model derived from FFCM-1. It is optimized for high pressures (10 atm or above). Westbrook Dryer(WD-9) is a reduced mechanism from HyPerComp Inc. for CH4-O2 combustion in rocket engines. Lastly, the Dryer mechanism was used in this study to validate 1D H2-Air premixed propagating flame with CEMA [111].

2.6 Numerical Scheme

A finite-volume dual-time scheme is used for GEMS [113]. The dual-time scheme means that for each physical time step, a select number of pseudo-time iterations are performed to improve the likelihood of convergence. Note that once convergence is reached, the pseudo derivative term disappears and only the original conservation equations remain. Since the pseudo time derivative will vanish, one need not use the vector of conserved variables Q. Assuming that no discontinuities exist, it is preferable to use primitive variables Q_p over conservative variables. This is because working with primitive variables is easier, faster, and generally gives more accurate results. Primitive variables are defined as,

$$\mathbf{Q}_p = \begin{pmatrix} p & u & v & w & T & Y_\ell \end{pmatrix}^\top.$$ (2.54)

2.6.1 Spatial Discretization

In GEMS, Roe Flux Difference Splitting is mainly used to calculate the flux at a face of each computational cell.

At $i + 1/2^{th}$ face of ith cell, the flux is,

$$E_{i+1/2} = \frac{1}{2}\left(E_i + E_{i+1}\right) - \frac{1}{2}\left(\left|\frac{\partial E}{\partial Q_p}\frac{\partial Q_p}{\partial Q}\right|\frac{\partial Q}{\partial Q_p}\delta Q\right)_{i+1/2}$$ (2.55)

In terms of Jacobian Γ, this can be written as,

$$E_{i+1/2} = \frac{1}{2}\left(E_i + E_{i+1}\right) - \frac{1}{2}\left(\left|A\Gamma^{-1}\right|\Gamma\right)_{i+1/2}\delta Q_{i+1/2}$$ (2.56)

and if $|CB| \, A = A \, |BC|$, then,

$$E_{i+1/2} = \frac{1}{2} \left(E_i + E_{i+1} \right) - \frac{1}{2} \left(\Gamma \left| \Gamma^{-1} A \right| \right)_{i+1/2} \delta Q_{i+1/2} \tag{2.57}$$

where the eigenvalue and right eigenvector matrix can be used to rewrite matrix $\left| \Gamma^{-1} A \right|$ as,

$$\left| \Gamma^{-1} A \right|_{i+1/2} = \left(R \left| \Lambda \right| R^{-1} \right)_{i+1/2} \tag{2.58}$$

The Roe averaging method can be used to conserve fluxes and determine dissipation while flux directions. For denisty, velocity, and enthalpy, this is written as,

$$\rho_{i+1/2} = \sqrt{\rho_i \rho_{i+1}} \tag{2.59}$$

$$u_{i+1/2} = \frac{u_i \sqrt{\rho_i} + u_{i+1} \sqrt{\rho_{i+1}}}{\sqrt{\rho_i} + \sqrt{\rho_{i+1}}} \tag{2.60}$$

$$h_{i+1/2} = \frac{h_i \sqrt{\rho_i} + h_{i+1} \sqrt{\rho_{i+1}}}{\sqrt{\rho_i} + \sqrt{\rho_{i+1}}} \tag{2.61}$$

$$\tag{2.62}$$

Similarly, the other variables have a similar process to that for velocity and enthalpy.

2.6.2   Temporal Discretization

GEMS has the option to use first-order accuracy or second-order time discretization to approximate physical time derivative.

First-order accuracy time discretization is shown as,

$$\frac{\partial \mathbf{Q}}{\partial t} = \frac{\mathbf{Q}^{n+1} - \mathbf{Q}^n}{\Delta t}, \tag{2.63}$$

and second-order accuracy time discretization is,

$$\frac{\partial \mathbf{Q}}{\partial t} = \frac{3\mathbf{Q}^{n+1} - 4\mathbf{Q}^n + \mathbf{Q}^{n-1}}{2\Delta t}. \tag{2.64}$$

Note, the spatial derivative is discretized using finite volume and flux schemes.

A pseudo-time derivative can be introduced into Eq. 2.1 to solve the system of equations. Starting from an initial condition, this iterative variable can be marched until convergence

31

is reached. $\frac{\partial \mathbf{Q_P}}{\partial \tau}$ eventually disappears as pseudo time approaches infinity, thereby having no effect on the final solution. Thus, it can be written in non-conservative form as,

$$\mathbf{\Gamma}_p \frac{\partial \mathbf{Q_P}}{\partial \tau} + \frac{\partial \mathbf{Q}}{\partial t} + \frac{\partial \mathcal{F}_i}{\partial x_i} - \frac{\partial \mathcal{F}_{v,i}}{\partial x_i} = \mathbf{H} \tag{2.65}$$

First order accuracy discretization is sufficient to approximate the pseudo time derivative above,

$$\frac{\partial \mathbf{Q}_p}{\partial \tau} = \frac{\mathbf{Q}_p^{n+1} - \mathbf{Q}_p^n}{\Delta \tau} \tag{2.66}$$

2.7 CHEMKIN Computational Framework

The CHEMKIN chemical kinetics package [114] was used to compute the time evolution of a homogeneous reacting gas mixture in a closed system. This enabled the extraction of information, such as temperature and species profiles, which are time-dependent. CHEMKIN is suitable for dealing with stiff chemical kinetics problems, where species conservation equations have widely varying magnitudes in source terms and associated chemical timescales,. This is because it uses implicit, multistep methods. Within CHEMKIN, the thermodynamic conditions can be varied and externally imposed to solve six different problem types

- A constant pressure adiabatic system

- A constant volume adiabatic system

- A time-dependent volume adiabatic system

- A constant pressure and constant temperature system

- A constant volume and constant temperature system

- A time-dependent pressure and time-dependent temperature system

All 0D simulations presented here involved a constant volume adiabatic assumption (the second case listed above). In this section, the governing equations are described for this problem, as well as a brief discussion of the numerical methods and program structure.

2.7.1   Governing Equations

As mentioned previously, CHEMKIN is used to investigate a reacting mixture in a closed system with no mass crossing the boundary. The total mass of the mixture is

$$m = \sum_{\ell=1}^{N} m_\ell \tag{2.67}$$

where m_ℓ is the mass of species ℓ. This total mass is constant, thus, $\frac{dm}{dt} = 0$. The production or destruction of each species is determined by

$$\frac{dm_\ell}{dt} = V\dot{\omega}_\ell W_\ell \tag{2.68}$$

where t is time, $\dot{\omega}_\ell$ is the molar production rate of the ℓ-th species for each elementary reaction, W is the molecular weight of the ℓ-th species, and V is the total volume of the system. Using the fact that the total mass is constant, the equation above can be written in terms of the mass fractions as

$$\frac{dY_\ell}{dt} = \nu\dot{\omega}_\ell W_\ell \tag{2.69}$$

where Y_ℓ is the mass fraction of the ℓ-th species and $\nu = V/m$ is the specific volume. Note for the constant volume case, the energy equation must be derived. In an adiabatic closed system, the first law of thermodynamics for a pure substance states that

$$de + pd\nu = 0 \tag{2.70}$$

where e is the internal energy per mass and p is the pressure. The internal energy of the mixture is given by

$$e = \sum_{\ell=1}^{N} e_\ell Y_\ell \tag{2.71}$$

where e_ℓ is the internal energy of the ℓ-th species. The internal energy of the mixture can then be differentiated, resulting in

$$de = \sum_{\ell=1}^{N} Y_\ell de_\ell + \sum_{\ell=1}^{N} e_\ell dY_\ell \tag{2.72}$$

For a calorically perfect gas, $de_\ell = c_{v,\ell} dT$, where T is the temperature of the mixture, and c_ν, is the specific heat of the ℓ-th species at constant volume. The mean mixture specific heat is

$$c_\nu = \sum_{\ell=1}^{N} Y_\ell c_{\nu,\ell} \tag{2.73}$$

The expression can be differentiated with respect to time, leading to the following energy equation

$$c_\nu \frac{dT}{dt} + \sum_{\ell=1}^{N} e_\ell \frac{dY_\ell}{dt} + p\frac{d\nu}{dt} = 0 \tag{2.74}$$

Using the expression 3.2 for the species production rate yields

$$c_\nu \frac{dT}{dt} + p\frac{d\nu}{dt} + \nu \sum_{\ell=1}^{N} e_\ell \dot{\omega}_\ell W_\ell = 0 \tag{2.75}$$

To obtain the pressure, the ideal gas equation of state is used. Recall, in these 0D simulations, the volume is held constant. Thus, Eq. 3.9 simplifies to

$$c_\nu \frac{dT}{dt} + \nu \sum_{\ell=1}^{N} e_\ell \dot{\omega}_\ell W_\ell = 0 \tag{2.76}$$

The net chemical production rate, $\dot{\omega}_\ell$, of each species is computed using all the chemical reactions involving that species. The law of mass action dictates the way each reaction proceeds, with the forward rate coefficients written in the modified Arrhenius form, as specified earlier.

The initial value problem for each of the different cases formulated above requires initial conditions for the temperature, pressure, and composition of the mixture. The equation

of state is used to compute the initial density. Because these variables are intensive, the problem is not dependent on the absolute quantity of mixture.

2.7.2 Numerical Methods

The set of ordinary differential equations mentioned previously is stiff. Thus, an implicit approach can be used to efficiently solve them. The time integration and a sensitivity analysis (first-order) can be performed using a differential/algebraic system solver using a backward differentiation formula (BDF). BDF methods are often used to solve stiff chemical kinetics problems. The details of the numerical methods are described by [115]. In this document, only main features of the sensitivity methods are briefly outlined.

2.7.3 Program Structure

To solve a problem using CHEMKIN, the user first executes the preprocessor program, "chem". This program helps CHEMKIN obtain user-supplied information, such as the species and chemical reactions, involved in a particular reaction mechanism. It also extracts thermodynamic properties and data from the "therm.dat" database file. CHEMKIN then reads the inputs specified directly by the user. The user input information and thermodynamic properties are stored in the CHEMKIN Linking File, "chem.asc". This file is later used by the CHEMKIN subroutine library to solve the specified problem.

CHAPTER 3

2D Rocket Injector

As mentioned in Chapter 1, the goal of this dissertation is to study the effects of turbulence on chemistry and, specifically, on different mechanisms under conditions representative of rocket injector applications. To investigate global effects of turbulence and reaction mechanisms using a realistic configuration, a 2D shear coaxial injector, typical of injector geometries in liquid rocket engines (LREs), was studied. This type of injector has been studied before by UCLA and AFRL/RQR researchers before [81–89]. As mentioned previously, researchers have also investigated the effects kinetic mechanisms on combustion instabilities in a shear coaxial injector configuration [93, 94, 116]. The injector used in this study is similar to one that will be developed and experimentally tested at the Air Force Research Laboratory in the near future. Thus, these simulations are also used to guide the development of the injector. The shear coaxial rocket injector configuration was also chosen because it provides a great environment to study turbulent combustion and investigate the effects of kinetics on phenomena such as shear layer instabilities, flame holding, and acoustic oscillations. Another key advantage of coaxial jets is that as the Momentum Flux Ratio (MFR) between the outer and inner jet increases, mixing of the two fluids within the coaxial jet also increases. Thus, only short distances from the exit plane are necessary to obtain a uniform mixture [97]. The preliminary focus of the numerical studies in this chapter is on evaluating the impact of chemical kinetics and turbulent-chemistry interactions on simulation results for a range of operating conditions. Three chemical mechanisms for methane-oxygen combustion in a single element shear coaxial rocket injector are explored, with focus on global effects, such as mixing, flame anchoring location, flame length, and blowout, as well as detailed properties of the flame.

3.1 Geometric Configuration

Figure 3.1a shows the configuration for the single element shear coaxial rocket injector explored in these computations. The injector geometry is based on the continuously variable resonance chamber (CVRC) geometry explored at Purdue University, which accommodates a reaction of gaseous methane and oxygen at variable pressure conditions. A complete description of the experiment can be found in [97]. A few simplifications have been made so that the geometry can be represented using a two-dimensional axisymmetric geometry for the present computational study. The geometry is based on the CVRC experiment and was reduced to a smaller scale that is better suited for detailed large eddy simulations (LES) and that also corresponds to the experimental lab-setup at AFRL/RQR.

Figure 3.1a also shows some of the flow dynamics associated with the injector. Cold fuel and hot oxidizer enter in a coaxial fashion upstream of the backstep. Fuel enters through the smaller inlet while oxidizer enters through the larger inlet. Mixing of the two fluids then occurs, leading to a shear layer composed of the cold fuel and warm oxidizer. In addition, hot combustion products become trapped in a recirculation zone near the backstep, which interacts with the cold shear layer. This can affect the state of the mixture and the corresponding heat release significantly. Figure 3.1 shows the full combustor. A nozzle was added to prevent flow back into the exit boundary.

3.2 Mesh, Boundary Conditions, and Operating Conditions

In this study, the computational domain covers the entire full geometry shown in Figure 3.1. The mesh can be seen in Figure 3.2. The two-dimensional baseline grid contains approximately one hundred thousand grid points, with an average spatial resolution in the injector portion of the domain of approximately 0.03 mm by 0.03 mm and a time step of $0.1\mu s$. A grid resolution study was performed in which the total number of grid elements was increased from the baseline case of one hundred thousand grid points to a finer case of approximately three hundred thousand grid points and the time step was decreased to
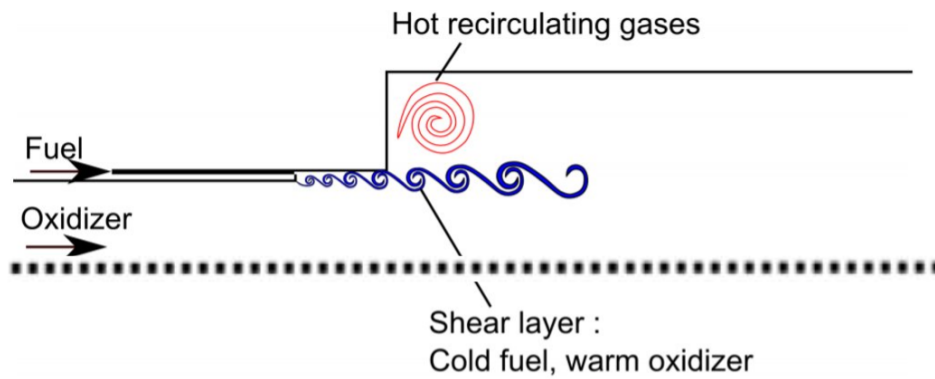
(a) Injector Schematic and Flow Dynamics [93]

(b) Full Combustor Schematic

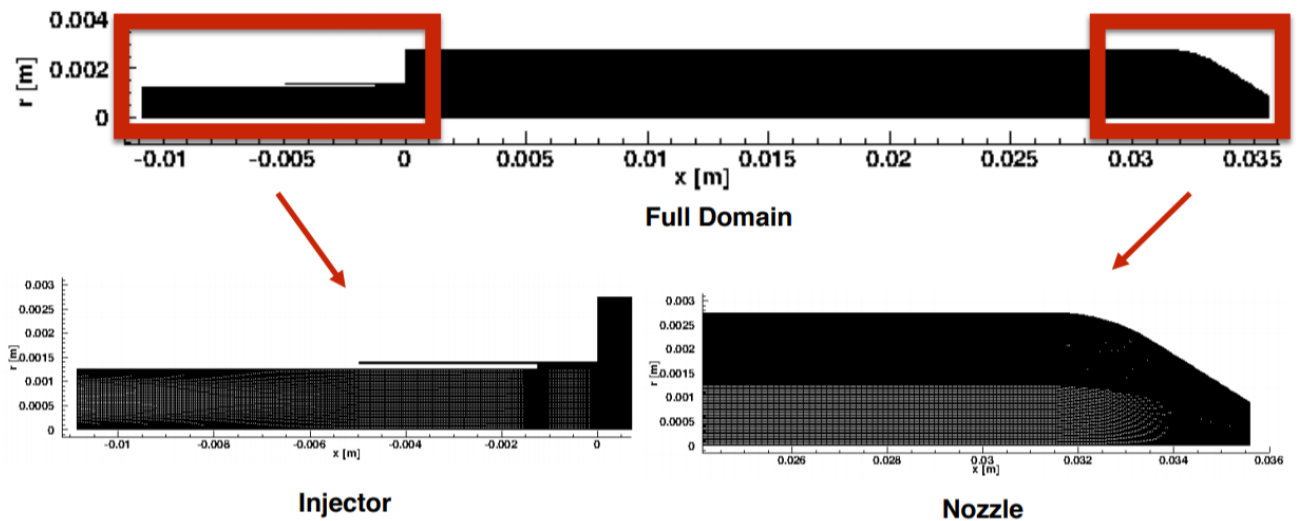Figure 3.1: Injector and Combustor Geometry (units in mm)

Figure 3.2: 2D mesh for geometry

Table 3.1: 2D spatial and temporal resolution for various cases

	Baseline	Finer Grid
No. Cells	100,000	300,000
Spatial Resolution	0.03×0.03 mm	0.015×0.015 mm
Temporal Resolution	0.1 μs	0.05 μs

$0.05\mu s$, as shown in Table 3.1.

Resolving the boundary layers along the injector surfaces typically requires a large number of grid points in a numerical simulation. Near the wall, the grid must be refined so that the first grid point is $y+$, a non-dimensional unit, value of unity away from the wall. In addition to the small cell size required near the wall, the grid needs to slowly coarsen away from the wall to capture the large gradients present in the boundary layer. This leads to cells near the wall that are densely packed. The cell aspect ratio controls the cell size in the stream-wise direction. Usually an aspect ratio of 1000 is used within the boundary layer. The inlet boundary conditions for the propellants are defined using the mass flow rate, species mass fractions, and the stagnation temperature of the propellants. All walls have the no-slip and adiabatic conditions specified there. Axisymmetry is enforced along the centerline, and the outlet backpressure is set to 20 atm.

A range of operating conditions has been studied in an axisymmetric coaxial injector configuration [94, 117] with different kinetic mechanisms for the combustion of methane and oxygen. Some of the non-dimensional parameters used in this study include the Reynolds number, which represents the ratio of inertial to viscous forces, the global equivalence ratio, which is below unity for a fuel lean mixture and above unity for a fuel rich mixture, the fuel-to-oxidizer density and velocity ratios, and the fuel-to-oxidizer Momentum Flux Ratio (MFR).

Tables 3.2-3.3 show the operating conditions for the simulation cases that were performed. Note that for all cases, a chamber pressure of 20 atm, inlet fuel temperature of 300 K, and inlet oxidizer temperature of 1000 K was used. In the group of tests labeled Set 1 (Table

Table 3.2: Operating conditions for Set 1 simulation cases. Vary fuel mass flow rate (velocity varies; density and area remain constant) and keep oxidizer mass flow rate constant.

Fuel MF [kg/s]	Ox MF [kg/s]	Fuel Re	Ox Re	ϕ	Density Ratio (F/O)	Velocity Ratio (F/O)	MFR (F/O)
3.26E-05	5.21E-04	320.27	2.77E06	0.25	1.72	0.41	0.29
6.52E-05	5.21E-04	640.3	2.77E06	0.5	1.72	0.82	1.16
1.30E-04	5.21E-04	1280.6	2.77E06	1.0	1.72	1.64	4.64
1.96E-04	5.21E-04	1920.8	2.77E06	1.5	1.72	2.47	10.44
2.61E-04	5.21E-04	2561.0	2.77E06	2.0	1.72	3.29	18.56

Table 3.3: Operating conditions for Set 2 simulation cases. Keep fuel mass flow rate constant (equal to value at stoichiometric from Set 1) and vary oxidizer mass flow rate (velocity varies; density and area remain constant) such that ratios remain the same as in Set 1.

Fuel MF [kg/s]	Ox MF [kg/s]	Fuel Re	Ox Re	ϕ	Density Ratio (F/O)	Velocity Ratio (F/O)	MFR (F/O)
1.30E-04	2.09E-03	1280.6	1.11E07	0.25	1.72	0.41	0.29
1.30E-04	1.04E-04	1280.6	5.52E06	0.5	1.72	0.82	1.16
1.30E-04	5.21E-04	1280.6	2.77E06	1.0	1.72	1.64	4.64
1.30E-04	3.48E-04	1280.6	1.84E06	1.5	1.72	2.47	10.44
1.30E-04	2.62E-04	1280.6	1.38E06	2.0	1.72	3.29	18.56

Table 3.4: Operating conditions for Set 1 simulation cases in this study

Fuel MF [kg/s]	Ox MF [kg/s]	Fuel Re	Ox Re	ϕ	Density Ratio (F/O)	Velocity Ratio (F/O)	MFR (F/O)
3.26E-05	5.21E-04	320.27	2.77E06	0.25	1.72	0.41	0.29

Table 3.5: Operating conditions for Set 2 simulation cases in this study

Fuel MF [kg/s]	Ox MF [kg/s]	Fuel Re	Ox Re	ϕ	Density Ratio (F/O)	Velocity Ratio (F/O)	MFR (F/O)
1.30E-04	2.62E-04	1280.6	1.38E06	2.0	1.72	3.29	18.56

Table 3.6: Kinetic mechanisms used in 2D study

	Type 1	Type 2	Type 3
Kinetic Mechanism	WD-9	GRI-Mech 3.0	FFCM1-21
No. Species	9	36	22
No. Steps	7	218	107

3.2), the oxidizer mass flow rate was held constant while the fuel mass flow rate was varied in order to achieve momentum flux ratios of 0.29 to 18.56, with fuel-oxidizer equivalence ratios of 0.25 to 2.0. In Set 2, the fuel mass flow rate was held constant (matched to the value corresponding to the stoichiometric case in Set 1) while the oxidizer mass flow rate was varied in order to achieve the same momentum flux ratios and equivalence ratios. Two cases of interest were chosen for this study, which are shown in Tables 3.4-3.5. They involve a low MFR case from Set 1 (MFR = 0.29) and a high MFR case from Set 2 (MFR = 18.56). Note, the length scales used to calculate the inlet oxidizer and fuel Reynolds numbers are the radius of the oxidizer inlet and the width of the annulus for the fuel inlet, respectively.

3.3   Chemistry

In this study, a laminar combustion closure of the chemical source terms is implemented using three alternative chemical kinetic mechanisms, as shown in Table 3.6.

- Modified Westbrook and Dryer (WD-9) (developed by HyPerComp, Inc)

- Foundational Fuel Chemistry Model, reduced version (FFCM1-21) [30, 31]

- GRI Mech-3.0 [25, 26]

The WD-9 mechanism contains seven reactions and nine species, as indicated in Table 3.6. It was further developed by HyPerComp Inc. and calibrated to predict the combustion of methane-oxygen for rocket applications. The modified WD-9 mechanism is a relatively simple reduced mechanism, and not expected to perform as well as the other two kinetics mechanisms.

GRI Mech-3.0 is another chemical mechanism explored in this study. Note that reactions involving nitrogen were removed from GRI-Mech to reduce the computational cost of the simulations while eliminating unnecessary reactions. GRI-Mech has been used extensively in the combustion community and has typically been regarded as the standard for hydrocarbon and methane combustion simulations. Yet several studies have noted GRI-Mech-3.0's limited performance certain extreme conditions, such as those at very high pressures and temperatures as relevant to rocket engines [118]. FFCM1-21 is a skeletal kinetic model of 107 reactions and 22 species developed to represent combustion of small hydrocarbon fuels [30, 31]. It is derived from the detailed FFCM-1 chemical mechanism of 291 reactions and 38 species that uses up-to-date kinetic data and well-defined predictive uncertainties. A key objective with the FFCM endeavor is to identify weaknesses within current kinetic knowledge and data in order to improve kinetic models and help direct future research directions. At present FFCM-1 and FFCM1-21 are designed to predict H2, H2/CO, CH2O and CH4 combustion only. In this 2D study, the FFCM1-21 (107 reactions, 22 species) is used (reduction by Tienfeng Lu), which has been optimized for CH4-O2 combustion. For the 0D study, which will be discussed in detail in the following chapter, the detailed mechanism, FFCM-1 (38 species, 291 reactions), was also be explored, as well as a reduced mechanism, FFCMY-12 (13 species, 38 reactions), which is a reduced mechanism and meant for high pressures only (10 atm and above).

3.4   Results and Discussion

Results are shown for the scaled-down shear-coaxial methane-gaseous oxygen injector that corresponds to element designs to be tested at AFRL. The preliminary focus of the numerical studies is on evaluating the impact of chemical kinetics and turbulent-chemistry interactions on simulation results for a range of operating conditions. In exploring the influences of the three chemical mechanisms on methane-oxygen combustion in a single element shear coaxial rocket injector, focus was placed on global effects, such as mixing, flame anchoring location, flame length, and blowout, as well as detailed properties of the flame.
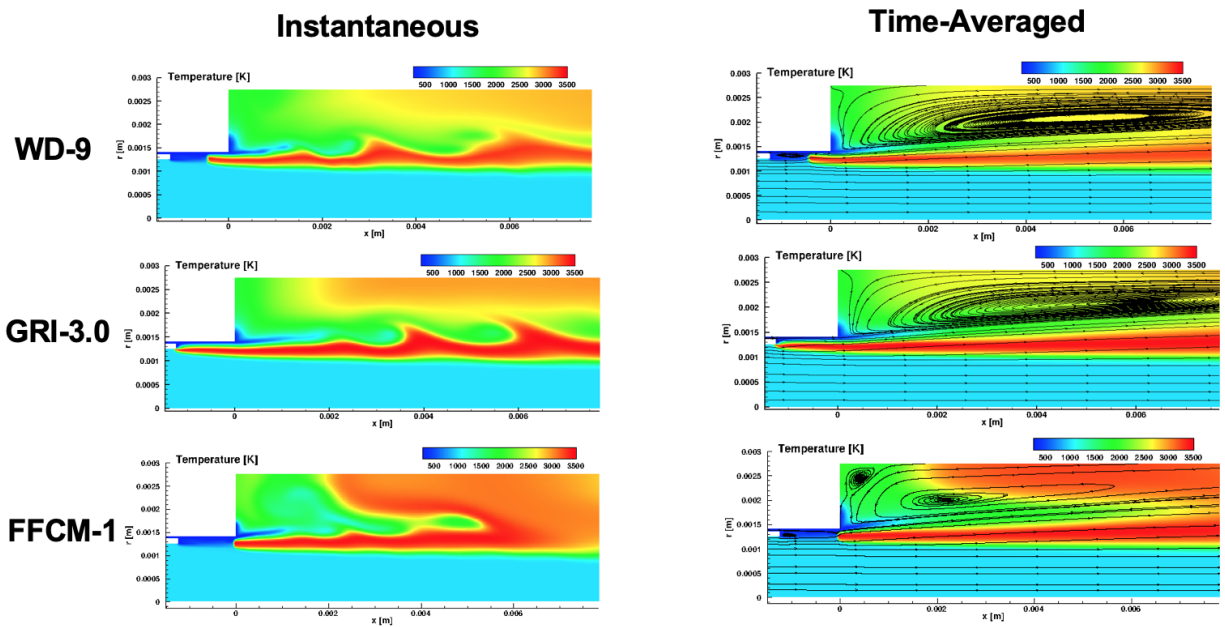
Figure 3.3: Instantaneous and time-averaged temperature field for all three chemical mechanisms at a low momentum flux ratio, MFR = 0.29, with baseline grid and temporal resolution.
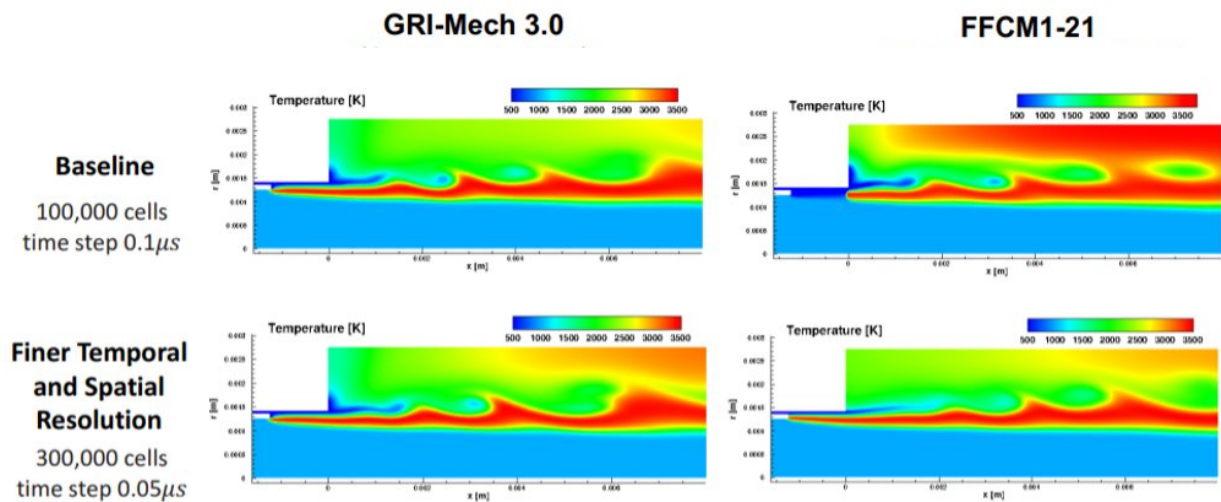

Figure 3.4: Instantaneous temperature contours for shear-coaxial methane-oxygen injector using GRI-Mech (left) and FFCM1-21 (right) for fuel-oxidizer momentum flux ratio of 0.29. Top row is for the baseline grid as shown in Figure 3.3, bottom row has finer spatial and temporal grid resolution.
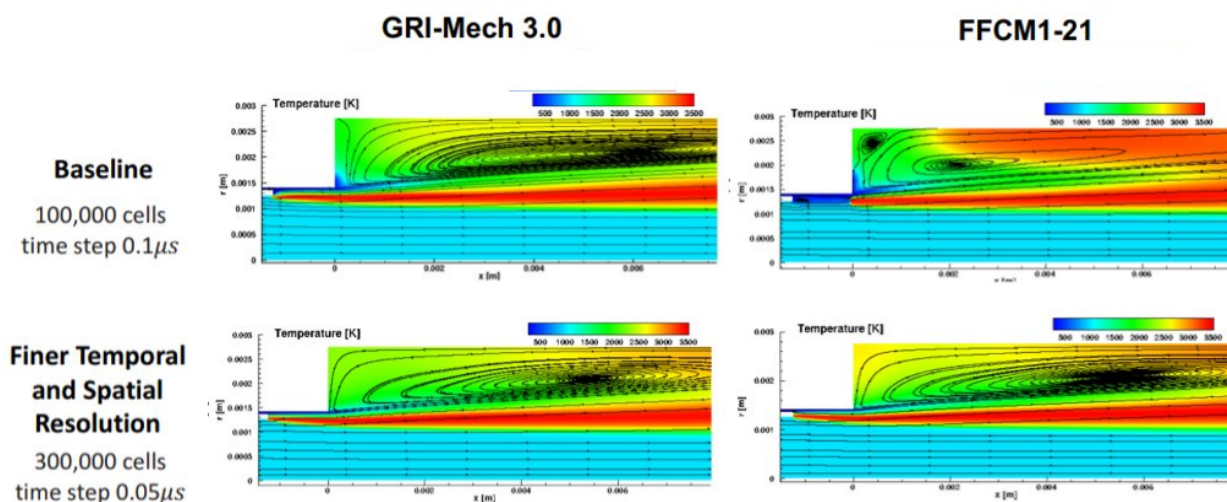
43

Figure 3.5: Average temperature contours for shear-coaxial methane-oxygen injector using GRI-Mech (left) and FFCM1-21 (right) for fuel-oxidizer momentum flux ratio of 0.29. Top row is for the baseline grid as shown in Figure 3.3, bottom row has finer spatial and temporal grid resolution.
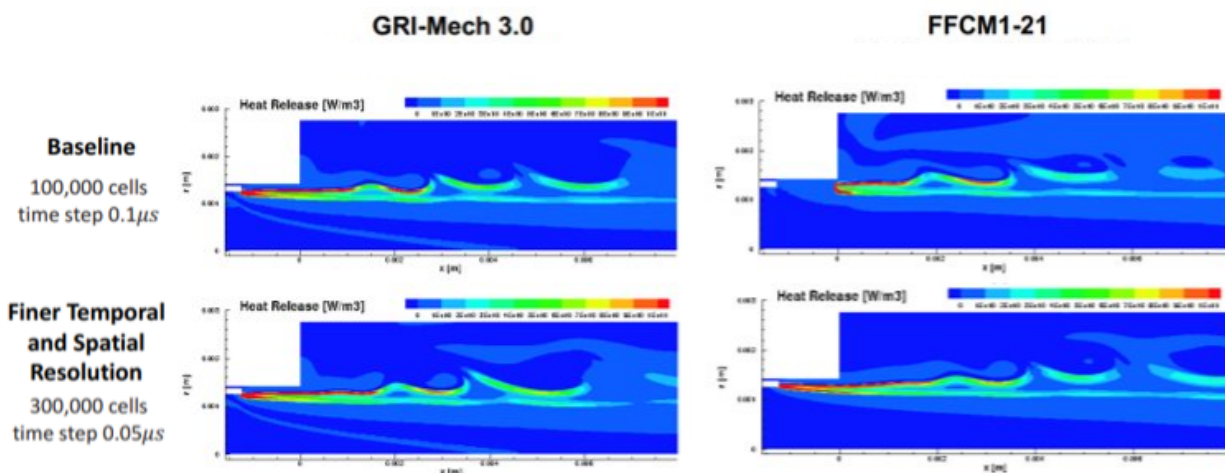

Figure 3.6: Instantaneous heat release contours for shear-coaxial methane-oxygen injector using GRI-Mech (left) and FFCM1-21 (right) for fuel-oxidizer momentum flux ratio of 0.29. Top row is for the baseline grid as shown in Figure 3.3, bottom row has finer spatial and temporal grid resolution.

44

Taking a close look at the differences in the flame anchoring locations, Figure 3.3 shows the instantaneous and time-averaged temperature contour plots for the three chemical mechanisms for the low momentum flux ratio case, MFR = 0.29. It is evident that each chemical mechanism yields a different flame anchoring location. GRI-Mech 3.0 yields a flame anchoring location very close to the splitter plate (separating the fuel and oxidizer inlets), and the flame anchors somewhat closer to the oxidizer side than the fuel side. This flame anchoring location was expected based on the higher temperature of oxidizer than fuel at injection. In contrast, the FFCM1-21 mechanism results in a flame anchoring location downstream of injection, at the dump plane into the combustor rather than at the splitter plate. The flow recirculation and flame structure also differ somewhat between GRI-Mech and the FFCM1-21 mechanism, even at this low momentum flux ratio case, indicating an effect of the kinetics on the flow itself, in addition to effects of the altered flowfield on reaction processes. Results for the WD-9 mechanism show that the flame anchors in between the splitter plate separating the fuel and oxidizer inlets and the dump plane into the main combustor region. The anchoring location for the flame using the WD-9 mechanism is closer to that of GRI-Mech, and the high temperature region near the wall due to the large recirculation region is similar to that for GRI-Mech. FFCM1-21 yields the highest temperature and a recirculation region that differs from those for the other cases near the wall.

The effects of grid and temporal resolution in the simulations are explored in Figure 3.4 for GRI-Mech and FFCM1-21, for the same F/O momentum flux ratio of 0.29. The top row shows results on the baseline grid and the bottom row results are obtained with half the grid and time-step sizes. While the finer grid and smaller time step had a relatively minor effect on the temperature field (instantaneous and time-averaged) predicted by GRI-Mech 3.0, the improved resolution had a more significant influence on the results with the FFCM1-21 mechanism. As shown in Figure 3.4, with the smaller time step alone, the flame anchoring location predicted by the FFCM1-21 mechanism moved slightly upstream from the dump plane. Adding a finer grid, the flame anchoring location predicted by the FFCM1-21 mechanism moved even further upstream from the dump plane, close to the reactant injection location at the splitter plate, now similar to that predicted by GRI-Mech. The

instantaneous temperature field for FFCM1-21 also became much closer to that for GRI-Mech with finer spatial and temporal resolution. Hence it is important to ensure a converged solution when comparing the various mechanisms in studies such as this. Figure 3.5 shows the time-averaged temperature field for the cases in Figure 3.4 and good agreement is shown. It can also be observed from the time-averaged plots that the FFCM1-21 case exhibits two recirculation zones (a small one and a large one) near the wall for the baseline case, but then converges to one large recirculation zone for the higher resolution case, thus agreeing with that of GRI-Mech 3.0.

Instantaneous heat release results for this case seem to agree with the instantaneous temperature field results in Figure 3.4. One notable observation is that the largest heat release seems to be concentrated at the corresponding flame anchoring locations, with a larger region being concentrated there for GRI-Mech compared to FFCM1-21. In the shear layer region, the largest heat release is found more on the fuel side rather than the oxidizer side for both mechanisms, however, it seems to span a greater distance for GRI-Mech than FFCM1-21. Lastly, just as with the instantaneous field temperature contours, instantaneous heat release contours seem to match for both mechanisms as the time-step and grid resolution is increased.

A power spectral density (PSD) analysis was performed to try and gain a quantitative understanding of the nature of the unsteadiness. Figure 3.7 shows a PSD analysis using FFCM1-21 for fuel-oxidizer momentum flux ratio of 0.29 at two locations. The first location is at x = 2mm and r = 1.25mm, in the shear layer region. The second one is at x = 2mm and r = 1.75mm, in the recirculation zone near the wall. Although some minor differences are observed among the different time-step and grid resolutions, overall there seems to be an agreement, and both exhibit some noise. In addition, unsteadiness or significant instabilities are not observed, possibly indicating that these cases are fairly stable. Although not shown here, results for GRI-Mech show a similar behavior. An equivalent analysis will be performed for temperature and species mass fractions, since these quantities may be more sensitive than pressure.

Figure 3.8 shows the instantaneous and time-averaged temperature contour plots for the
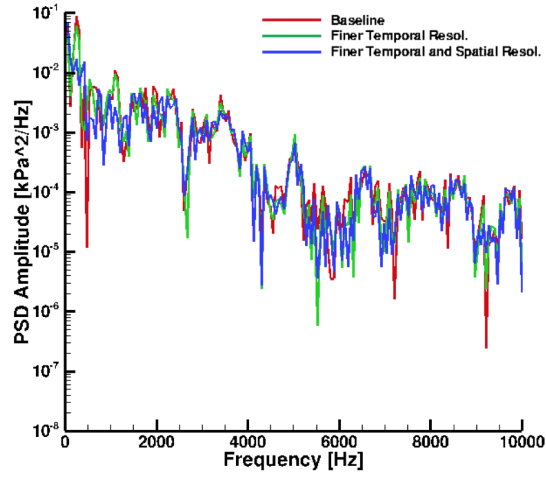
(a) x = 2mm and r = 1.25mm (shear layer)
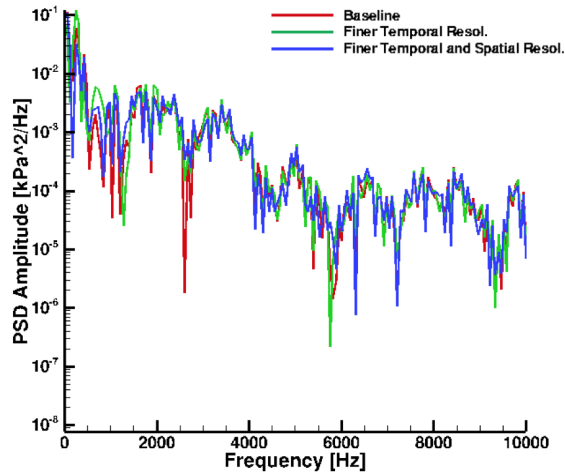
(b) x = 2mm and r = 1.75mm (near wall recirculation region)

Figure 3.7: Power spectral density analysis using FFCM1-21 for fuel-oxidizer momentum flux ratio of 0.29 at two locations. Red is for the baseline grid, green is for the same spatial resolution but higher temporal resolution, and blue is for higher spatial and temporal resolution.

three chemical mechanisms for the high momentum flux ratio case, corresponding to MFR = 18.56. For this baseline resolution condition, there were $100,000$ grid points ($\Delta x = 0.03$ mm) and a time step of $0.1\mu m$. In contrast to the low momentum flux ratio case shown in Figure 3.3, the high momentum flux ratio case shows a larger difference in the flame anchoring location and behavior amongst the three chemical mechanisms. The flame predicted by GRI-Mech 3.0 anchors at the splitter plate, and on the oxidizer side, as in the low momentum flux ratio case, again consistent with a higher temperature for the oxidizer at injection. And while the instantaneous temperature field shown for GRI-Mech 3.0 suggests a lower overall temperature in Figure 3.8, the time-averaged field actually shows the highest temperatures in the vicinity of flameholding and beyond the dump plane, in contrast to a lower average temperature for the other cases, especially that produced by the FFCM1-21 mechanism. Interestingly, the flame corresponding to the FFCM1-21 mechanism is not anchored; it is a lifted flame. The flame has a significantly different flame anchoring location than the other two flames, including the one corresponding to the WD-9 mechanism, which anchors upstream of the dump plane. The larger differences in this high MFR case compared to the low MFR case are due to the fact that the higher MFR case has a higher velocity fuel jet. This can lead to greater unsteadiness, especially with shedding that can occur due to the backstep. For all three mechanisms, the mean flow structure consists of two recirculation zones downstream of the dump plane rather than one, as observed for the MFR = 0.29 case in Figure 3.3. The higher speed flow appears to create more distorted flame structures which do not heat the interior of the chamber to the extent observed for the low momentum ratio case in Figure 3.3.

The influence of temporal and spatial grid resolution on the instantaneous temperature field is shown, for example, in Figure 3.9 for the GRI-Mech 3.0 and FFCM1-21 simulations with a higher F/O momentum flux ratio of 18.56. Interestingly, with a smaller time step, there is a negligible effect on the flame structure and anchoring for either mechanism (in contrast to that seen for the lower MFR condition for the FFCM1-21 case in Figure 3.4. But when a finer spatial resolution is incorporated for each simulation, the flame anchoring location moves downstream, toward the dump plane, for the GRI-Mech 3.0 simulation, while
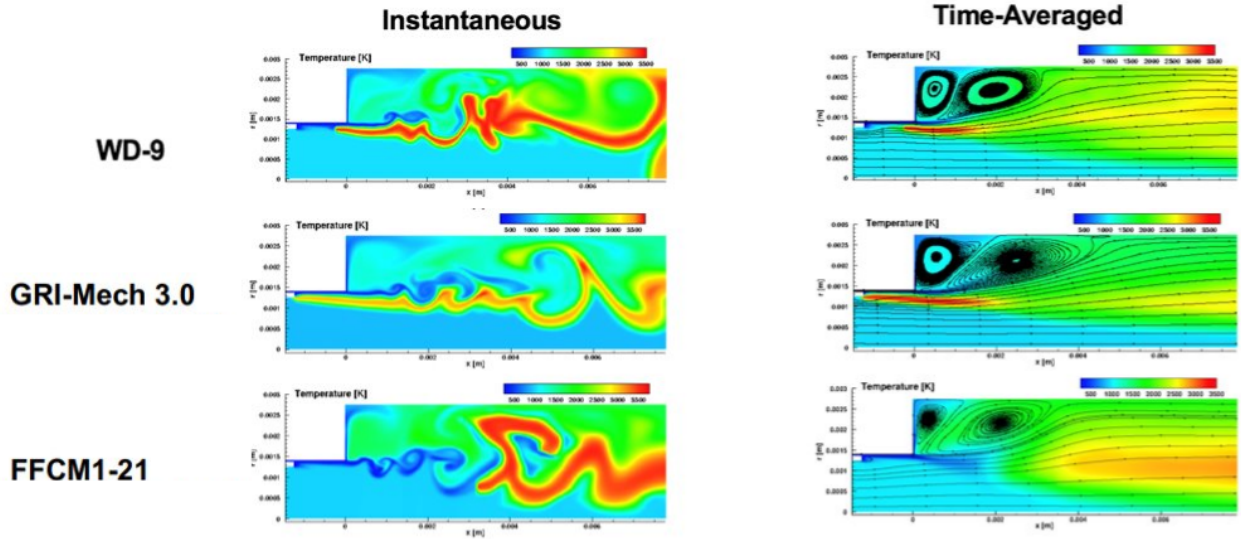
Figure 3.8: Instantaneous and time-averaged temperature field for all three chemical mechanisms at a high momentum flux ratio, MFR = 18.56, with baseline grid and temporal resolution.

Figure 3.9: Instantaneous temperature contours for shear-coaxial methane-oxygen injector using GRI-Mech (left) and FFCM1-21 (right) for fuel-oxidizer momentum flux ratio of 18.56. Top row is for the baseline grid as shown in Figure 3.8, bottom row has finer spatial and temporal grid resolution.

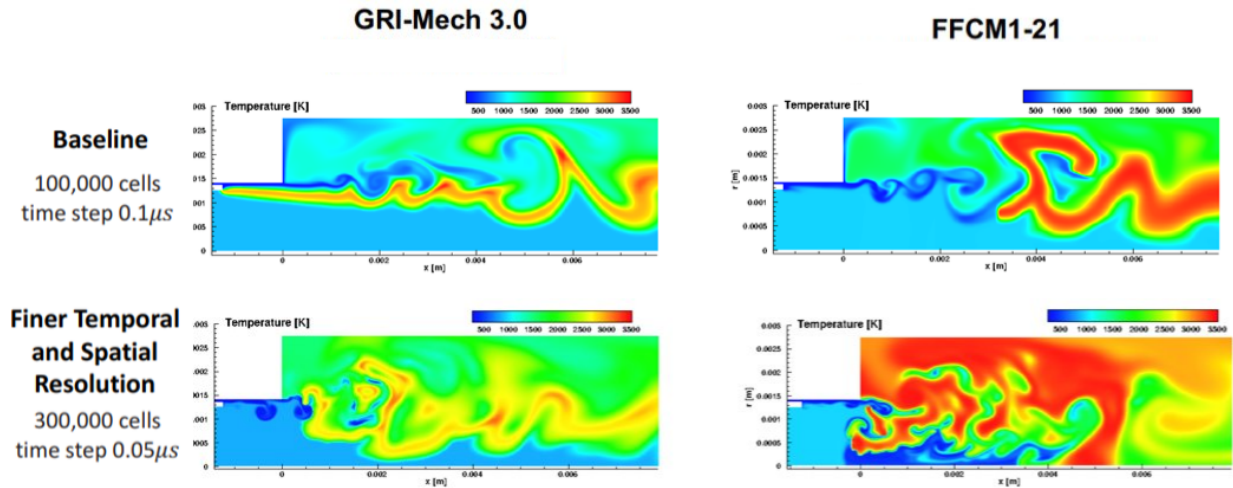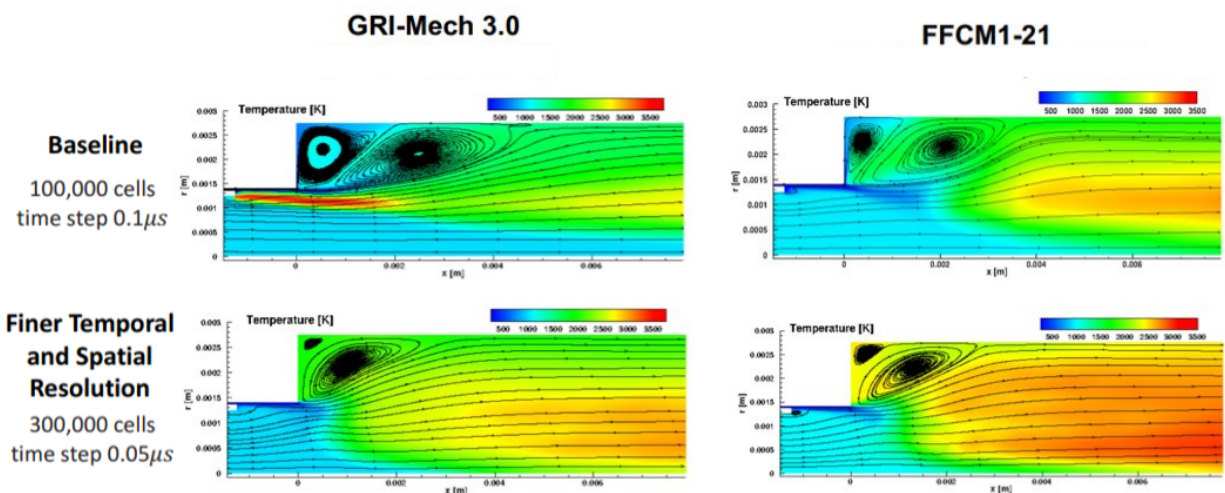Figure 3.10: Average temperature contours for shear-coaxial methane-oxygen injector using GRI-Mech (left) and FFCM1-21 (right) for fuel-oxidizer momentum flux ratio of 18.56. Top row is for the baseline grid as shown in Figure 3.8, bottom row has finer spatial and temporal grid resolution.

the flame begins to attach to the dump plane for the FFCM1-21 case. It appears that neither condition here is sufficiently resolved, and additional level of grid resolution is required to fully understand the effects of the different mechanisms on the turbulent reactive flowfield. Figure 3.10 shows the time-averaged temperature field results for the cases in Figure 3.4 and show good agreement. In addition, all cases show two small recirculation regions, which ineract with the shear layer and alter the flame dynamics.

.

3.5   Observations from 2D Simulations

Methane-oxygen combustion simulations of a shear coaxial injection configuration were performed using three alternative chemical kinetic mechanisms. The first was the modified global mechanism from Westbrook and Dryer (WD-9), the second one was the detailed GRI-Mech 3.0 mechanism, and the third was the skeletal FFCM1-21 mechanism. Results revealed that it is important to establish grid convergence before making comparisons of re-

action mechanisms. They also show that for low MFR, FFCM1-21 has greater time-step and spatial grid sensitivity. The absence of certain species in the skeletal chemical mechanism (FFCM1-21) may be responsible for the sensitivity. For high MFR, greater differences were observed at the same resolution. In addition, finer resolution is needed for kinetics models at high MFR to achieve convergence compared to low MFR case. Therefore, it would be useful to study the behavior of detailed, reduced and skeletal mechanisms in a systematic fashion. This will be carried out in the next part of the thesis. Specifically, it is useful to explore the application of the CEMA approach for the different mechanisms and their influence on the reactive process itself. The amount of data obtained in 2D can be very large. Thus, scaling back to a smaller, yet similar, problem , such as 0D and/or 1D combustion problems, can help users gain a clearer understanding. These simpler configurations are presented and explored in the subsequent chapters.

CHAPTER 4

CEMA Formulation and Validation

4.1   Introduction

Premixed combustion is found in many advanced combustion engines. An important parameter to predict or model in these flames is the burning velocity [19]. Assuming that the reactants upstream are chemically frozen, ignition occurs due to back-diffusion of energy and radicals from the reaction zone when the mixture crosses the preheat zone. Thus, in this case the laminar flame speed is considered a property of the pre-mixture. The flame propagation mode in this case is due to a deflagration wave that propagates at the flame speed, an eigenvalue of the flame. However, when the reactant mixture is pre-heated and auto-ignites at the inlet, the flame propagation may not be controlled by back-diffusion. Note, auto-ignition here is defined as taking place if the residence time of the mixture ahead of the flame front is longer than or comparable to the ignition delay time at the reactant mixture inlet. Thus, the flame speed is an important parameter in premixed flame simulations.

Several studies have been carried out to investigate the two different flame propagation modes in laminar [119] and turbulent [120] premixed flames. The transition of flame propagation from deflagration to auto-ignition for one-dimensional (1-D) steady state freely propagating flames of hydrogen/air were studied by Sankaran [121] by varying the computational domain size. Krisman et al. [122] investigated the flame location as a function of inflow velocity for fuels with and without the negative temperature coefficient (NTC) behavior.

As seen in the previous chapter, a more quantitative diagnostic tool is necessary to gain more insight into the important species and reactions for each mechansim. The chemical explosive mode (CEM) analysis (CEMA) [2], which was developed based on eigen-analysis

as a systematic diagnostic for critical flame features such as premixed flame fronts, auto-ignition, and local extinction, may be one viable option. CEMs have been found to be important for the ignition processes of combustion problems [123]. In the present chapter, a more detailed overview of the CEMA framework is presented. The CEMA formulation is then validated for a stoichiometric 1-D premixed flame for hydrogen-air. Next, CEMA is also applied to a similar methane-oxygen flame to study the reaction mechanisms relevant to rocket combustion of interest in the current work.

4.2 CSP and CEMA

Computational Singular Perturbation (CSP) analysis involves calculating the Jacobian for the chemical terms when solving chemical kinetics problems that are complex and stiff, and in most applications has included diffusion processes as well [58,124]. In the Chemical Explosive Mode Analysis (CEMA), only the chemical time scale is considered and thus, the diffusion time scale is omitted from the analysis [2]. In doing so, the implementation potentially becomes easier since the Jacobian can be easily calculated independently at each cell using the local primitive variables. Thus, CEMA formulation is simpler to implement compared with the computational singular perturbation (CSP) based methods [58, 124]. The already defined (CEMA) method was developed to qualitatively and quantitatively capture critical flame features, such as ignition, extinction, and premixed flame fronts. While CEMA has been used by certain groups more recently, the timescale analysis from CSP has influenced the development of CEMA. In the present study the CEMA approach for determining explosion indices is implemented, while the CSP-based participation index concept is also used in order to explore differences among the various mechanisms of interest.

CEMA is derived from the zero dimensional reacting equations, which are written as $\mathbf{f} = \frac{\partial \mathbf{Y}}{\partial t}$ where $\mathbf{Y} = \begin{pmatrix} Y_\ell & T \end{pmatrix}$. The source term vector is

$$\mathbf{f} = \begin{pmatrix} \frac{-1}{\rho c_p} \sum_{\ell=1}^{N} h_\ell \dot{\omega}_\ell & \frac{1}{\rho} \dot{\omega}_\ell \end{pmatrix}^\top \tag{4.1}$$

The species production term and progress variable are, respectively,

$$\dot{\omega}_\ell = W_\ell \sum_{k=1}^{K} \left(\nu_{\ell k}'' - \nu_{\ell k}' \right) w_k \tag{4.2}$$

The Jacobian used for CEMA $J = \frac{\partial \mathbf{f}}{\partial \mathbf{Y}}$. In the current CEMA implementation within the CFD solver [102], the Jacobian is computed analytically for accuracy.

A CEMA module is developed and the conservative Jacobian with the full LES solution vector $\left(\rho \quad \rho e \quad \rho Y_\ell \right)$ instead of $\left(T \quad Y_\ell \right)$ state vector is used. Thus, the Jacobian that is used in this study is $\Gamma^{-1}D$, where D is the Jacobian in terms of primitive variables and Γ^{-1} takes care of the transformation of variables from primitive to conservative. This Jacobian can also be written as

$$D_\omega = \frac{\partial \dot{\boldsymbol{\omega}}}{\partial \left(\rho \quad \rho e \quad \rho Y_\ell \right)} \tag{4.3}$$

D_ω has N+1 eigenvalues. M of these eigenvalues will be zero and correspond to conservative modes. These are associated with mass balance of the elements that participate in the reactions, such as C, H, O, N. In addition, two additional conservative modes exist with eigenvalues of zero. These are a result of the Jacobian entries corresponding to ρ and ρe. In reality, the values of the conservative modes near zero because of numerical rounding. Thus, a tolerance of 10^{-30} is used to classify the conservative modes as zero. After obtaining the eigenvalues of the Jacobian, M+2 eigenvalues are removed using a set threshold. Using the remaining eigenvalues, λ_{exp} is defined as $\lambda_{exp} = max\left(\Re\left(\lambda_i \right) \right)$ for $i = 1, ..., N + 1 - (M + 2)$ where $\Re$ is defined as the real part of the complex eigenvalue. λ_{exp} is largest eigenvalue of the Jacobian and is the dominant chemical time scale. When $\Re(\lambda_{exp}) > 0$, this mode is responsible for growth, and is considered explosive. When $\Re(\lambda_{exp}) < 0$ this mode is the slowest rate of decay and is non-explosive.

The transition of a mode from being explosive, i.e. $\Re(\lambda_{exp}) > 0$, to non-explosive, i.e. $\Re(\lambda_{exp}) < 0$, is indicative of critical flame features, such as ignition, extinction, and premixed flame front locations [2]. The presence of a positive chemical explosive mode (CEM) denotes

the tendency of a local mixture to auto-ignite, assuming it is adiabatic and in a constant volume.

4.3   Explosion Indices (EI) and Participation Indices (PI)

For a given CEM, there are corresponding left and right eigenvectors, $\mathbf{b_e}$ and $\mathbf{a_e}$. Using the left and right eigenvectors, we can define the explosive index [2] and participation index [125]. These are a weighted ranking of the importance that a species or reaction have on the explosive mode. The explosion index (EI), determines the species that contribute most to the trajectory of the explosive mode. This is based on the product of the left and right eigenvectors of the explosive mode. Note there is one EI for each species. The vector of EI can be defined as

$$EI = \frac{\text{diag}|\mathbf{a_e}\mathbf{b_e}|)}{\sum \text{diag}|\mathbf{a_e}\mathbf{b_e}|)} \tag{4.4}$$

and is a measure of how perpendicular the kth species is to the surface defined by the explosive mode. Larger values of this indicate a more significant impact to the explosive mode. Small values do not alter the trajectory of the explosive mode in state space and have negligible effect on the explosive mode.

The participation index (PI), determines which reactions are contributing most to the trajectory of the explosive mode. $\mathbf{S}$ is the matrix of stoichiometric coefficients, $\mathbf{w}$ is the net reaction rate vector. There is one PI for each reaction. The vector of PI can be defined as

$$PI = \frac{|\mathbf{b_e}\mathbf{S} \cdot \mathbf{w}|}{\sum |\mathbf{b_e}\mathbf{S} \cdot \mathbf{w}|} \tag{4.5}$$

One big challenge is that because different mechanisms will have a different numbers of species and reactions, the EI and PI can not be compared quantitatively between mechanisms because EI and PI represent a weighted contribution. However, for a particular mechanism, EI and PI are found to accurately determine relative importance of species and reactions that are responsible for the chemical explosive modes observed.
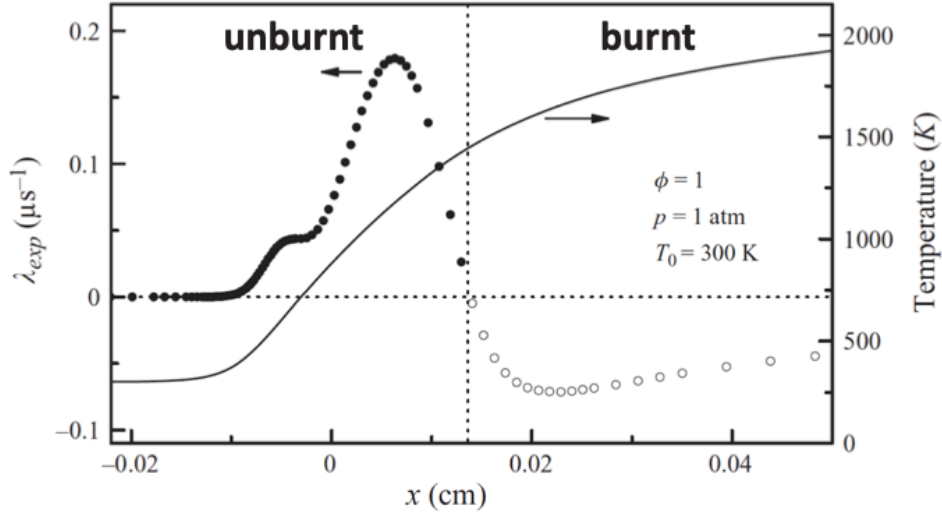
Figure 4.1: Structure of Temperature and Time Scales of the Chemical Explosive Modes in a 1D Freely Propagating H2-Air Premixed Flame [2]

4.4   1D Premixed Flame Validation

In the present study, the chemical explosive mode analysis (CEMA) module was developed. The CEMA module was first incorporated within GEMS and validated with published hydrogen-air 1D premixed flame results from [2].

The chemical explosive mode (inverse time scale) and temperature as a function of time in a one-dimensional freely propagating laminar premixed flame are shown in Figure 4.1 [2] and Figure 4.2 (GEMS). In both cases, the stoichiometric premixed hydrogen-air mixture is at a chamber pressure of 1 atm and initial temperature of 1000K. Note that there is both qualitative and quantitative agreement between the two cases. Chemical explosive modes (positive eigenvalues) are located in the unburnt region of the mixture (preheat zone). These chemical explosive modes increase, reaching both a local maximum and a global maximum, before decreasing and eventually transitioning to negative eigenvalues. Non-explosive modes (negative eigenvalues) are found in the burnt region of the mixture. Note that in Figure 4.1, all the eigenvalues are negative (open circles). This is because the appropriate number of modes of value zero were excluded to obtain these negative eigenvalues (M+2, eight modes
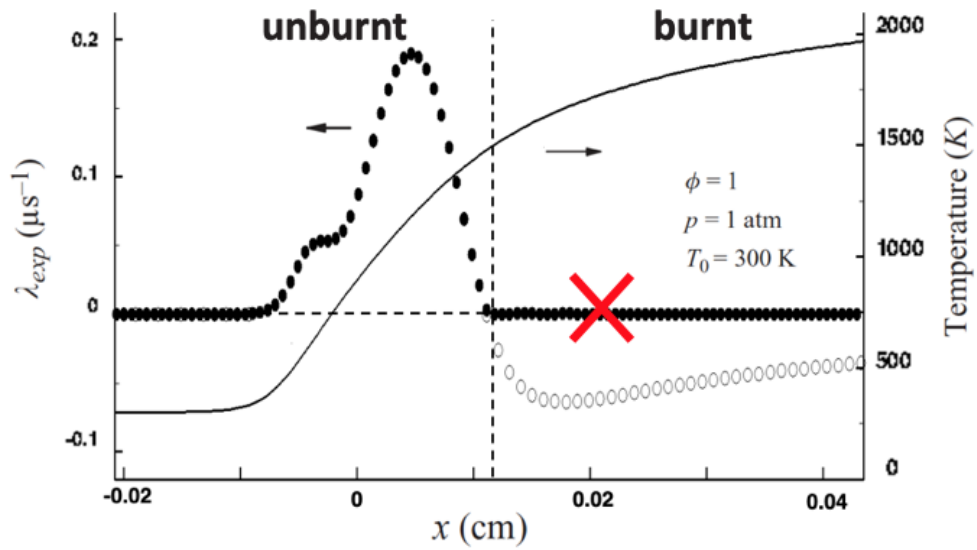
Figure 4.2: Structure of Temperature and Time Scales of the Chemical Explosive Modes in a 1D Freely Propagating H2-Air Premixed Flame (GEMS)
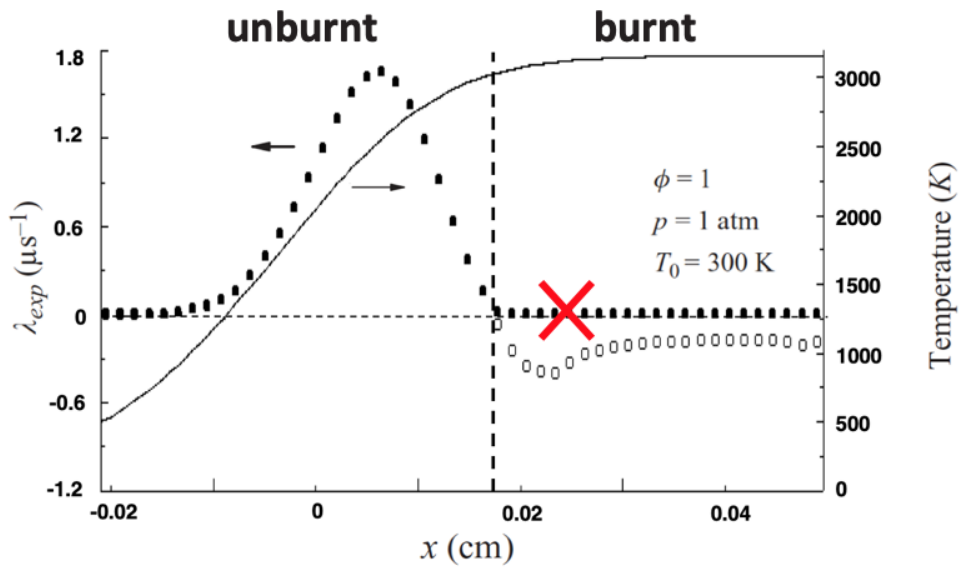

Figure 4.3: Structure of Temperature and Time Scales of the Chemical Explosive Modes in a 1D Freely Propagating CH4-O2 Premixed Flame (GEMS)

excluded). Figure 4.2 shows that if the appropriate number of modes are not excluded (seven or less modes excluded), then you obtain near zero eigenvalues and do not capture the negative eigenvalues appropriately. Thus, it is crucial to identify the number of zero eigenvalues to exclude, which is dependent on the problem type and chemical mechanism used. The mode exclusion procedure was described in Section 4.2. The transition from explosive to non-explosive modes occurs very sharply and in the vicinity of the thermal runaway. This zone is thinner than the reaction zone and clearly separates the burnt and unburnt mixtures, denoted by the vertical dotted black line. Thus, the sharp transition from positive to negative eigenvalues can be used to detect the flame front for premixed flames.

A similar 1D case was run for methane-oxygen combustion using the FFCM1-21 mechanism at the same initial conditions. The explosive and non-explosive modes are shown in Figure 4.3. In this case, a local maximum is not as in Figure 4.2. The eigenvalues magnitudes also differ and are much higher for the CH4-O2 mixture. However, there is still a similar qualitative behavior as in the H2-Air mixture for both the explosive and non-explosive modes. The premixed flame front location is clearly delineated. Just as it was observed in 4.2, failing to remove the appropriate number of conservative modes (M+2, five modes should be excluded) leads to erroneous modes and negative eigenvalues are not accurately captured.

Figure 4.4 show the explosion indices for temperature and some species for the H2-Air mixture mentioned previously. These explosion indices indicate the relative or weighted importance of temperature and species that contribute to each chemical explosive mode. In the preheat zone, the dominant explosion index is that for temperature. This is expected since temperature is known to significantly influence ignition. In addition, there is a notable contribution from the H radical since the H radical from the burnt mixture diffuses back into the preheat zone (which is larger than the local generation of H in the preheat zone), thus continuously feeding the flame. As will be shown, this is in contrast to auto-ignition, where radical explosion contributes significantly to the accumulation of radicals in the preheat region.

Thus, as shown and validated for this 1D problem, chemical Jacobian eigenvalues and EI and/or PI can give insight on the location of the explosive modes within the flowfield, the
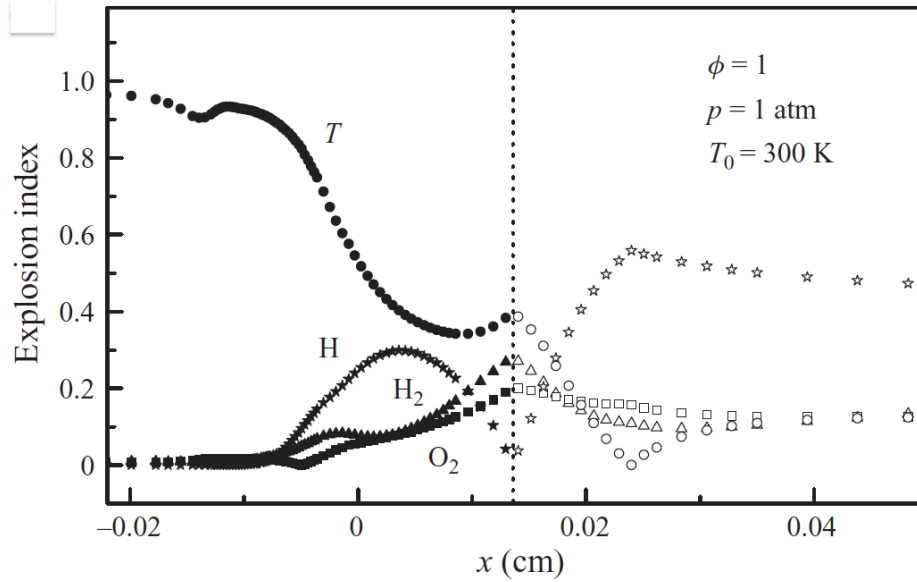
Figure 4.4: EI of the Chemical Explosive Modes in a 1D Freely Propagating H2-Air Premixed Flame [2]

point of ignition, and the species and/or reactions that are most important for ignition. As will be shown, this CEMA method will be applied to a 0D homogeneous ignition problem to gain insight into the important species and reactions in methane-oxygen combustion. Specifically, we use the analysis to distinguish which species and reactions are significant contributors to the CEMA modes and whether they change based on the inlet conditions into the flame-front. In turn, these results are relevant to the rocket injector problem described earlier.

CHAPTER 5

Sensitivity of Methane-Oxygen Combustion

There is great interest in understanding the effect of turbulence on kinetics. As mentioned previously, DNS simulations are costly, especially for large parameter studies involving detailed chemistry models. Chemical explosive mode analysis (CEMA) may provide an efficient tool to extract information from datasets and identify the important species and reactions. In particular, CEMA is similar to a sensitivity analysis but is less computationally expensive to implement since it does not involve species transport. It involves a local flux, which does not involve diffusive properties.

Thus, CEMA can be applied to 2D and 3D CFD data sets, one-dimensional turbulence (ODT), and/or particle Lagrangian time histories without significant effort. The current approach is to apply the CEMA framework to 0D combustion before considering a more complex turbulent data set, such as 2D or 3D CFD data sets. The objective is to verify that the conclusions from 0D reflect what is already known about laminar combustion. 0D simulations with the CEMA implementation may also help identify and determine what to examine in a large and more complex turbulent dataset.

It is thought that because of mixing, stretching, and other factors, the sensitivity for the large number of chemical pathways in turbulent flames may be lower than in laminar flames. This would mean that in these turbulent flowfields, reduced mechanisms may be applicable under certain types of flows, regimes, and conditions. Thus, it is important to eventually investigate complex turbulent flames with the CEMA approach.

Table 5.1: Kinetic mechanisms used in 0D study

	FFCM-1	FFCMY-12
No. Species	38	13
No. Reactions	291	38
No. Conserved Elements	6	3
No. Modes Excluded	8	5

Table 5.2: Initial conditions for all cases

Case	Pressure [atm]	Temperature [K]	ϕ	Species Mole Fractions
Baseline	10, 20, 30	1000	1.0	CH4: 0.33, O2: 0.67
O & H Radical Addition	10, 20, 30	1000	1.0	CH4: 0.332803, O2: 0.666626, H: 0.00293, O: 0.00278
O Radical Addition	10	1000	1.0	CH4: 0.32903, O2: 0.66818 O: 0.00279

5.1 Operating Conditions

The kinetic mechanisms used in this 0D study are the detailed FFCM-1 chemistry model and the reduced FFCMY-12 chemistry model for methane-oxygen combustion [30,31]. Table 5.1 shows details for each of the chemical mechanisms. The FFCM-1 mechanism contains 38 species and 291 reactions. The number of conserved elements, M, are six (H, O, C, N, AR, He). Note, when using the CEMA framework, according to the rules specified in Chapter 4, M+2 modes need to be excluded to capture the negative eigenvalues. Thus, a total of eight modes need to be excluded. In contrast, the FFCMY-12 chemical mechanism is much smaller, with 13 species and 38 reactions. It has been derived from FFCM-1 and optimized for high pressures (10 atm or above). This chemistry model has only three conserved elements (H, O, C) and thus, the total number of modes that need to be excluded in order to capture the negative eigenvalues are five.

A range of operating conditions has been studied for 0D homogeneous combustion using the different kinetic mechanisms mentioned previously. CHEMKIN was utilized to run 0D constant volume adiabatic combustion. Table 5.2 shows the initial conditions of the all the 0D cases in this study. The baseline case involves gaseous methane and oxygen mixture (its composition specified by the species mole fractions) at an initial pressure of 10 atm, an

Table 5.3: 0D Baseline Case: Ignition Delay, Peak Temperature, Peak CEM

	FFCM-1	FFCMY-12
Ignition Delay [ms]	26.58	18.40
Peak Temperature [K]	3831.23	3826.96
Peak CEM $[\frac{1}{\mu s}]$	84.3831	88.5067

Table 5.4: 0D O and H Radical Addition Case: Ignition Delay, Peak Temperature, Peak CEM

	FFCM-1	FFCMY-12
Ignition Delay [ms]	3.06	0.45
Peak Temperature [K]	3837.33	3833.01
Peak CEM $[\frac{1}{\mu s}]$	85.6762	89.5983

initial temperature of 1000 K, and a stoichiometric equivalence ratio. There are also radical addition cases in which O or O and H radicals are added to the initial CH4-O2 mixture under the same initial pressure, temperature, and equivalence ratio. O and H radicals were added to the initial mixture to mimic the condition that occurs when there is a backflow of O and H radicals to the preheat region that generally occurs under turbulent conditions. The baseline and O and H radical addition cases are also performed at elevated pressures of 20 atm and 30 atm.

Table 5.5: 0D O Radical Addition Case: Ignition Delay, Peak Temperature, Peak CEM

	FFCM-1	FFCMY-12
Ignition Delay [ms]	6.654	1.09
Peak Temperature [K]	3834.40	3830.10
Peak CEM $[\frac{1}{\mu s}]$	85.08	89.12

Table 5.6: 0D Baseline Case at Elevated Pressure (20 atm): Ignition Delay, Peak Temperature, Peak CEM

	FFCM-1	FFCMY-12
Ignition Delay [ms]	13.629	12.576
Peak Temperature [K]	3965.82	3961.11
Peak CEM $[\frac{1}{\mu s}]$	161.35	157.99

Table 5.7: 0D Baseline Case at Elevated Pressure (30 atm): Ignition Delay, Peak Temperature, Peak CEM

	FFCM-1	FFCMY-12
Ignition Delay [ms]	9.241	9.544
Peak Temperature [K]	4046.47	4041.53
Peak CEM $[\frac{1}{\mu s}]$	233.06	217.83

Table 5.8: 0D O and H Radical Addition Case at Elevated Pressure (20 atm): Ignition Delay, Peak Temperature, Peak CEM

	FFCM-1	FFCMY-12
Ignition Delay [ms]	1.390	0.292
Peak Temperature [K]	3972.60	3967.82
Peak CEM $[\frac{1}{\mu s}]$	163.94	160.11

Table 5.9: 0D O and H Radical Addition Case at Elevated Pressure (30 atm): Ignition Delay, Peak Temperature, Peak CEM

	FFCM-1	FFCMY-12
Ignition Delay [ms]	0.898	0.231
Peak Temperature [K]	4053.68	4048.66
Peak CEM $[\frac{1}{\mu s}]$	236.92	220.92

5.2 Results

It is useful to compare the ignition times, peak CEM, and peak temperatures predicted by the different chemical mechanisms to see how closely the reduced mechanism, FFCMY-12, agrees with the detailed mechanism, FFCM-1. In addition, it is also important to look at different initial conditions to see how the two mechanisms agree under varying conditions. Table 5.3 shows the resulting ignition delay, peak temperature, and peak CEM for the baseline cases for each chemical mechanism. Comparing the two chemical mechanisms, the ignition delay with the reduced FFCMY-12 mechanism is shorter by about 30% than with the detailed FFCM-1 mechanism, despite other parameters, such as laminar flame speeds, have been matched in its development. In addition, FFCMY-12 slightly underpredicts the peak temperature and overpredicts the CEM compared to the FFCM-1 chemistry model. This can also be seen in Figure 5.1, which shows the temperature and CEM distribution for the baseline case in the vicinity of the flame along with the ignition time in terms of shifted time (denoted by the vertical dotted black line along a shifted time of zero). Figure 5.1 also shows that prior to ignition, FFCMY-12 tends to overpredict the CEM and after ignition, the negative eigenvalues are underpredicted by FFCMY-12 (to a larger extent).

Mass fractions for some species in the baseline case are shown in Figure 5.2 and Figure 5.3 in the shifted time interval of -2×10^{-9} to 2×10^{-9}. The species profiles for O2 and CH4 using FFCMY-12 seem to agree fairly well with those for the detailed mechanism. For the CH4 profile, the largest discrepancies between the two mechanisms occur away from the the ignition point and at/near ignition. Specifically, FFCMY-12 underpredicts CH4 mass fraction prior to (but away) from ignition and overpredicts it at/near ignition. For the CO2 profile, FFCMY-12 begins to slightly overpredict as ignition is approached, and the discrepancy increases after ignition. For the CH3 profile, FFCMY-12 overpredicts the species mass fraction significantly before and slightly after ignition. The discrepancy between the two mechanisms decreases until a point after ignition, after which there is good agreement. There seems to be fair agreement between the two chemical mechanisms for both H and O radicals, with FFCMY-12 slightly overpredicting the value in both cases.
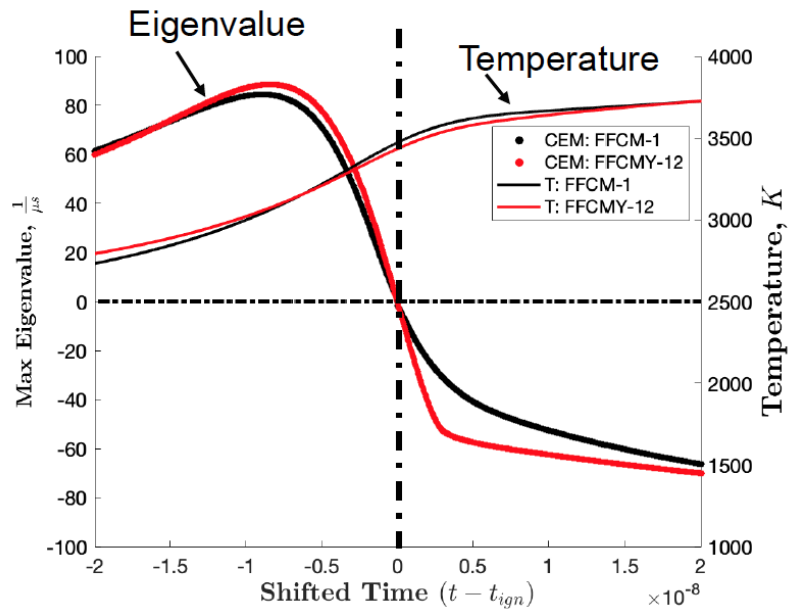
64

Figure 5.1: Explosive modes/non-explosive modes (left ordinate) and temperature (right ordinate) as a function of shifted time for FFCM-1 and FFCMY-12 (shifted by corresponding ignition time). Horizontal dashed line separates explosive modes (positive eigenvalues) and non-explosive modes (negative eigenvalues). Vertical dashed line denotes ignition point.

Table 5.4 shows that for the case where O and H radicals are added to the original mixture, the ignition delay with the FFCM-1 is significantly shorter (88.5% shorter) than in the baseline case. Similarly, the ignition delay with the FFCMY-12 is significantly shorter (98% shorter) than in the baseline case. Thus, the addition of these radicals seems to speed up ignition time in both chemical mechanisms (moreso in the reduced mechanism), which is expected when there is backflow of O and H radicals that speed up the combustion equation. In addition, with the FFCM-1 mechanism, the CEM increases by 1.5% as radicals O and H are added to the initial mixture while with the FFCMY-12 mechanism, the CEM increases by 1.2%. Comparing the two chemical mechanisms under the same conditions (O and H radical addition), the ignition delay with the reduced FFCMY-12 mechanism is shorter by about 85% than with the detailed FFCM-1 mechanism, which is a larger difference than in the baseline case. In addition, FFCMY-12 slightly underpredicts the peak temperature and overpredicts the CEM by 4.6% compared to the FFCM-1 chemistry model.

Table 5.5 shows that for the case where only the O radical is added to the original mixture, the ignition delay with the FFCM-1 is significantly larger (117% larger) than in the O and H radical addition case. Similarly, the ignition delay with the FFCMY-12 is significantly larger (142% shorter) than in the baseline case. Thus, the addition only the O radical seems to slow ignition compared to adding both O and H radicals, in which the combustion equation is significantly activated. In addition, with the FFCM-1 mechanism, the CEM decreases by 0.7% when compared to O and H radical addition while with the FFCMY-12 mechanism, the CEM decreases by 0.5%. Comparing the two chemical mechanisms under the same conditions (O radical addition), the ignition delay with the reduced FFCMY-12 mechanism is shorter by about 84% than with the detailed FFCM-1 mechanism, which is a slightly shorter difference than in the O and H radical addition case. In addition, FFCMY-12 slightly underpredicts the peak temperature and overpredicts the CEM by 4.7% compared to the FFCM-1 chemistry model.

These three cases show two main effects. The first is that for FFCM-1, the addition of radicals to the initial methane-oxygen mixture yields significant differences in the ignition time and slight differences in the peak temperature and peak CEM. Specifically, with the

addition of O and H radicals, the ignition time decreases and both the peak temperature and peak CEM increase. The second, and most important, is that given FFCM-1, FFCMY-12 consistently underpredicts the ignition time and overpredicts the peak CEM, especially for the radical addition cases, and thus may be missing important reactions found in the FFCM-1 detailed mechanism that suitable for turbulent conditions, where backflow and mixing of radicals into the intial mixture is common. Another thing to note is that chemical mechanism development typically involves calibration to laminar flame speed data, etc. Unfortunately, ignition times or reduced mechanisms are difficult to pin down for agreement. Thus, a difference in ignition time between FFCM-1 and FFCMY-12 (up to factor of 2) may be expected.

As mentioned previously, the baseline and O and H radical addition cases were performed at elevated pressures (20 and 30 atm) as well. This is shown in Tables 5.6 to 5.9. Looking at FFCM-1, for either the baseline case or the addition of radicals, as pressure increases, ignition time decreases, peak temperature increases, and peak CEM increases. Specifically, for the baseline case, as pressure is increased from 10 atm to 20 atm, the ignition time decreases by almost 50% and the peak CEM increases by about 90%. Going from 20 atm to 30 atm, the ignition time further decreases by 32% and the peak CEM increases by 44%. Thus, as pressure increases, it has less of an effect on the ignition time and peak CEM. For the O and H radical addition case, a similar trend can be seen. Increasing the pressure from 10 atm to 20 atm, the ignition time decreases by almost 55% and the peak CEM increases by about 90%. Going from 20 atm to 30 atm, the ignition time further decreases by 35% and the peak CEM increases by 44%.

Comparing the two chemical mechanisms under the same conditions (baseline or O and H radical addition), there seems to be a greater discrepancy for ignition delay times between the two mechanisms at lower pressures. As the pressure is increased, the ignition delay times have better agreement for the two mechanisms. Specifically, for the baseline case at 20 atm, the FFCMY-12 mechanism underpredicts the ignition delay time that FFCM-1 yields by 7.7% compared to the baseline case at 10 atm, which results in a discrepancy of about 30%. In addition, the FFCMY-12 mechanism underpredicts the peak CEM by 2%, compared to

the baseline case at 10 atm, which results in a discrepancy of about 5%. For the baseline case at 30 atm, the FFCMY-12 mechanism overpredicts the ignition delay time that FFCM-1 yields by 3.2%. Also, the FFCMY-12 mechanism underpredicts the peak CEM by 6.5%. For the O and H radical addition case at 20 atm, the FFCMY-12 mechanism underpredicts the ignition delay time that FFCM-1 yields by 80% compared to the O and H radical addition case at 10 atm, which results in a discrepancy of about 88.5%. In addition, the FFCMY-12 mechanism underpredicts the peak CEM by about 2%, compared to the O and H radical addition case at 10 atm, which results in a discrepancy of about 4.6%. Similarly, at 30 atm, the FFCMY-12 mechanism underpredicts the ignition delay time that FFCM-1 yields by 74%. Also, the FFCMY-12 mechanism underpredicts the peak CEM by about 6.7%.

The Explosion Indices and Participation Indices for each of the cases were also calculated to gain insight into the important species and reactions. Figures 5.4 - 5.8 show the dominant Explosion Indices for the baseline case using the FFCM-1 and FFCMY mechanisms within the shifted time window of -2×10^{-9} to 2×10^{-9}. The vertical line represents the ignition time (represented as a shifted time of zero). It is evident that for both mechanisms, the explosion index for O2 dominates around ignition. There is some contribution from CO2 sometime after ignition when using the FFCMY-12 mechanism. Looking at the second, third, and fourth largest explosion indices gives a greater insight into other fairly significant contributions to the CEM. The plot for the second largest EI shows that EI for OH and ρ dominate prior to ignition for both mechanisms. With the FFCMY-12 mechanism, the EI for OH dominates at and immediately after ignition, after which EI for ρ quickly takes over again. EI for CO then dominates. In contrast, with FFCMY-12, EI for ρ dominates across ignition continuously. Afterwards, EI for CO2, O2, and ρe dominate. The third, fourth, etc largest EI can be constructed to show similar plots of the most dominant EI to the CEM.

Figures 5.9 to 5.2 show the dominant Participation Indices for the baseline case using the FFCM-1 and FFCMY mechanisms within the shifted time window of -2×10^{-9} to 2×10^{-9}. The vertical line represents the ignition time (represented as a shifted time of zero). The reactions are labeled according to how they are ordered in the FFCM-1 chemical mechanism. It can be seen that R1: $H + O_2 \longleftrightarrow O + OH$ is the most dominant reaction around ignition

for both chemical mechanisms. This is consistent with what is found in the literature, since the R1 chain branching reaction is often considered one of the most important elementary reactions in combustion chemistry. To look at other important reactions that contribute to the CEM, it is important to look at the second, third, fourth, etc largest PI. Looking at the second largest PI in Figure 5.10, it can be seen that with FFCM-1, R4 dominates across ignition. In contrast, with FFCMY-12, R98 dominates prior and across ignition. R4 then takes over shortly after ignition, and then R32 takes over. Thus, the major difference between the two mechanisms is the dominance of R98 with the FFCMY-12 mechanism, which will be explained shortly.

The EI and PI contributing most to the CEM for all the cases were tabulated. The species or reactions present in FFCM-1 but not present in FFCMY-12 are shown in red. The species or reactions considered important in the corresponding chemistry model but not the other are shown in blue. Table 5.10 shows the most important EI and PI for the baseline case. As the table shows, the most important species in common for both mechanisms are OH, O, O2, CO, CO2, CH3, and CH4. For FFCM-1, H, H2, C2H2 are also dominant EI. For FFCMY-12, H, H2, and C2H2 are not found as dominant species for the baseline case. The table also shows the most important reactions for each mechanism. Comparing important PI for both chemistry models at baseline conditions, most of the same reactions are generally considered important for both. Specifically, the mechanisms seem to share reactions R1, R3, R4, and R32. R98 is found to be important in the FFCMY-12 mechanism but not in FFCM-1, and R35 and R87 are found to be important in the FFCM-1 but do not exist in FFCMY-12.

The EI and PI contributing most to the CEM for the two mechanisms in the O and H radical addition case are summarized in Table 5.10. These seem to be the same as for the baseline case. As the table shows, the most important species in common for both mechanisms are OH, O, O2, CO, CO2. For FFCM-1, C2H2 is also dominant EI. For FFCMY-12, H, CH3 are also dominant species for the O and H radical addition case. The table also shows the most important reactions for each mechanism. Comparing important PI for both chemistry models at baseline conditions, most of the same reactions are generally considered

69

important for both. Specifically, the mechanisms seem to share reactions R1, R3, R4, and R32. R98 is found to be important in the FFCMY-12 mechanism but not in FFCM-1, and R35 and R87 are found to be important in the FFCM-1 but do not exist in FFCMY-12.

The EI and PI contributing most to the CEM for the two mechanisms in the O radical addition case are summarized in Table 5.10. Again, these ar the same as for the previous two cases. As the table shows, the most important species in common for both mechanisms are OH, O, O2, CO, CO2. For FFCM-1, C2H2 is also dominant EI. For FFCMY-12, H, CH3 are also dominant species for the O and H radical addition case. The table also shows the most important reactions for each mechanism. Comparing important PI for both chemistry models at baseline conditions, most of the same reactions are generally considered important for both. Specifically, the mechanisms seem to share reactions R1, R3, R4, and R32. R98 is found to be important in the FFCMY-12 mechanism but not in FFCM-1, and R35 and R87 are found to be important in the FFCM-1 but do not exist in FFCMY-12.

Thus in all three cases, the same reactions seem to be important for a particular chemical mechanism, indicating that although the addition of radicals to the initial mixture may shorten the ignition delay and increase the peak CEM, it has no impact on the reactions that are considered important to the CEM. For all three cases, a few reactions seem to be considered important in both mechanisms, such as R1, R3, R4, and R32. It is expected that R1, a chain-branching reaction, is important across all cases since it is one of the most important elementary reactions in combustion chemistry and aides in the production of OH radicals that are crucial to combustion chemistry. In all cases, FFCMY-12 has an important reaction, R98, which was not found to be important in the detailed mechanism. This is because in the development of FFCMY-12, C2 chemistry that was originally found in FFCM-1 was removed. Thus, no CH2 recombination is present in FFCMY-12. This yields a significant difference in CH3 mass fraction between FFCM-1 and FFCMY-12, which was observed previously in Figure 5.2a. R98 was purposefully slowed by modifying its reaction rate (becomes very limiting) in order to compensate for the C2 chemistry removal [30],smith2017ffcm. Thus, this explains why R98 is found to be an important reaction in FFCMY-12 but not in FFCM-1.

The ignition times in reduced mechanisms are inherently difficult to pin down for agreement during their development and validation. However, after comparing the reduced FFCMY-12 mechanisms with the detailed FFCM-1 mechanism, it was found that there was poor prediction of the ignition delay by FFCMY-12 in the presence of radicals. One reason for this may be that although for FFCMY-12, the same species and reactions seem to be important for the baseline and O and H radical addition cases, the magnitudes of the EI and PI are different. Thus, their contributions to the CEMS are not always exactly the same. The presence of radicals in the mixture may have more of an effect on the relative contributions of the EI and PI values in the smaller FFCMY-12 mechanism compared to in the larger FFCM-1 mechanism, thereby affecting the accuracy of the FFCMY-12 ignition delay.

Comparing the important EI and PI as a function of pressure, it can be seen that at the lowest pressure of 10 atm, H seems to be an important radical in the reduced FFCMY-12 mechanism that is not considered important in the detailed FFCM-1 mechanism. However, as pressure is increased to 20 and 30 atm, the H atom is considered important by the detailed mechanism but not captured by the reduced mechanism. For all pressure cases, C2H2 is considered important by the detailed mechanism, an important precursor to soot, but is not captured by the FFCMY-12 mechanism. FFCMY-12 shows CH3 as important for all pressures. It is interesting that as pressure is increased, the number of reactions that are considered important in the detailed mechanism increases. As pressure is increased to 20 atm, R270 is also considered important, which makes sense since OH* is a very important radical for ignition. As pressure is increased to 30 atm, R136, which involves CH3 and CH4, also becomes important.
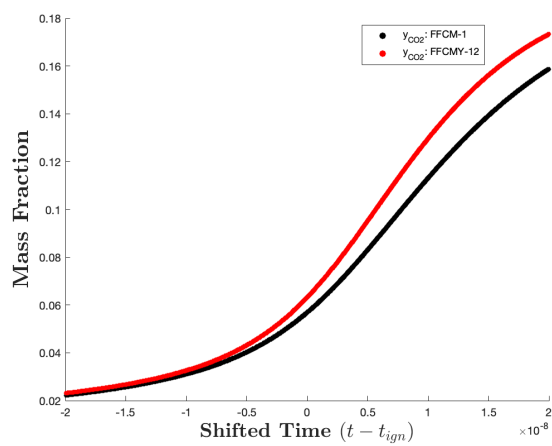
5.3   Observations from 0D Simulations

Chemical explosive mode analysis (CEMA) may serve as an efficient sensitivity analysis tool to identify the important species and reactions in a given flowfield since it is less computationally expensive than traditional means, especially for large simulations such as DNS and
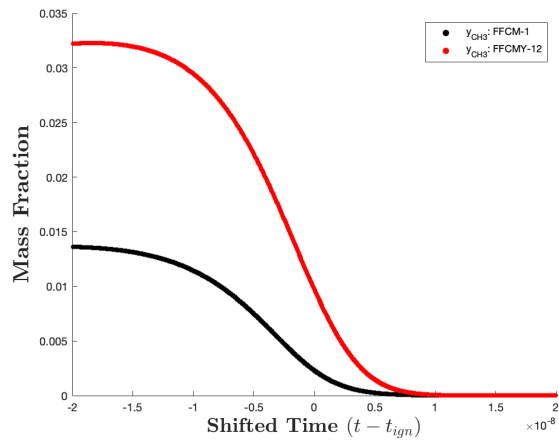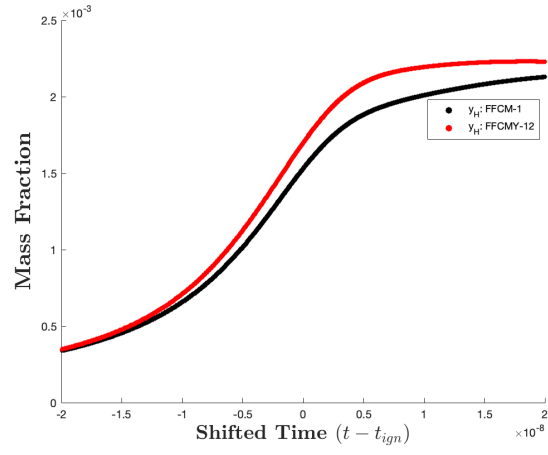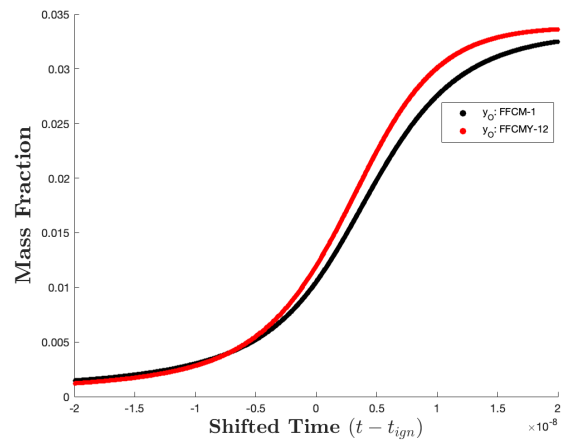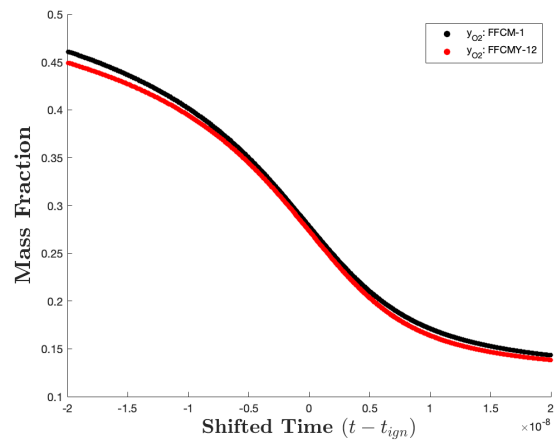
(a) Y_{CH3}
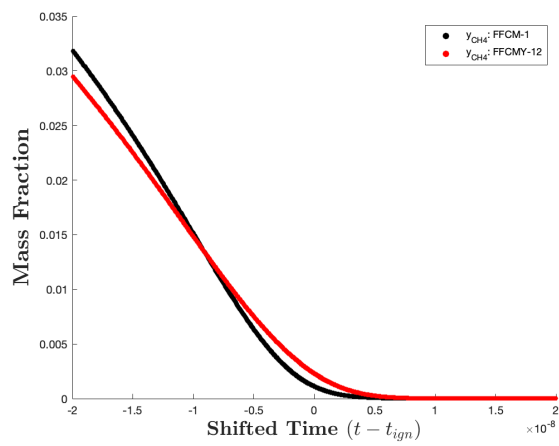
(b) Y_{CH4}

(c) Y_{CO2}

Figure 5.2: Species mass fractions for baseline case: CH3, CH4, CO2
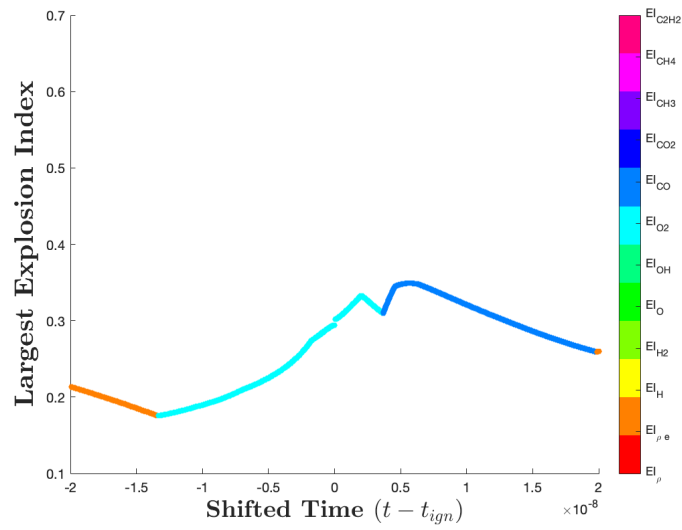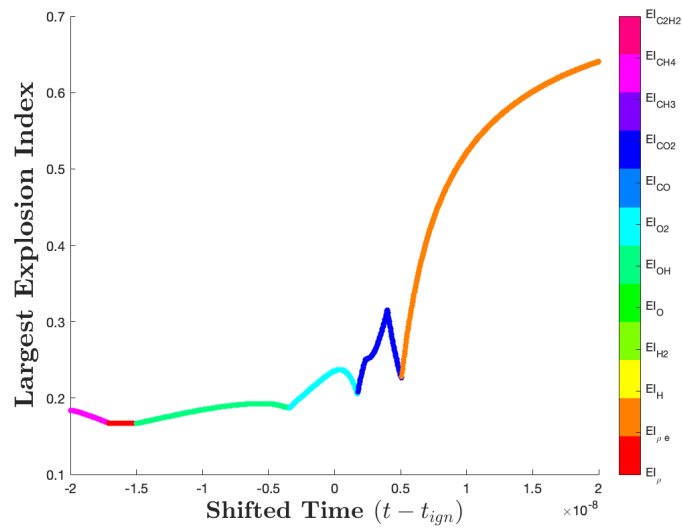
(a) Y_H

(b) Y_O

(c) Y_{O2}

Figure 5.3: Species mass fractions for baseline case: H, O, O2
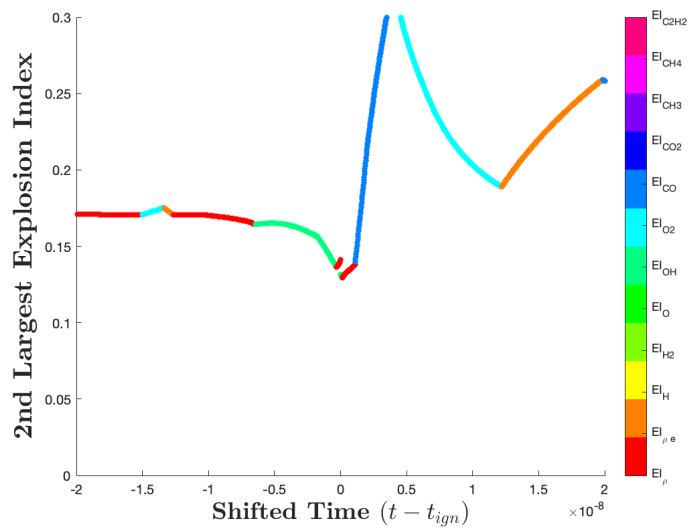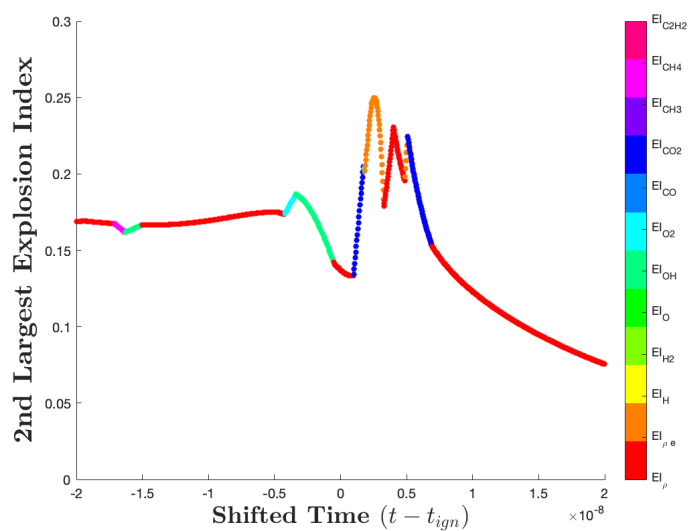
73

(a) FFCM-1

(b) FFCMY-12

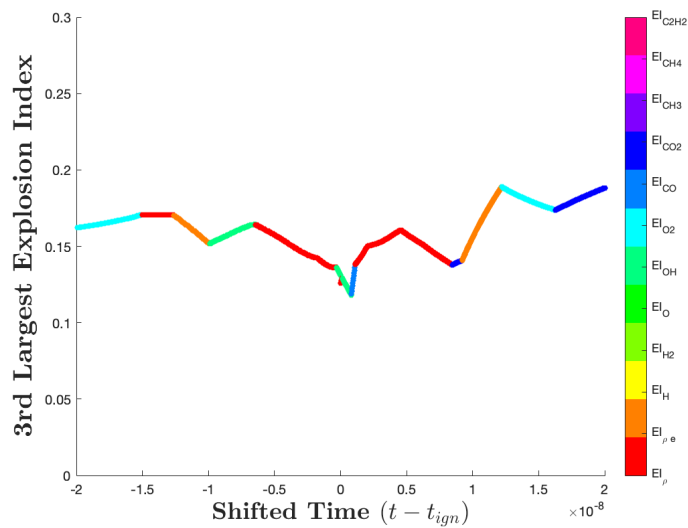Figure 5.4: Maximum EI for baseline case using FFCM-1 and FFCMY-12
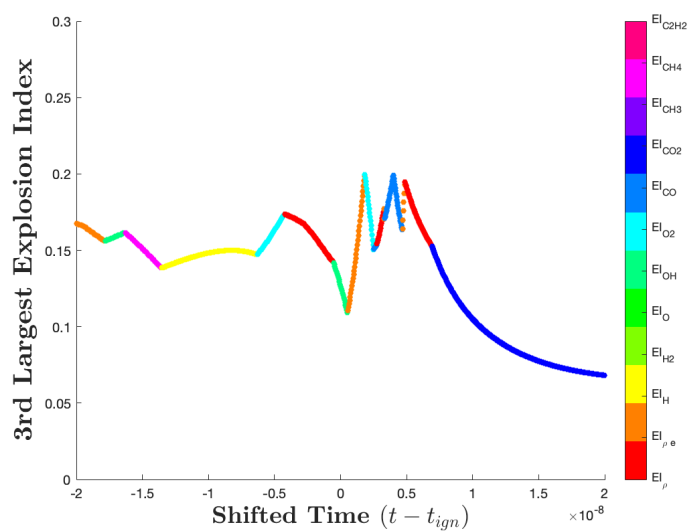
(a) FFCM-1

(b) FFCMY-12

Figure 5.5: 2nd Maximum EI for baseline case using FFCM-1 and FFCMY-12
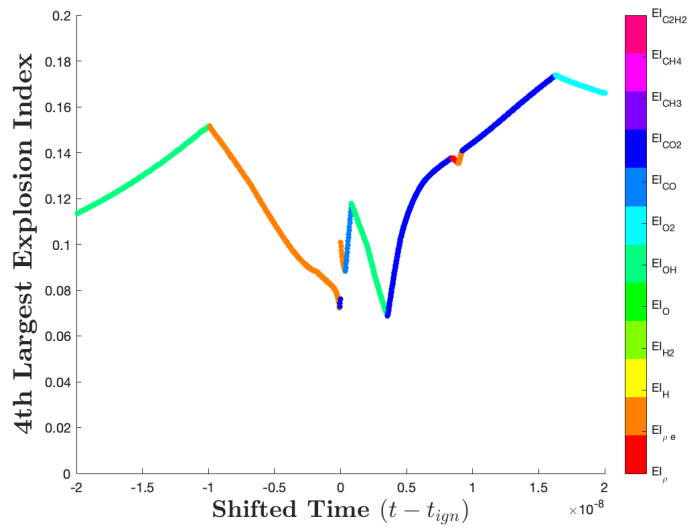
(a) FFCM-1

(b) FFCMY-12

Figure 5.6: 3rd Maximum EI for baseline case using FFCM-1 and FFCMY-12

(a) FFCM-1

(b) FFCMY-12

Figure 5.7: 4th Maximum EI for baseline case using FFCM-1 and FFCMY-12

(a) FFCM-1

(b) FFCMY-12

Figure 5.8: 5th Maximum EI for baseline case using FFCM-1 and FFCMY-12

(a) FFCM-1

(b) FFCMY-12

Figure 5.9: Maximum PI for baseline case using FFCM-1 and FFCMY-12

(a) FFCM-1

(b) FFCMY-12

Figure 5.10: 2nd Maximum PI for baseline case using FFCM-1 and FFCMY-12
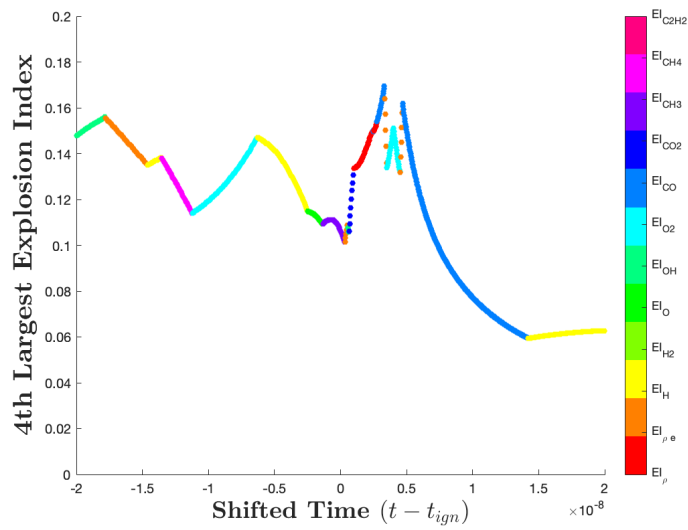
80

(a) FFCM-1

(b) FFCMY-12

Figure 5.11: 3rd Maximum PI for baseline case using FFCM-1 and FFCMY-12

81
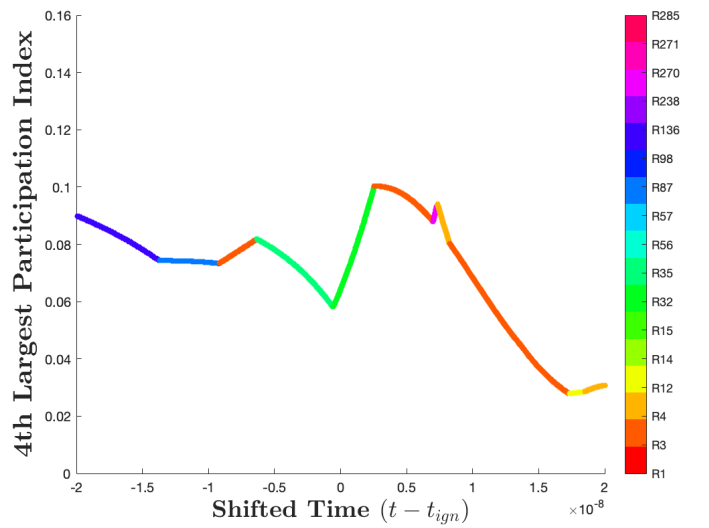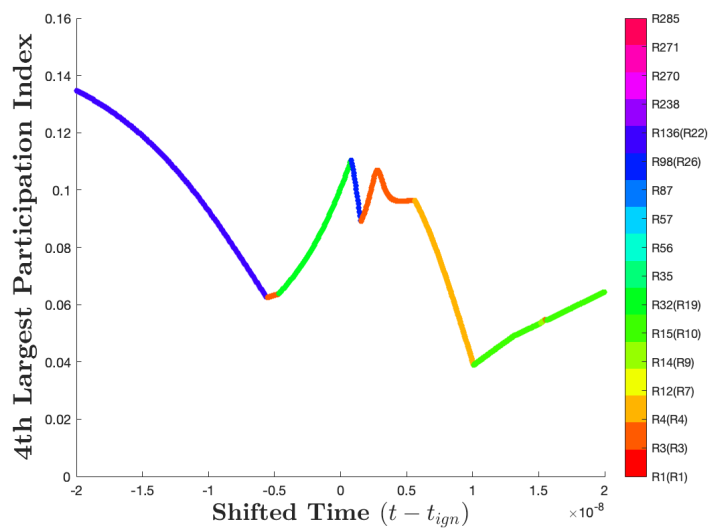
(a) FFCM-1

(b) FFCMY-12

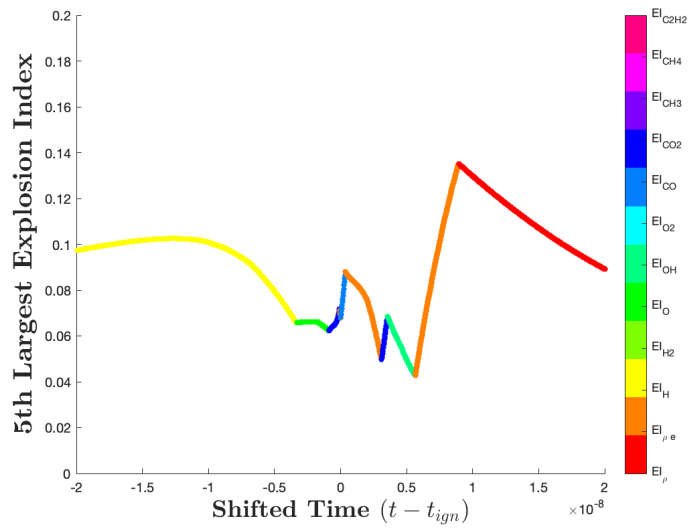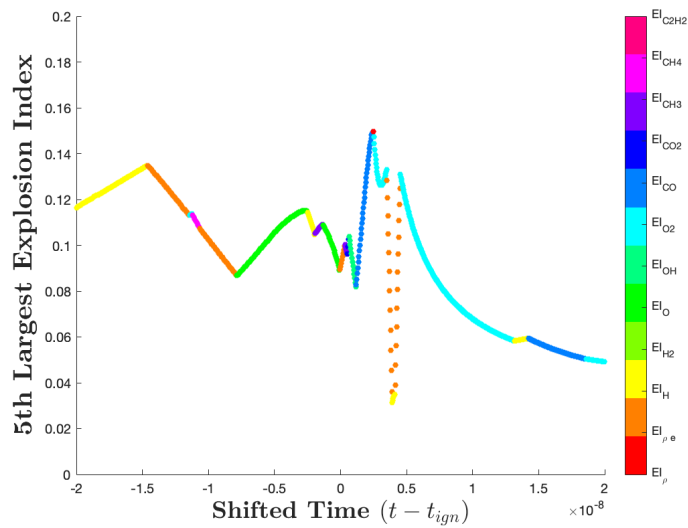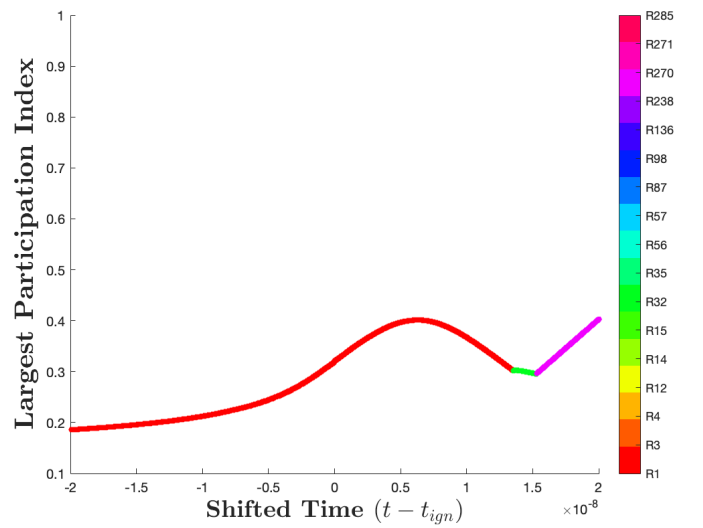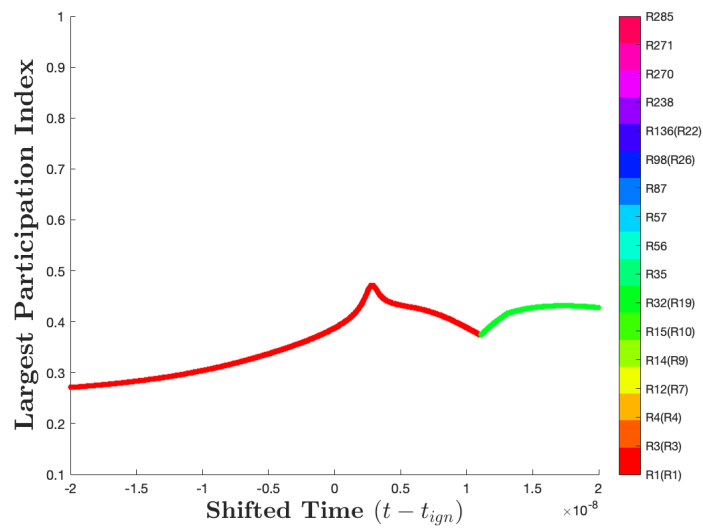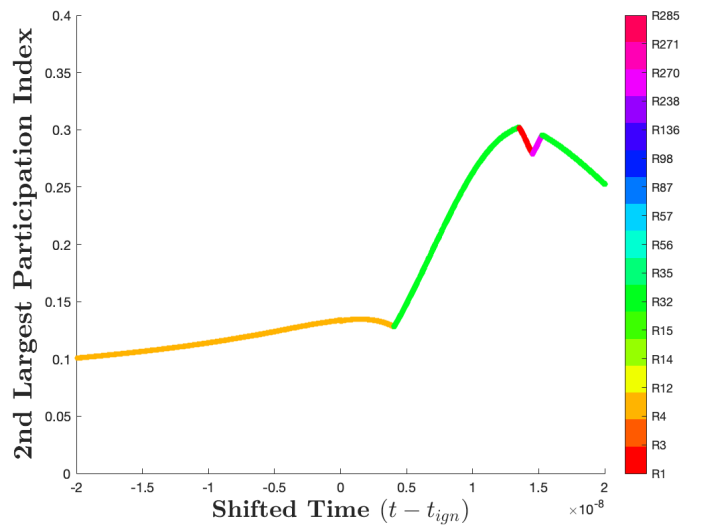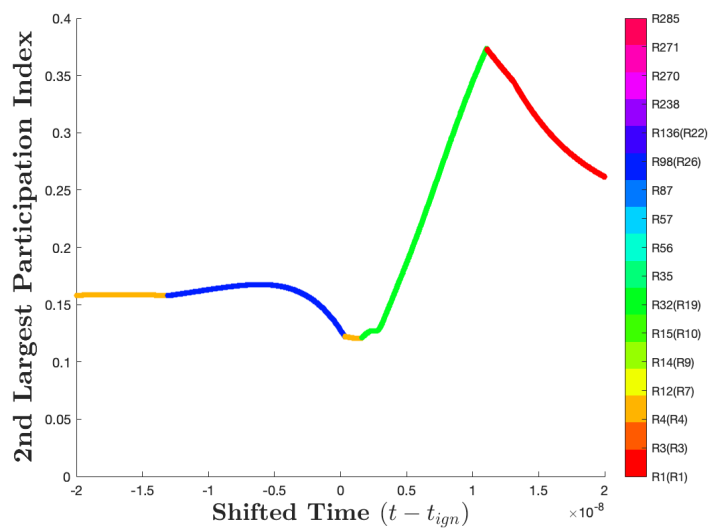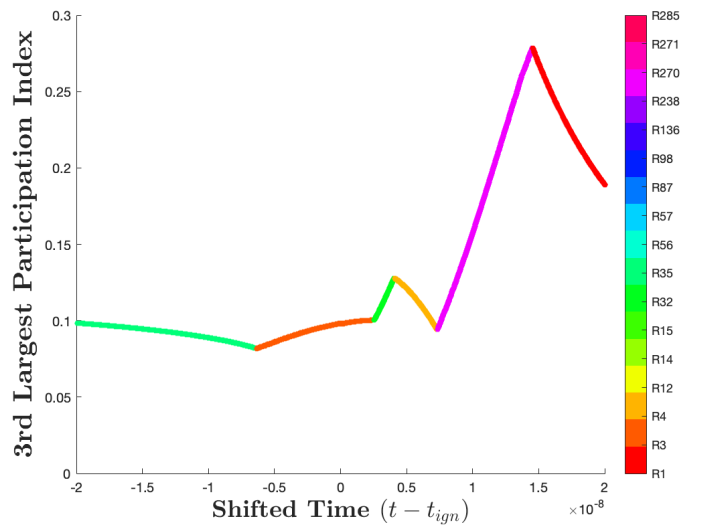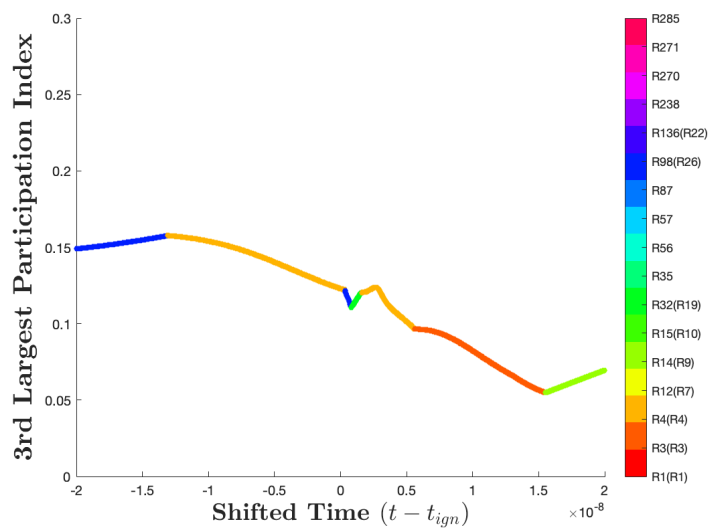Figure 5.12: 4th Maximum PI for baseline case using FFCM-1 and FFCMY-12

Table 5.10: Baseline, O and H Radical Addition, and O Radical Addition Cases (10 atm): Important EI and PI

Most Important EI and PI	FFCM-1	FFCMY-12
Species	OH, O, O2, CO, CO2, C2H2	H, OH, O, O2, CO, CO2, CH3
Reactions	R1: $H + O_2 \longleftrightarrow O + OH$	R1: $H + O_2 \longleftrightarrow O + OH$
	R3: $O + H_2 \longleftrightarrow H + OH$	R3: $O + H_2 \longleftrightarrow H + OH$
	R4: $OH + H_2 \longleftrightarrow H + H_2O$	R4: $OH + H_2 \longleftrightarrow H + H_2O$
	R32: $CO + OH \longleftrightarrow H + CO_2$	R32: $CO + OH \longleftrightarrow H + CO_2$
	R35: $HCO + M \longleftrightarrow H + CO + M$	R98: $CH_3 + O \longleftrightarrow H + CH_2O$
	R87: $CH_2O + H \longleftrightarrow HCO + H_2$	

Table 5.11: Baseline, O and H Radical Addition Cases (20 atm): Important EI and PI

Most Important EI and PI	FFCM-1	FFCMY-12
Species	H, OH, O, O2, CO, CO2, C2H2	OH, O, O2, CO, CO2, CH3
Reactions	R1: $H + O_2 \longleftrightarrow O + OH$	R1: $H + O_2 \longleftrightarrow O + OH$
	R3: $O + H_2 \longleftrightarrow H + OH$	R3: $O + H_2 \longleftrightarrow H + OH$
	R4: $OH + H_2 \longleftrightarrow H + H_2O$	R4: $OH + H_2 \longleftrightarrow H + H_2O$
	R32: $CO + OH \longleftrightarrow H + CO_2$	R32: $CO + OH \longleftrightarrow H + CO_2$
	R35: $HCO + M \longleftrightarrow H + CO + M$	R98: $CH_3 + O \longleftrightarrow H + CH_2O$
	R87: $CH_2O + H \longleftrightarrow HCO + H_2$	
	R270: $H + O + M \longleftrightarrow OH \cdot + M$	

Table 5.12: Baseline, O and H Radical Addition Cases (30 atm): Important EI and PI

Most Important EI and PI	FFCM-1	FFCMY-12
Species	H, OH, O, O2, CO, CO2, C2H2	OH, O, O2, CO, CO2, CH3
Reactions	R1: $H + O_2 \longleftrightarrow O + OH$	R1: $H + O_2 \longleftrightarrow O + OH$
	R3: $O + H_2 \longleftrightarrow H + OH$	R3: $O + H_2 \longleftrightarrow H + OH$
	R4: $OH + H_2 \longleftrightarrow H + H_2O$	R4: $OH + H_2 \longleftrightarrow H + H_2O$
	R14: $2\,H_2O \longleftrightarrow H + OH{+}H_2O$	R32: $CO + OH \longleftrightarrow H + CO_2$
	R32: $CO + OH \longleftrightarrow H + CO_2$	R98: $CH_3 + O \longleftrightarrow H + CH_2O$
	R35: $HCO + M \longleftrightarrow H + CO + M$	
	R87: $CH_2O + H \longleftrightarrow HCO + H_2$	
	R136: $CH_4 + H \longleftrightarrow CH_3 + H_2$	
	R270: $H + O + M \longleftrightarrow OH\cdot + M$	

3D LES. The CEMA framework was applied to 0D combustion to determine its viability in a more complex turbulent data set, such as 2D or 3D CFD data sets. A gaseous methane-oxygen mixture was run as well as mixtures with the addition of H and/or O radicals to simulate the effects of turbulent mixing of burnt gases with reactants. The O and H radical addition is an extreme case of the initial conditions and was used to mimic the thermochemical state in turbulent flames, such as the exhaust gas recirculation (EGR) condition, where there is recirculation of radicals from the burnt mixture into the unburnt mixture. This is important because current validation tests when reducing mechanisms are not inclusive of all thermochemical states in turbulent flames. The ignition times in reduced mechanisms are inherently difficult to pin down for agreement during their development and validation. However, it was found that there was poor prediction of the ignition delay by FFCMY-12 in the presence of radicals. One reason for this may be that although for FFCMY-12, the same species and reactions seem to be important for the baseline and O and H radical addition cases, the magnitudes of the EI and PI are different. Thus, their contributions to the CEMs are not always exactly the same. The presence of radicals in the mixture may have more of an effect on the relative contributions of the EI and PI values in the smaller FFCMY-12 mechanism compared to in the larger FFCM-1 mechanism, thereby affecting the accuracy of

the FFCMY-12 ignition delay. Thus, a 0D CEMA analysis could help in the development of reduced mechanisms that are validated under EGR conditions by pinpointing the pertinent species and reactions under such conditions. Trends seen in 0D results helped to identify the important species and reactions necessary for a reduced mechanism to replicate important phenomena such as ignition. Because of this, there is confidence that 0D simulations with the CEMA implementation could also help identify and determine what to examine in a large and more complex turbulent dataset. CEMA could also be used in conjunction with Adaptive Chemistry Reduction in order to figure out what can be truncated in a particular thermochemical state as the simulation runs. This would significantly lower numerical cost of the CFD solution, especially for cases in which large chemical mechanisms are used. Note that methodology for reduction is valid for lower Karlovitz numbers but not high Ka (where more EGR and ignition/extinction modes exist). Thus, cases run may be within a low Ka range. CEMA may be useful to tell which region one is in. One of the biggest challenges with reduced mechanisms is the education needed to inform users on reduced mechanisms and related details, which may be beneficial so that reduced mechanisms are applied properly. One issue that is often encountered, for example, is that applying chemistry models to turbulent simulations is highly sensitive to grid resolution.

The one-dimensional turbulence (ODT) model represents an efficient and novel multiscale approach to couple reaction, diffusion and turbulent transport. It solves the unfiltered governing equations in one spatial dimension with a stochastic model for turbulent transport [126]. The model may be implemented as stand-alone for simple turbulent flows to get detailed information on the physics or may be used as a subgrid scale model in LES [127] to provide closure for reacting scalars in combustion in one dimension. Thus, one possible next step may include performing a repeat analysis using ODT particle history with CEMA at varying Ka in order to see if there is a difference in the important reactions for the CEM and to determine resolution requirements for FFCM-1 and FFCMY-12.

CHAPTER 6

Conclusions

The objective of this dissertation is to gain insights into the influence of alternative chemical kinetics mechanisms on the results of turbulent combustion simulations and, specifically, the effects of these mechanisms under conditions representative of rocket injector applications. The CEMA method was then applied to simpler 0D and 1D cases that are relevant to the more complex 2D combustion problem. A summary of the key conclusions and findings in each chapter is listed in the following.

In Chapter 3, simulations of methane-oxygen combustion and a shear coaxial injection configuration were performed. This configuration was used to study turbulent combustion and investigate the effects of kinetics on phenomena such as flame holding. Results demonstrated that in several cases, the kinetic mechanism can influence instantaneous and time-averaged flame characteristics, such as temperature. In addition, it was observed that at higher MFR conditions, spatial resolution had a significant effect on both GRI-Mech and FFCM1-21 chemical mechanisms at higher MFR conditions. In contrast, at low MFR, finer spatial and temporal resolution has an effect on the temperature field for FFCM-based computations. Thus, chemical mechanisms may have different resolution requirements to achieve similar flowfields. It may not always be clear which is the true solution among the different mechanisms. A more quantitative diagnostic tool, such as CEMA, is needed to help explain differences in simulation results with different mechanisms and to inform chemistry model development.

In Chapter 4, the CEMA framework was described in more detail. Instead of looking at a 2D problem, which can include a large amount of data, 1D premixed flames were studied. Results were validated with Lu et al. and showed good agreement for the temperature, CEM,

and species EI. With regard to the EI, results confirmed the notable contribution of the H radical due to radical backflow from the burnt mixture. Thus, as shown and validated for this 1D problem, chemical Jacobian eigenvalues and EI and/or PI can give insight on the location of the explosive modes within the flowfield, the point of ignition, and the species and/or reactions that are most important for ignition.

In Chapter 5, the CEMA framework was applied to 0D homogeneous combustion for various methane-oxygen mixtures using a detailed and reduced chemical mechanism to determine in viability in a more complex turbulent data set, such as 2D or 3D CFD data sets. It was found that there was poor prediction of the ignition delay by FFCMY-12 in the presence of radicals. One reason for this may be that although for FFCMY-12, the same species and reactions seem to be important for the baseline and O and H radical addition cases, the magnitudes of the EI and PI are different. Thus, their contributions to the CEMs are not always the exactly the same. The presence of radicals in the mixture may have more of an effect on the relative contributions of the EI and PI values in the smaller FFCMY-12 mechanism compared to in the larger FFCM-1 mechanism, thereby affecting the accuracy of the FFCMY-12 ignition delay. Results show that R1 tends to be an important reaction for both the detailed and reduced mechanism. One difference is the presence of R98 in the reduced mechanism, which explained by the fact that C2 chemistry was removed in the development of the reduced mechanism, thus the reaction rate for R98 had to be enhanced to compensate. The study also revealed the need for reduced mechanisms to be validated under EGR conditions and that CEMA in 0D could help by pinpointing the pertinent species and reactions and identify and determine what to examine in a large and more complex turbulent dataset. As mentioned previously, The ODT model represents an efficient and novel multi-scale approach to couple reaction, diffusion and turbulent transport and may be implemented as stand-alone for simple turbulent flows to get detailed information on the physics or may be used as a subgrid scale model in LES [22] to provide closure for reacting scalars in combustion in one dimension. Thus, one possible next step may include performing a repeat analysis using ODT particle history with CEMA at varying Ka in order to see if there is a difference in the important reactions for the CEM and to determine resolution requirements

for FFCM-1 and FFCMY-12.

REFERENCES

[1] TF Lu and CK Law. Linear time reduction of large kinetic mechanisms with directed relation graph: n-heptane and iso-octane. *Combust. Flame*, 144:24–36, 2006.

[2] TF Lu, CS Yoo, JH Chen, and CK Law. Three-dimensional direct numerical simulation of a turbulent lifted hydrogen jet flame in heated coflow: a chemical explosive mode analysis. *Journal of Fluid Mechanics*, 652(1):45–64, 2010.

[3] P Dagaut and FN Egolfopoulos. Editorial comment. *Combustion and Flame*, 159:2531–2532, 2012.

[4] T Lu and CK Law. Toward accommodating realistic fuel chemistry in large-scale computations. *Prog. Energy Combust. Sci*, 35:192–215, 2009.

[5] JF Driscoll. Turbulent premixed combustion: Flamelet structure and its effect on turbulent burning velocities. *Prog. Energy Combust. Sci.*, 34:91–124, 2008.

[6] TM Wabel, AW Skiba, JE Temme, and JF Driscoll. Measurements to determine the regimes of premixed flames in extreme turbulence. *Prog. Energy Combust. Sci*, 36:1809–1816, 2017.

[7] MJ Dunn, AR Masri, and RW Bilger. A new piloted premixed jet burner to study strong finite-rate chemistry effects. *Combust. Flame*, 151:46–60, 2007.

[8] J Hult, S Gashi, N Chakraborty, M Klein, KW Jenkins, S Cant, and CF Kaminski. Measurement of flame surface density for turbulent premixed flames using plif and dns. *Proc. Combust. Inst.*, 31:1319–1326, 2007.

[9] B Zhou, C Brackmann, Z Li, M Alden, and XS Bai. Simultaneous multi-species and temperature visualization of premixed flames in the distributed reaction zone regime. *Proc. Combust. Inst.*, 35:1409–1416, 2015.

[10] B Zhou, C Brackmann, Z Li, M Alden, and XS Bai. Distributed reactions in highly turbulent premixed methane/air flames. part i. flame structure characterization. *Combust. Flame*, 162:2937–2953, 2015.

[11] RB Chowdhury and BM Cetegen. Experimental study of the effects of free stream turbulence on characteristics and flame structure of bluff-body stabilized conical lean premixed flames. *Combust. Flame*, 178:311–328, 2017.

[12] RS Barlow and JH Frank. Effects of turbulence on species mass fractions in methane/air jet flames. *Symp. (Int.) Combust*, 27:1087–1095, 1998.

[13] AR Masri, RW Dibble, and RS Barlow. The structure of turbulent nonpremixed flames revealed by raman-rayleigh-lif measurements. *Symp. (Int.) Combust*, 22:307–362, 1996.

[14] M Juddoo and AR Masri. High-speed oh-plif imaging of extinction and re-ignition in nonpremixed flames with various levels of oxygenation. *Combust. Flame*, 158:902–914, 2011.

[15] R Cabra, T Myhrvold, JY Chen, RW Dibble, AN Karpetis, and RS Barlow. Simultaneous laser raman-rayleigh-lif measurements and numerical modeling results of a lifted turbulent h2/n2 jet flame in a vitiated coflow. *Proc. Combust. Inst.*, 29:1881–1888, 2002.

[16] SB Pope. Small scales, many species and the manifold challenges of turbulent combustion. *Proc. Combust. Inst.*, 34:1–31, 2013.

[17] Z Jozefik, NL Mundis, A Edoh, and V Sankaran. Grid convergence study of a bluff-body stabilized turbulent premixed flame. In *AIAA SciTech Forum*, page 2161. AIAA, 2018.

[18] R Ranjan, B Muralidharan, Y Nagaoka, and S Menon. Laser doppler vibrometry: Subgrid-scale modeling of reaction-diffusion and scalar transport in turbulent premixed flames. *Combustion Science and Technology*, 188(9):1496–1537, 2016.

[19] CK Law. *Combustion Physics*. Cambridge University Press, New York, 2006.

[20] D Dasgupta, W Sun, M Day, and T Lieuwen. Effect of turbulence-chemistry interactions on chemical pathways for turbulent hydrogen-air premixed flames. *Combustion and Flame*, 176:191–201, 2017.

[21] X Wang, T Jin, Y Xie, and KH Luo. Pressure effects on flame structures and chemical pathways for lean premixed turbulent h2/air flames: Three-dimensional dns studies. *Fuel*, 215:320–329, 2018.

[22] AC Zambon and WH Calhoon Jr. Private communication, 2017.

[23] C Xu, A Poludnenko, X Zhao, H Wang, and TF Lu. Structure of strongly turbulent premixed n-dodecane-air flames: Direct numerical simulations and chemical explosive mode analysis. *Combust. and Flame*, 209:27 – 40, 2019.

[24] CK Law. Combustion at a crossroads: Status and prospects. *Proc. Combust. Inst.*, 31:1–29, 2007.

[25] GP Smith, DM Golden, M Frenklach, NW Moriarty, B Eiteneer, M Goldenberg, CT Bowman, R Hanson, S Song, WC Jr. Gardiner, V Lissianski, and Z Qin. Grimech 3.0. *http://www.me.berkeley.edu/gri mech/*.

[26] M Frenklach, H Wang, C Yu, M Goldenberg, C Bowman, R Hanson, D Davidson, E Chang, G Smith, and D Golden. Gri-mech-1.2, an optimized detailed chemical reaction mechanism for methane combustion. *Gas Research Institute*, 1995.

[27] Mechanical San Diego Mechanism web page and Aerospace Engineering (Combustion Research). Chemical-kinetic mechanisms for combustion applications. *http://combustion.ucsd.edu*.

[28] H Wang, R Xu, K Wang, CT Bowman, DF Davidson, RK Hanson, K Brezinsky, and FN Egolfopoulos. A physics-based approach to modeling real-fuel combustion chemistry - i. evidence from experiments, and thermodynamic, chemical kinetic and statistical considerations. *Combust. and Flame*, 193:502 – 519, 2018.

[29] R Xu, K Wang, S Banerjee, J Shao, T Parise, Y Zhu, S Wang, A Movaghar, DJ Lee, R Zhao, X Han, Y Gao, T Lu, K Brezinsky, FN Egolfopoulos, DF Davidson, RK Hanson, CT Bowman, and H Wang. A physics-based approach to modeling real-fuel combustion chemistry - ii. reaction kinetic models of jet and rocket fuels. *Combust. and Flame*, 193:520 – 537, 2018.

[30] GP Smith, Y Tao, and H Wang. Foundational fuel chemistry model version 1.0 (ffcm-1). 2016.

[31] GP Smith, Y Tao, and H Wang. Foundational fuel chemistry model version 1.0 (ffcm-1). 2017.

[32] T Turanyi. Reduction of large reaction mechanisms. *New J. Chem.*, 14:795–803, 1990.

[33] NJ Brown, G Li, and ML Koszykowski. Mechanism reduction via principal component analysis. *Int. J. Chem. Kinet.*, 29:393–414, 1997.

[34] H Wang and M Frenklach. Detailed reduction of reaction mechanisms for flame modeling. *Combust. Flame*, 87:365–370, 1991.

[35] XL Zheng, TF Lu, CK Law, CK Westbrook, and HJ Curran. Experimental and computational study of nonpremixed ignition of dimethyl ether in counterflow. *Proc.Combust. Inst.*, 30:1101–1108, 2005.

[36] XL Zheng, TF Lu, and CK Law. Experimental counterflow ignition temperatures and reaction mechanisms of 1,3-butadiene. *Proc. Combust. Inst.*, 31:367–375, 2007.

[37] H. Pitsch P. Pepiot-Desjardins. An efficient error-propagation-based reduction method for large chemical kinetic mechanisms. *Combust. Flame*, 154:67–81, 2008.

[38] KE Niemeyer, CJ Sung, and MP Raju. Skeletal mechanism generation for surrogate fuels using directed relation graph with error propagation and sensitivity analysis. *Combust. Flame*, 157:1760–1770, 2010.

[39] W Sun, Z Chen, X Gou, and Y Ju. A path flux analysis method for the reduction of detailed chemical kinetic mechanisms. *Combust. Flame*, 157:1298–1307, 2010.

[40] X Gou, W Sun, Z Chen, and Y Ju. A dynamic multi-timescale method for combustion modeling with detailed and reduced chemical kinetic mechanisms. *Combust. Flame*, 157:1111–1121, 2010.

[41] L Tosatto, BAV Bennett, and MD Smooke. A transport-flux-based directed relation graph method for the spatially inhomogeneous instantaneous reduction of chemical kinetic mechanisms. *Combust. Flame*, 158:820–835, 2011.

[42] T Nagy and T Turanyi. Reduction of very large reaction mechanisms using methods based on simulation error minimization. *Combust. Flame*, 156:417–428, 2009.

[43] P Zhao, SM Nackman, and CK Law. On the application of betweenness centrality in chemical network analysis: Computational diagnostics and model reduction. *Combust. Flame*, 162:2991–2998, 2015.

[44] Y Liu, Y Wu, Y Gao, and T Lu. A linearized error propagation model based on jacobian analysis for skeletal mechanism reduction. In *9th U.S. National Combustion Meeting*. Cincinnati, Ohio, 2015.

[45] AS Tomlin, MJ Pilling, T Turanyi, JH Merkin, and J Brindley. Mechanism reduction for the oscillatory oxidation of hydrogen: Sensitivity and quasi-steady-state analyses. *Combust. Flame*, 91:107–130, 1992.

[46] LE Whitehouse, AS Tomlin, and MJ Pilling. Systematic reduction of complex tropospheric chemical mechanisms, part i: sensitivity and time-scale analyses. *Atmos. Chem. Phys*, 4:2025–2056, 2004.

[47] L Liang, JG Stevens, and JT Farrell. A dynamic adaptive chemistry scheme for reactive flow computation. *Proc. Combust. Inst.*, 32:527–534, 2009.

[48] Y Shi, L Liang, HW Ge, and RD Reitz. Acceleration of the chemistry solver for modeling di engine combustion using dynamic adaptive chemistry (dac) schemes. *Combust. Theor. Model*, 14:69–89, 2010.

[49] M Bodenstein and SC Lind. Geschwindigkeit der bildung des bromwasserstoffs aus seinen elementen. *Phy. Chem.-Leipzig*, 57:168–175, 1906.

[50] M Smooke. Reduced kinetic mechanisms and asymptotic approximation for methane-air flames. In *Lecture Notes in Physics*. Springer-Verlag, Berlin, 1991.

[51] T Turanyi. Sensitivity analysis of complex kinetic systems. tools and applications. *Journal of Mathematical Chemistry*, 5(3):203–248, 1990.

[52] A Coussement, BJ Isaac, and O Gicquel. Assessment of different chemistry reduction methods based on principal component analysis: Comparison of the mg-pca and score-pca approaches. *Combust. Flame*, 168:83–97, 2016.

[53] CK Law. A directed relation graph method for mechanism reduction. *Proc. Combust. Inst.*, 30:1333–1341, 2005.

[54] T Lu, M Plomer, Z Luo, S Sarathy, W Pitz, S Som, and DE Longman. Directed relation graph with expert knowledge for skeletal mechanism reduction. In *7th U.S. National Combustion Meeting*. Atlanta, Georgia, 2011.

[55] S Yang, X Wang, V Yang, W Sun, and Huo H. Comparison of flamelet/progress-variable and finite-rate chemistry les models in a preconditioning scheme. In *55th AIAA Aerospace Sciences Meeting*, page 0605. AIAA, 2017.

[56] M Bodenstein. Eine theorie der photochemischen reaktionsgeschwindigkeiten. *Zeitschrift Fur Phys. Chemie*, 85:329–397, 1913.

[57] DL Chapman and LK Underhill. Lv.-the interaction of chlorine and hydrogen. the influence of mass. *J. Chem. Soc., Trans.*, 103:496–508, 1913.

[58] S Lam and D Goussis. The csp method for simplifying kinetics. *International Journal of Chemical Kinetics*, 26(4):461–486, 1994.

[59] U Maas and SB Pope. Simplifying chemical kinetics: intrinsic low-dimensional manifolds in composition space. *Combustion and Flame*, 88(3):239–264, 1992.

[60] U Maas. Efficient calculation of intrinsic low-dimensional manifolds for the simplification of chemical kinetics. *Computing and Visualization in Science*, 1(2):69–81, 1998.

[61] S Hartl, RV Winkle, D Geyer, A Dreizler, G Magnotti, C Hasse, and RS Barlow. Assessing the relative importance of flame regimes in raman/rayleigh line measurements of turbulent lifted flames. *Proceedings of the Combustion Institute*, 37(2):2297 – 2305, 2012.

[62] K Wan, S Hartl, L Vervisch, P Domingo, RS Barlow, and journal=Combustion and Flame volume=219 number= pages=268 – 274 year=2020 publisher=Elsevier Hasse, C. Combustion regime identification from machine learning trained by raman/rayleigh line measurements.

[63] H Rabitz, M Kramer, and D Dacol. Sensitivity analysis in chemical kinetics. *Annu. Rev. Phys. Chem.*, 34:419–461, 1983.

[64] M Valorani, HN Najm, and DA Goussis. Csp analysis of a transient flame-vortex interaction: Time scales and manifolds. *Combust. Flame*, 134:35–53, 2003.

[65] HN Najm, M Valorani, DA Goussis, and J Prager. Analysis of methane-air edge flame structure. *Combust. Theor. Model.*, 14:257–294, 2010.

[66] J Prager, M Najm, HN Valoranii, and DA Goussis. Structure of n-heptane/air triple flames in partially-premixed mixing layers. *Combust. Flame*, 158:2128–2144, 2011.

[67] S Gupta, HG Im, and M Valorani. Classification of ignition regimes in hcci combustion using computational singular perturbation. *Proc. Combust. Inst.*, 33:2991–2999, 2011.

[68] P.G. Arias H.G. Im M.S. Wooldridge P.P. Ciottoli R.M. Galassi P. Pal, M. Valorani. Computational characterization of ignition regimes in a syngas/air mixture with temperature fluctuations. *Proc. Combust. Inst.*, 36:3705–3716, 2017.

[69] R Shan and T Lu. A bifurcation analysis for limit flame phenomena of dme/air in perfectly stirred reactors. *Combust. Flame*, 161:1716 – 1723, 2014.

[70] Z Luo, CS Yoo, E Richardson, JH Chen, CK Law, and TF Lu. Chemical explosive mode analysis for a turbulent lifted ethylene jet flame in highly-heated coflow. *Combustion and Flame*, 159(1):265–274, 2012.

[71] R Shan, CS Yoo, JH Chen, and TF Lu. Computational diagnostics for n-heptane flames with chemical explosive mode analysis. *Combustion and Flame*, 159(10):3119–3127, 2012.

[72] X Gao, J Zhai, W Sun, T Ombrello, and C Carter. The effect of ozone addition on autoignition and flame stabilization. In *54th AIAA Aerospace Sciences Meeting*, page 0960. AIAA, 2016.

[73] X Gao, W Sun, T Ombrello, and C Carter. The effect of ozonolysis activated autoignition on jet flame dynamics. In *55th AIAA Aerospace Sciences Meeting*. AIAA, 2017.

[74] X Gao, S Yang, B Wu, and W Sun. The effects of ozonolysis activated autoignition on non-premixed jet flame dynamics: a numerical and experimental study. In *53rd AIAA/SAE/ASEE Joint Propulsion Conference*. AIAA, 2017.

[75] S Yang, X Gao, V Yang, W Sun, S Nagaraja, JK Lefkowitz, and Y Ju. Nanosecond pulsed plasma activated c2h4/o2/ar mixtures in a flow reactor. *Journal of Propulsion and Power*, 32(5):1240–1252, 2016.

[76] X Gao, Y Zhang, S Adusumilli, J Seitzman, W Sun, T Ombrello, and C Carter. The effect of ozone addition on laminar flame speed. *Combustion and Flame*, 162(10):3914–3924, 2015.

[77] D Gers, A Ghosh, A Trouve, and K Yu. Simulation of acoustically forced h2-o2 shear coaxial model injector. In *48th AIAA Aerospace Sciences Meeting Including the New Horizons Forum and Aerospace Exposition*, page 1523. AIAA, 2010.

[78] S Candel, G Herding, R Synder, P Scouflaire, P Rolon, L Vingert, M Habiballah, F Grisch, and M Pe. Experimental investigation of shear coaxial cryogenic jet flames. *Journal of Propulsion and Power*, 14(5):826–834, 1998.

[79] B Yang, F Cuoco, and M Oschwald. Atomization and flames in lox/h2-and lox/ch4-spray combustion. *Journal of Propulsion and Power*, 23(4):763–771, 2007.

[80] B Yang, F Cuoco, and M Oschwald. Effect of recess in high-pressure liquid oxygen/methane coaxial injection and combustion. *Journal of Propulsion and Power*, 25(1):24–32, 2009.

[81] DJ Forliti, A Badakhshan, J Wegener, IA Leyva, and DG Talley. The response of cryogenic h2/o2 coaxial jet flames to acoustic disturbances. In *53rd AIAA Aerospace Sciences Meeting, AIAA SciTech*. AIAA, 2015.

[82] JL Wegener, DJ Forliti, IA Leyva, and DG Talley. Receptivity of a cryogenic coaxial gas-liquid jet to acoustic disturbances. In *50th AIAA/ASME/SAE/ASEE Joint Propulsion Conference, Propulsion and Energy Forum*. AIAA, 2014.

[83] S Teshome, IA Leyva, D Talley, and AR Karagozian. Cryogenic high-pressure shear-coaxial jets exposed to transverse acoustic forcing. In *50th AIAA Aerospace Sciences Meeting, Nashville, TN*. AIAA, 2012.

[84] IA Leyva, JI Rodriguez, B Chehroudi, and D Talley. Preliminary results on coaxial jet spread angles and the effects of variable phase transverse acoustic fields. In *46th AIAA Aerospace Sciences Meeting Exhibit*. AIAA, 2008.

[85] I Leyva, B Chehroudi, and DG Talley. Dark core analysis of coaxial injectors at sub-, near-, and supercritical conditions in a transverse acoustic field. In *43rd AIAA/ASME/SAE/ASEE Joint Propulsion Conference and Exhibit*, page 5456. AIAA, 2007.

[86] JJ Graham, IA Leyva, JI Rodriguez, and D Talley. On the effect of a transverse acoustic field on a flush shear coaxial injector. In *45th AIAA Joint Propulsion Conference Exhibit*. AIAA, 2009.

[87] JI Rodriguez, JJ Graham, IA Leyva, and D Talley. Effect of variable phase transverse acoustic fields on coaxial jet forced spread angles (preprint). In *47th AIAA Aerospace Sciences Meeting and Exhibit*. AIAA, 2009.

[88] JI Rodriguez. Acoustic excitation of liquid fuel droplets and coaxial jets. *PhD thesis, University of California at Los Angeles, Los Angeles, CA*, 2009.

[89] JI Rodriguez. Droplet combustion and non-reactive shear-coaxial jets with transverse acoustic excitation. *PhD thesis, University of California at Los Angeles, Los Angeles, CA*, 2012.

[90] B Chehroudi, D Davis, and D Talley. Initial results from a cryogenic coaxial injector in an acoustic field. In *41st AIAA Aerospace Sciences Meeting and Exhibit*. AIAA, 2003.

[91] ME Harvazinski, WE Anderson, and CL Merkle. Analysis of self-excited combustion instabilities using two-and three-dimensional simulations. *Journal of Propulsion and Power*, 29(2):396 – 409, 2013.

[92] ME Harvazinski, C Huang, V Sankaran, TW Feldman, WE Anderson, CL Merkle, and DG Talley. Coupling between hydrodynamics, acoustics, and heat release in a self-excited unstable combustor. *Physics of Fluids*, 27(4):045102, 2015.

[93] SV Sardeshmukh, WE Anderson, ME Harvazinski, and V Sankaran. Prediction of combustion instability with detailed chemical kinetics. In *AIAA SciTech Forum, 53rd AIAA Aerospace Sciences Meeting*. AIAA, 2015.

[94] SV Sardeshmukh, C Huang, WE Anderson, ME Harvazinski, and V Sankaran. Impact of chemical kinetics on the predictions of bluff body stabilized flames. In *AIAA SciTech Forum, 54th AIAA Aerospace Sciences Meeting*. AIAA, 2016.

[95] K Miller, J Sisco, N Nugent, and W Anderson. Combustion instability with a single-element swirl injector. *Journal of Propulsion and Power*, 23:1102 – 1112, 2007.

[96] YC Yu, JC Sisco, S Rosen, A Madhav, and WE Anderson. Spontaneous longitudinal combustion instability in a continuously-variable resonance combustor. *Journal of Propulsion and Power*, 285(5):876 – 887, 2012.

[97] YC Yu. Experimental and analytical investigations of longitudinal combustion instability in a continuously variable resonance combustor (cvrc). *Purdue University*, 2009.

[98] JC Oefelein and V Yang. Modeling high-pressure mixing and combustion processes in liquid rocket engines. *Journal of Propulsion and Power*, 14(5):843–857, 1998.

[99] G Lacaze and JC Oefelein. A non-premixed combustion model based on flame structure analysis at supercritical pressures. *Combustion and Flame*, 158(20):2087–2103, 2012.

[100] MJ Foust, M Deshpande, S Pal, T Ni, CL Merkle, and RJ Santoro. Experimental and analytical characterization of a shear coaxial combusting go2/gh2 flowfield. In *34th AIAA Aerospace Sciences Meeting and Exhibit*, page 0646. AIAA, 1996.

[101] JC Oefelein. Numerical mixing and combustion of cryogenic oxygen-hydrogen shear-coaxial jet flames at supercritical pressure. *Combustion Science and Technology*, 178:229–252, 2006.

[102] G Xia, V Sankaran, D Li, and C Merkle. Modeling of turbulent mixing layer dynamics in ultra-high pressure flows. In *36th AIAA Fluid Dynamics Conference and Exhibit*, page 3729. AIAA, 2006.

[103] CF Curtiss and JO Hirshfelder. Transport properties of multicomponent gas mixtures. *The Journal of Chemical Physics*,, 17–6:550–555, 1949.

[104] BJ McBride, MJ Zehe, and S Gordon. Nasa glenn coefficients for calculating thermodynamic properties of individual species. *Technical Report TP-2002-211556, NASA*, 2002.

[105] BJ McBride, MJ Zehe, and MA Reno. Coefficients for calculating thermodynamic and transport properties of individual species. *Technical Report TM-4513, NASA*, 1993.

[106] CR Wilke. A viscosity equation for gas mixtures. *Journal of Chemical Physics*, 18:517–519, 1950.

[107] S Mathur, PK Tondon, and SC Saxena. Thermal conductivity of binary ternary and quaternary mixtures of rare gases. *Molecular Physics*, 12, 1967.

[108] SB Pope. *Turbulent Flows*. Cambridge, New York, 2008.

[109] D Wilcox. Formulation of the $k - \omega$ turbulence model revisited. *AIAA Journal*, 46(11):2823–2838, 2008.

[110] SR Turns. *An Introduction to Combustion*. McGraw Hill, 2000.

[111] J Li, Z Zhao, A Kazakov, and FL Dryer. An updated comprehensive kinetic model of hydrogen combustion. *International Journal in Chemical Kinetics*, 36:566–575, 2004.

[112] J Su, Y Wu, Y Wang, X Chen, , and Z Chen. Skeletal and reduced kinetic models for methane oxidation under engine-relevant conditions. *Fuel*, (119667), 2012.

[113] V Sankaran and C Merkle. Dual time stepping and preconditioning for unsteady computations. In *Aerospace Sciences Meeting and Exhibit, 33rd*, page 0078. AIAA, 1995.

[114] RJ Kee, FM Rupley, JA Miller, ME Coltrin, JF Grcar, E Meeks, HK Moffat, AE Lutz, G DixonLewis, MD Smooke, J Warnatz, GH Evans, RS Larson, RE Mitchell, LR Petzold, WC Reynolds, M Caracotsios, WE Stewart, P Glarborg, C Wang, and O Adigun. Chemkin collection. *Release 3.6, Reaction Design, Inc., San Diego, CA*, 2000.

[115] LR Petzold. A description of dassl. In *Sandia National Laboratories Report*, pages SAND82 – 8637. AFOSR, 1982.

[116] J Manohar, YJ Kim, MC Kim, and JS Kim. Numerical simulation of the combustion characteristics in gch4-go2 shear coaxial injector using various combustion models and kinetic mechanisms. In *AIAA Propulsion and Energy 2020 Forum*. AIAA, 2020.

[117] S Badillo-Rios. Effect of chemical kinetic mechanisms on turbulent combustion. *Prospectus, UCLA*, 2019.

[118] LR Petzold. Large eddy simulation of flame-turbulence interactions in a lox-ch4 shear coaxial injector. In *50th AIAA Aerospace Sciences Meeting including the New Horizons Forum and Aerospace Exposition*. AIAA, 2012.

[119] XJ Gu, DR Emerson, and D Bradley. Modes of reaction front propagation from hot spots. *Combust. Flame*, 133:63 – 74, 2003.

[120] CS Yoo, T Lu, JH Chen, and CK Law. Direct numerical simulations of ignition of a lean nheptane/air mixture with temperature inhomogeneities at constant volume: Parametric study. *Combust. Flame*, 158:1727 – 1741, 2011.

[121] R Sankaran. Propagation velocity of a deflagration front in a preheated autoigniting mixture. In *9th U.S. National Combustion Meeting, Cincinnati, Ohio*. elsevier, 2015.

[122] A Krisman, ER Hawkes, and JH Chen. The structure and propagation of laminar flames under autoignitive conditions. *Combust. Flame*, 188:399 – 411, 2018.

[123] A Kazakov, M Chaos, Z Zhao, and FL Dryer. Computational singular perturbation analysis of two-stage ignition of large hydrocarbons. *J. Phys. Chem.*, 110:7003 – 7009, 2006.

[124] SH Lam. Using csp to understand complex chemical kinetics. *Comb. Sci. Technol.*, 89:375–404, 1993.

[125] DA Goussis and HN Najm. Model reduction and physical understanding of slowly oscillating processes: the circadian cycle. *Multiscale Modeling and Simulation*, 5(4):1297–1332, 2006.

[126] AR Kerstein. One-dimensional turbulence: model formulation and application to homogeneous turbulence, shear flows, and buoyant stratified flows. *J. Fluid Mech.*, 392:277–334, 1999.

[127] S Cao and T Echekki. The one-dimensional-turbulence model. *J. Turbul.*, 9:1–35, 2008.